AMERICAN UNIVERSITY OF BEIRUT

ROBUSTNESS ANALYSIS OF WIND TURBINE CONTROL SYSTEMS

by
OMAR FADI FARHAT

A thesis
submitted in partial fulfillment of the requirements
for the degree of Master of Engineering
to the Department of Mechanical Engineering
of Maroun Semaan Faculty of Engineering and Architecture
at the American University of Beirut

Beirut, Lebanon
December 2022

AMERICAN UNIVERSITY OF BEIRUT

ROBUSTNESS ANALYSIS OF WIND TURBINE CONTROL SYSTEMS

by

OMAR FADI FARHAT

Approved by:

Dr. Dany Abou Jaoude, Assistant Professor — Advisor

Mechanical Engineering

Dany Abou Jaoude 2023.02.07 13:36:37 +02'00'

Dr. Elie Shammas, Associate Professor — Member of Committee

Mechanical Engineering

Dr. Naseem Daher, Associate Professor — Member of Committee

Electrical and Computer Engineering

Dr. Devaprakash Muniraj, Assistant Professor — Member of Committee

Aerospace Engineering

Indian Institute of Technology, Madras

Date of thesis defense: December 22, 2022

AMERICAN UNIVERSITY OF BEIRUT

THESIS RELEASE FORM

Student Name: Farhat (Last) Omar (First) Fadi (Middle)

I authorize the American University of Beirut, to: (a) reproduce hard or electronic copies of my thesis; (b) include such copies in the archives and digital repositories of the University; and (c) make freely available such copies to third parties for research or educational purposes

☑ **As of the date of submission of my thesis**

___ **After 1 year from the date of submission of my thesis .**

___ **After 2 years from the date of submission of my thesis .**

___ **After 3 years from the date of submission of my thesis .**

Signature

January 7, 2023

Date

Acknowledgements

I would first like to thank and express my sincere gratitude to my advisor Dr. Dany Abou Jaoude for his continuous support, patience, and encouragement. His guidance and assistance have made my graduate studies at the American University of Beirut (AUB) an exceptional learning experience and were crucial for the completion of this thesis.

I would also like to thank my thesis committee members Dr. Elie Shammas, Dr. Naseem Daher, and Dr. Devaprakash Muniraj for their time and invaluable feedback.

I would also especially wish to acknowledge the efforts and encouragement of my family members who have been very caring, patient, and supportive. I must also thank my friends for their motivation and for being there in my time of need.

Finally, I would like to thank the Global Sustainable Electricity Partnership (GSEP) for granting me the 2020 Education for Sustainable Energy Development (ESED) scholarship to support my master's degree at AUB.

This thesis was supported by the University Research Board (URB) at AUB.

Abstract of the Thesis of

Omar Fadi Farhat for Master of Engineering
Major: Mechanical Engineering

Title: Robustness Analysis of Wind Turbine Control Systems

In this thesis, a framework for robustness analysis of wind turbine control systems is proposed. This framework is employed to examine and compare the robustness of $\mathcal{H}_\infty$ and PI blade pitch controllers designed to maintain the turbine's generated power at its rated value in Region 3 of the wind turbine operation. The $\mathcal{L}_2$-induced norm of the closed-loop system is used as the performance metric. In this framework, a turbulent wind model based on the Kaimal spectrum is added to the closed-loop wind turbine model obtained by linearizing the nonlinear model at different operating wind speeds. This framework utilizes the theory of Integral Quadratic Constraints (IQCs), whereby IQCs and signal IQCs are used to incorporate the wind model into the wind turbine model. As a result, upper bounds on the $\mathcal{L}_2$-induced norm of the system are obtained by solving semidefinite programs (SDPs). The proposed framework results in a better characterization of the system's performance. The analysis results from the proposed framework are verified and validated via extensive high-fidelity simulations of the nonlinear wind turbine model.

Table of Contents

Illustrations

Tables

Abbreviations

ILMI	Iterative linear matrix inequality
IQC	Integral quadratic constraints
KYP	Kalman–Yakubovich–Popov
LFT	Linear fractional transformation
LMI	Linear matrix inequality
LPV	Linear parameter-varying
LTI	Linear time-invariant
LTV	Linear time-varying
MBC	Multi-blade coordinate
PI	Proportional integral
PID	Proportional integral derivative
PLTV	Periodic linear time-varying
SDP	Semidefinite program
SLTV	Static linear time-varying
SOF	Static output feedback

Chapter 1

INTRODUCTION

Wind energy is a rapidly growing field all over the world. According to the Global Wind Energy Council (GWEC), the global installed capacity of wind power increased by an annual growth of 53% in 2020, which makes it the best year in history for the global wind industry. In addition, GWEC states that wind turbines need to be installed at a much faster rate in the upcoming decade to mitigate the worst impacts of climate change [1].

For wind turbines to be competitive within the energy market, the cost of generating wind power should be economically competitive with that of conventional power production. For this purpose, high performance and reliability of wind turbines are required. The area of control systems has significantly contributed to the reduction of the cost of wind-generated electricity. In order to reduce the cost of wind power, a wind turbine is controlled to maximize energy production, as well as to minimize mechanical loads to extend its lifetime.

The rapid growth in the wind energy industry brings several challenges to the current turbine control system. Wind turbines are highly nonlinear systems subject to varying dynamics and uncertainties in different wind conditions. As the size of wind turbines grows, considerations on load reduction become more critical. This motivates the need for robust control strategies that ensure satisfactory and robust performance of the wind turbine despite all operating conditions and model uncertainties.

1.1 Thesis Contribution

This thesis is the first work proposing a comprehensive model-based framework for the analysis and certification of wind turbine control systems using tools from robust control theory. This framework provides a systematic and rigorous tool for designing, testing, and certifying that a controller is safe for implementation on a real wind turbine. The framework allows for comparing the performance of different controllers with respect to different outputs, as well as comparing the same controller's performance across varying wind speeds. The novelty of the proposed framework consists in incorporating the characteristics of a turbulent wind profile in the analysis of the closed-loop wind turbine model in the following approach:

- The wind turbine model is subject to an exogenous input, which is the wind disturbance. Instead of assuming the wind disturbance to be any finite energy ($\mathcal{L}_2$) signal, a wind model is incorporated into the wind turbine model. This wind model is based on Kaimal's characterization of turbulence and generates a turbulent wind profile from white noise inputs. Moreover, this wind model contains time-varying trigonometric terms. Hence, the resulting combined wind turbine model is a time-varying system with white noise signals as exogenous inputs.

- The complex combined wind turbine model is systemically handled using the theory of integral quadratic constraints. The time-varying trigonometric terms are treated as uncertainties, and the resulting time-varying system can be modeled in the Linear Fractional Transformation (LFT) framework as a feedback interconnection of a linear time-invariant nominal system with uncertainties. This configuration allows for characterizing the uncertainties as static linear time-varying (SLTV) parameters using the Integral Quadratic Constraints (IQCs) framework. This framework allows for performing the robustness analysis of the system by solving semidefinite programs, which can be solved using readily available numerical solvers.

- Signal IQCs are also incorporated in the proposed analysis framework. The white noise inputs of the wind model are characterized via signal IQCs. Instead of assuming the white noise inputs to be any finite energy ($\mathcal{L}_2$) signals, signal IQCs allow for constraining these inputs to lie in a predefined set of white noise signals (a subset of $\mathcal{L}_2$). This results in a more accurate description of the exogenous inputs.

The proposed analysis framework is tested as follows:

- Linearizations of the nonlinear wind turbine model are obtained at different operating wind speeds.

- For one operating wind speed, $\mathcal{H}_\infty$ and PI blade pitch controllers are designed with the objective of maintaining the generated power of the wind turbine at its rated value in Region 3 of the wind turbine operation (high wind speeds).

- The robust performance of the two controllers is examined and compared at different wind speeds using the proposed analysis framework. The $\mathcal{L}_2$-induced norm of the closed-loop system, which measures the worst-case amplification from the exogenous inputs of the system to its outputs, is used as the performance metric. Upper bounds on the $\mathcal{L}_2$-induced norm of the system are obtained by solving semidefinite programs.

- The findings from the proposed analysis framework are benchmarked against observations based on extensive simulations performed on a high-fidelity nonlinear wind turbine model.

The importance of the proposed analysis framework lies in the following:

- Even though IQC analysis of wind turbine control systems has already been performed in the literature, this work is the first to incorporate the characteristics of a wind profile into the analysis, thereby allowing for analysis that more accurately reflects the wind turbine's performance and operating conditions.
- Traditionally, controller testing is done through high-fidelity extensive simulations, which are time-consuming. The proposed framework systematizes and speeds up the process of performing robustness analysis of wind turbine control systems. Thus, it is a complementary tool for simulations, and the insights obtained using the framework match those from the simulations but are attained much faster.
- Another problem with solely relying on simulations is that they may fail to predict rare failures and extreme case occurrences. The proposed framework allows for obtaining performance bounds that are of a worst-case type and cover all simulations. That is, it defines a guaranteed operating envelope that cannot be violated during operation. Since real-life implementation of controllers on wind turbines is expensive and risky, this framework helps in reducing costs by discarding controllers that cannot be certified to be safe.
- Even though a specific wind model based on Kaimal's characterization of turbulence is used in this framework, the developed framework is not specialized to one wind model. In fact, the framework is modular in the sense that any other wind model can be incorporated in the same manner. That is, if given any other wind profile or statistical data reflecting specific wind conditions in a given locality, they can be seamlessly incorporated into the analysis framework. This provides a useful tool for control synthesis, whereby engineers can design controllers targeted to specific wind conditions.
- Similarly, this framework can be also easily modified to account for other, improved models of the wind turbine. Even though the framework uses linear-time invariant models of the wind turbine in this thesis, other wind turbine models such as periodic linear time-varying (PLTV) and linear parameter-varying (LPV) models can be used. Thus, this thesis lays the groundwork for and enables the development of even better analysis tools, via the incorporation of better wind turbine models and/or specific turbulent wind information.

This framework is to be built-upon in future work, and hence, the analysis performed in this thesis is not comprehensive. Therefore, over-reaching conclusions will not be made from the analysis framework and simulations as some additions to the framework must be done to yield more accurate results. Namely, nonlinearities and uncertainties of the wind turbine model should be considered in the future. In addition, better tuning methods of the IQC filters should be considered.

1.2 Literature Review

The works that have been explored thoroughly are listed in Table 1.1.

Table 1.1: Relevant works on modeling and control of wind turbines and analysis using the theory of Integral Quadratic Constraints.

Topic		Relevant Works
Modeling of Wind Turbines		[2]–[8]
PI Control		[9]–[11]
Wind Turbine Baseline Controller		[3]
Periodic Control of Wind Turbines		[12], [13]
Adaptive Control of Wind Turbines		[14]
$\mathcal{H}_\infty$ Control		[15]–[21]
$\mathcal{H}_\infty$ Control of Wind Turbines		[22], [23]
LPV Control of Wind Turbines		[24], [25]
Integral Quadratic Constraints	IQC Theory	[26]–[35]
	Wind Turbines IQC Analysis and Synthesis	[36]
	Applied IQC Analysis and Synthesis Featuring Signal IQCs	[37], [38]

Modeling of Wind Turbines: Many models of wind turbines have been developed in the literature. In this thesis, a high-fidelity nonlinear wind turbine model provided by OpenFAST [2] and developed by the National Renewable Energy Laboratory (NREL) is adopted. A detailed description of this model is presented in Section 3.2 of the thesis. A one-state nonlinear model of the wind turbine is given in [3]. This model captures steady-state aerodynamics and rigid-body rotor dynamics, but not structural dynamics of the wind turbine. In this single degree-of-freedom model, all the rotating parts, including the blades, hub, and drive train, are considered rigid bodies. This model is helpful for understanding the basic principles of wind turbine operation. In this simple rotational system, the lift force generated on the turbine blades yields a torque on the rotor shaft, which is then balanced by the generator torque on the high-speed shaft. Other models that have been used include the one developed in [4], wherein a simple wind turbine benchmark model is developed. In this model, the blades and the tower are assumed rigid, and aerodynamics are described by a static model. The aerodynamics of the wind turbine are modeled as a torque acting on the blades, and the pitch system is modeled as a second-order piston servo system. The drive train is modeled by a two-mass model, and the generator and converter dynamics are modeled by a first-order transfer function.

Several mathematical representations of the turbulence experienced by wind turbines have been developed in the literature. One wind model is based on Kaimal's characterization of turbulence [5], [6]. This wind model is adopted in this thesis, and a detailed description of this model is presented in Section 3.5. Another wind model is proposed in [7], wherein a mathematical model describing turbulence is developed based on the von Karmen power spectrum. A simple wind model is presented in [8] in which the wind is simulated at one point only. This model consists of a spatial filter connected to a rotational sampling filter. The spatial filter aims at damping

the high-frequency components of the wind, which represents the filtering properties of the wind turbine blades. The rotational sampling filter serves to represent the rotational sampling of the wind as it hits the wind turbine blades.

Control of Wind Turbines: The wind turbine baseline controller is presented in [3]. It consists of a nonlinear generator torque controller that maximizes the generated power in Region 2 of the wind turbine operation and a PI pitch actuator controller that maintains the rated power in Region 3 of the wind turbine operation. Further details can be found in Section 3.1 of the thesis. In this thesis, a wind turbine Region 3 PI controller is designed as detailed in Section 2.3. The works in [9]–[11] proposed transforming the problem of designing a PID controller into that of a static output feedback (SOF) controller. Three different LMI conditions, corresponding to stability, $\mathcal{H}_\infty$ performance specification, and $\mathcal{H}_2$ performance specification, are presented. Then, algorithms based on iterative Linear Matrix Inequality (ILMI) techniques are proposed for designing the controllers. Advanced control of wind turbines has been widely explored in the literature, including periodic control [12], [13], adaptive control [14], $\mathcal{H}_\infty$ control [22], [23], and LPV control [24], [25].

The work in [12] aims to study whether periodic control is more effective than using constant gains. The control objective is regulating the wind turbine's speed in a fluctuating wind field in Region 3 of the wind turbine operation. A two-bladed, variable-speed, horizontal-axis wind turbine model is considered, the generator torque is set to a constant, and collective blade pitch is used. Periodic and constant-gain full-state feedback controllers are designed using optimal control theory on a linearized periodic model. Two turbulent wind conditions with different gust speed profiles are chosen to test the performance of the two controllers. The periodic gain controller did not show significantly improved performance over the constant gain controller. However, the periodic controller has an advantage over the constant controller in the sense that stability is guaranteed when implemented on a linear periodic plant. Moreover, when implemented on a nonlinear model, the system is less likely to become unstable. The disadvantage of a periodic controller is that it requires knowledge of the rotor position, which is not an observable state. The work in [12] is extended in [13] by incorporating periodic state estimation. Moreover, individual blade pitch actuation is used instead of collective pitch. In addition to regulating the rotor speed, the controller aims at mitigating cyclic loads. Disturbance Accommodating Control, which is a model-based approach to reject persistent disturbances to a linear system, is used in this paper to estimate fluctuating wind disturbances. Periodic, time-invariant constant-gain, and PID controllers are designed. Then, the designed controllers are compared and tested via simulations performed on a wind turbine nonlinear model subject to fluctuating wind input. The periodic and time-invariant controllers were able to reduce the cyclic loads without compromising the rotor speed regulation, with the periodic controller yielding a superior performance since a time-varying wind turbine model is used to estimate the unmeasured states.

An adaptive controller is designed in [14]. An adaptive generator torque controller is designed to maximize power generation in Region 2 of the wind turbine

operation, with the blade pitch angle set to a constant. This paper focuses on analyzing the stability of the developed control system and shows how the rotor speed is asymptotically stable in constant wind conditions and $\mathcal{L}_2$ stable in the case of varying wind speeds. In addition, a scheme is developed for the gain adaptation law to guarantee that the adaptive gain converges to its optimal value. The developed adaptive control scheme is tested on the Controls Advanced Research Turbine (CART) located in the NREL's National Wind Technology Center.

The problem of the design of an $\mathcal{H}_\infty$ controller has been extensively explored. The objective of this controller is to obtain a stable closed-loop system that has some upper bound on its $\mathcal{L}_2$-induced norm. This norm measures the worst-case amplification of a finite energy exogenous input signal at the performance output of the system. The $\mathcal{H}_\infty$-norm condition is in general not convex, and thus, the $\mathcal{H}_\infty$ controller design problem is not a convex optimization problem [15]. The works of [16]–[18] present LMI-based characterizations of the $\mathcal{H}_\infty$ performance condition, which allow for convex optimization formulations of the $\mathcal{H}_\infty$ controller design problem. Further details on the design of $\mathcal{H}_\infty$ controllers are presented in Section 2.2. The distributed $\mathcal{L}_2$-induced norm control of discrete-time, nonstationary linear parameter-varying (NSLPV) subsystems is explored in [19], wherein the NSLPV subsystems are represented in the LFT framework and are interconnected over arbitrary graphs. An NSLPV model is an extension of a standard LPV model wherein the nominal part of the system is allowed to be time-varying, to account for a priori available information on the time-varying terms in the system model [20], [21]. The designed controller is then a distributed NSLPV system with its subsystems having the same interconnection and LFT structures as the plant. Analysis and synthesis results were derived in terms of infinite sequences of LMIs. However, these conditions become finite-dimensional for eventually periodic systems over finite graphs.

A wind turbine $\mathcal{H}_\infty$ blade pitch controller is presented in [22]. The presented multivariable control design approach for an individual pitch controller aims at reducing structural loads on the rotating and nonrotating parts of the wind turbine. A controller tuning strategy that mitigates the dominant loads on the blade and nacelle is also presented. The LTI model in [22] is extended to an LPV model in [24]. The $\mathcal{H}_\infty$ controller in [22] performed better than LPV controller in [24] at its design condition (operating speed); however, this performance degraded at wind speeds higher than that of the controller design condition. The LPV controller showed better robustness at high wind speeds. In [23], an $\mathcal{H}_\infty$ controller is designed at several operating points, with the objective of power reference tracking and structural loads minimization. This controller is gain-scheduled based on the wind speed and the power output, which allows the wind turbine to operate smoothly. This work is extended in [25], wherein an LPV controller of the wind turbine is designed. An LPV model of the wind turbine, dependent on the operating wind speed, is used. Then, a robust control framework is proposed using the LPV design method. As a result, the controller designed using this method covers the turbine operations in all wind conditions. The LPV approach provides guarantees on the stability and performance of the closed-loop system, in contrast to the gain-scheduling approach. Improved load reduction of the proposed LPV controller was observed.

Integral Quadratic Constraints (IQCs): In this thesis, a framework is proposed for the analysis of wind turbine control systems, which utilizes the theory of Integral Quadratic Constraints (IQCs). The IQCs framework [26] provides a method for representing real-world complex and uncertain dynamical systems in a form that is convenient for stability and performance analysis. Nonlinearities, time-varying coefficients, parametric uncertainties, and unmodeled dynamics having complex mathematical descriptions can be replaced by IQC characterizations [27]. This allows for performing the analysis of the system by solving semidefinite programs, which can be solved using readily available numerical solvers [28]. As a result, IQC analysis allows for obtaining guaranteed upper bounds on the $\mathcal{L}_2$-induced norm of uncertain systems. Exogenous input signals of a system can be also characterized by signal IQCs [29]. A list of available classes of IQC and signal IQC multipliers can be found in [26], [29]–[31].

While the theory of IQCs is applied on a single, continuous-time, linear time-invariant system in this thesis, there have been multiple works that apply the IQCs theory to discrete-time, linear time-varying systems [32]–[35]. The robustness analysis framework using IQCs is extended to uncertain distributed systems in [32] and systems with uncertain initial conditions in [33]. Novel results are presented in [34], [35], wherein a novel method for computing point-wise bounds on the performance outputs is proposed in [34], and a novel method for the computation of invariant sets using the S-procedure and point-wise IQCs is presented in [35].

In addition to IQC analysis, IQCs can also be incorporated into control synthesis problems. In [36], a controller synthesis algorithm for LPV systems using the theory of IQCs is presented. This algorithm alternates between synthesis and analysis steps, both solved as semidefinite programs. The proposed algorithm results in a non-increasing robust performance at each iteration. In this thesis, only IQC analysis is performed.

A comprehensive analysis framework for small fixed-wing unmanned aircraft systems (UAS) is proposed in [37]. In the proposed framework, the uncertain UAS model is represented in the LFT framework. The theory of IQCs is then used for complete system uncertainty characterization and quantification, and robustness analysis of the system is performed. This work is pioneering in the sense of applying IQCs to complex engineering systems, in addition to extensively validating the results in actual flight experimentations. Flight test data is used to quantify the UAS uncertainties. Moreover, an IQC-based controller synthesis algorithm is presented and implemented, which helps emphasize the effect of the uncertainties on the system and provides guidance for improved control design. In [38], the framework proposed in [37] is improved in the sense that the analysis can be done for any UAS flight path with a bounded radius of curvature. $\mathcal{H}_\infty$ and $\mathcal{H}_2$ trajectory-tracking controllers, and $\mathcal{H}_\infty$, $\mathcal{H}_2$, and PID path-following controllers are synthesized and tuned using IQC analysis. Signal IQCs have also been added to model the wind disturbance. The analysis results of the proposed framework are compared to physical flight data. Results were reliable, less conservative, and reflective of the actual flight data.

1.3 Thesis Overview

The outline of this thesis is as follows. In Chapter 2, the notation and mathematical preliminaries of the thesis are presented. In addition, the $\mathcal{H}_\infty$ and PI controller synthesis problems are described. The Integral Quadratic Constraints (IQCs) theory is also introduced. In Chapter 3, an overview of modeling, basic operation, and control of wind turbines is presented. A high-fidelity nonlinear model of a horizontal-axis, three-bladed, variable-speed, pitch-controlled, onshore wind turbine is described. A linearized wind turbine model is then presented. In Chapter 4, the proposed framework and results of this thesis are presented. In Chapter 5, concluding remarks on this work are presented. In addition, the future work beyond this thesis is outlined.

Chapter 2

PRELIMINARIES

In this chapter, an overview of the notation and mathematical preliminaries is outlined. In addition, concepts from robust control theory used in the thesis are presented.

2.1 Notation

The set of real numbers is denoted by $\mathbb{R}$. The sets of n-dimensional real vectors and $m \times n$ real matrices are denoted by $\mathbb{R}^n$ and $\mathbb{R}^{m\times n}$, respectively. $D = \mathbf{diag}(d_1, \ldots, d_n)$ denotes a diagonal matrix D with the elements $d_1, \ldots, d_n$ on its diagonal. $\mathbf{D} = \mathbf{Blkdiag}(D_1, \ldots, D_n)$ denotes a block-diagonal matrix $\mathbf{D}$ with the matrices $D_1, \ldots, D_n$ on its diagonal blocks. $\mathbf{0}$ denotes a matrix that consists of all zero entries. The $n\times n$ identity matrix is denoted by I_n. $C \succ 0$ and $C \succeq 0$ mean that the symmetric matrix C is positive definite and positive semidefinite, respectively.

M^T and M^* denote the transpose and conjugate transpose of a matrix M, respectively. M^{-1} denotes the inverse of a nonsingular matrix M. The trace of a square matrix A is denoted by $\mathbf{tr}(A)$. The rank of a matrix A is denoted by $\mathbf{rank}(A)$. The null space of a matrix A is denoted by $\mathcal{N}(A)$. The largest singular value of a (possibly nonsquare) complex matrix A is defined as $\bar{\sigma}(A) = \sqrt{\lambda_{\max}(A^*A)}$.

$\mathcal{L}_2^n$ denotes the Hilbert space of $\mathbb{R}^n$-valued, square-summable sequences. For a signal $u \in \mathcal{L}_2^n$, the $\mathcal{L}_2$-norm of u is defined as $\|u\|_2^2 = \int_0^{+\infty} u(t)^T u(t)dt$. The symbol $\mathcal{L}_2$ is often used for simplicity. $\mathcal{RL}_\infty$ denotes the space of proper real rational matrix functions with no poles on the imaginary axis. $\mathcal{RH}_\infty \subset \mathcal{RL}_\infty$ denotes the space of proper real rational matrix functions with no poles in the closed right half complex plane.

2.2 $\mathcal{H}_\infty$ Control

Consider an open-loop, continuous-time system G with state-space equations of the form

$$\begin{bmatrix} \dot{x}_{OL}(t) \\ e(t) \\ y(t) \end{bmatrix} = \begin{bmatrix} A & B_1 & B_2 \\ C_1 & D_{11} & D_{12} \\ C_2 & D_{21} & \mathbf{0} \end{bmatrix} \begin{bmatrix} x_{OL}(t) \\ u_d(t) \\ u_c(t) \end{bmatrix}, \tag{2.1}$$

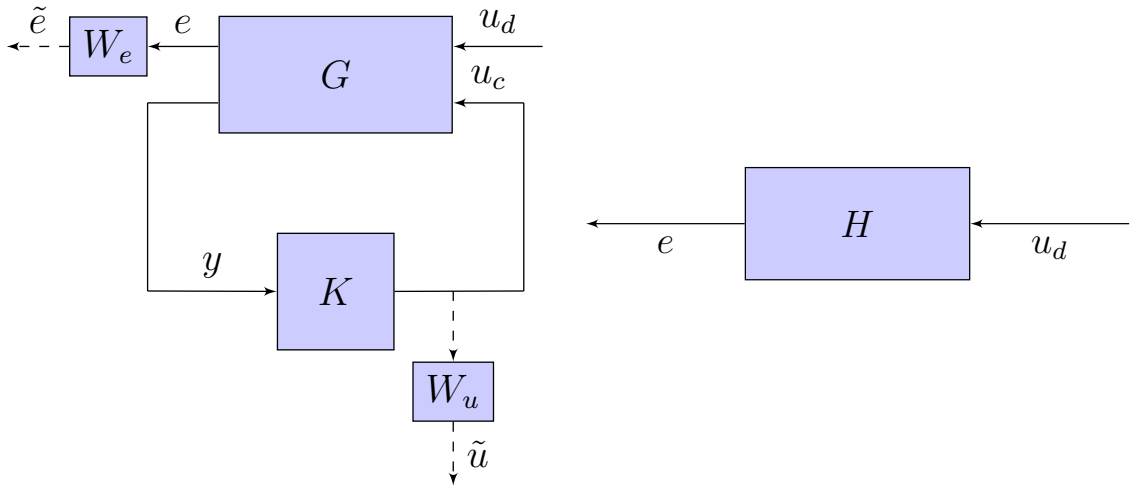

(a) Interconnection of a plant and a controller.

(b) Resulting closed-loop system.

Figure 2.1: Block diagram of a plant and a controller.

where $t \geq 0$ denotes continuous time, $x_{OL}(t) \in \mathbb{R}^{n_G}$ is the vector of state variables, $u_d(t) \in \mathbb{R}^{n_d}$ is the vector of exogenous inputs, $u_c(t) \in \mathbb{R}^{n_u}$ is the vector of control inputs, $e(t) \in \mathbb{R}^{n_e}$ is the vector of performance outputs, and $y(t) \in \mathbb{R}^{n_y}$ is the vector of measured outputs. The model used for synthesis can also include frequency weights W_e and W_u on the performance outputs and control inputs, respectively, as shown in Figure 2.1a.

A dynamic controller K is given by the equations

$$\begin{bmatrix} \dot{x}_K(t) \\ u_c(t) \end{bmatrix} = \begin{bmatrix} A_K & B_K \\ C_K & D_K \end{bmatrix} \begin{bmatrix} x_K(t) \\ y(t) \end{bmatrix}, \tag{2.2}$$

where $x_K(t) \in \mathbb{R}^{n_k}$ is the vector of controller state variables. A static controller is a special case of a dynamic controller wherein $u_c(t) = D_K y(t)$.

The closed-loop system H shown in Figure 2.1b, resulting from the closed-loop interconnection between the nominal plant G and a controller K as shown in Figure 2.1a, is given by

$$\begin{bmatrix} \dot{x}_{CL}(t) \\ e(t) \end{bmatrix} = \begin{bmatrix} A_{CL} & B_{CL} \\ C_{CL} & D_{CL} \end{bmatrix} \begin{bmatrix} x_{CL}(t) \\ u_d(t) \end{bmatrix}, \tag{2.3}$$

with

$$\begin{aligned} A_{CL} &= \begin{bmatrix} A + B_2 D_K C_2 & B_2 C_K \\ B_K C_2 & A_K \end{bmatrix}, & B_{CL} &= \begin{bmatrix} B_1 + B_2 D_K D_{21} \\ B_K D_{21} \end{bmatrix}, \\ C_{CL} &= \begin{bmatrix} C_1 + D_{12} D_K C_2 & D_{12} C_K \end{bmatrix}, & D_{CL} &= D_{11} + D_{12} D_K D_{21}, \end{aligned} \tag{2.4}$$

where $x_{CL}(t) = \begin{bmatrix} x_{OL}(t)^T & x_K(t)^T \end{bmatrix}^T \in \mathbb{R}^n$ is the vector of closed-loop state variables and $n = n_G + n_K$.

The $\mathcal{H}_\infty$-norm of a stable linear time-invariant system, with a transfer function $H(s)$, is defined as follows [39, Chapter 4.3]:

$$\|H\|_\infty = \sup_{\omega\in\mathbb{R}} \bar{\sigma}\big(H(j\omega)\big) = \sup_{u_d\in\mathcal{L}_2\setminus\{0\}} \frac{\|e\|_2}{\|u_d\|_2},$$

where s denotes the Laplace operator. The $\mathcal{H}_\infty$-norm measures the worst-case amplification of a finite energy exogenous input signal at the performance output of the system. The $\mathcal{H}_\infty$ controller synthesis problem is to design a controller $K_{\mathcal{H}_\infty}$ of the form given in (2.2) that renders the closed-loop system H stable and satisfying $\|H\|_\infty \leq \gamma$, for some constant γ [15].

The $\mathcal{H}_\infty$ controller is synthesized by first finding the smallest feasible γ. For this purpose, the following (nonconvex) optimization problem needs to be solved [15]:

$$\begin{array}{cc} \underset{\gamma,P,A_K,B_K,C_K,D_K}{\text{minimize}} & \gamma \\ \text{subject to} & P \succ 0, \\ & \begin{bmatrix} -PA_{CL} - A_{CL}^T P & PB_{CL} & C_{CL}^T \\ B_{CL}^T P & \gamma I_{n_d} & -D_{CL}^T \\ C_{CL} & -D_{CL} & \gamma I_{n_e} \end{bmatrix} \succ 0. \end{array} \tag{2.5}$$

An alternative convex formulation of the above problem is given in [18]. For this purpose, the following matrices are defined:

$$\begin{aligned} M_P &= \begin{bmatrix} P_f & I_{n_G} \\ I_{n_G} & P_g \end{bmatrix}, \\ M_A &= \begin{bmatrix} AP_f + B_2W_f & A + B_2W_hC_2 \\ L & P_gA + W_gC_2 \end{bmatrix}, \qquad M_B = \begin{bmatrix} B_1 + B_2W_hD_{21} \\ P_gB_1 + W_gD_{21} \end{bmatrix}, \\ M_C &= \begin{bmatrix} C_1P_f + D_{12}W_f & C_1 + D_{12}W_hC_2 \end{bmatrix}, \qquad M_D = D_{11} + D_{12}W_hD_{21}, \end{aligned} \tag{2.6}$$

where $P_f \in \mathbb{S}^{n_G}$, $P_g \in \mathbb{S}^{n_G}$, $W_f \in \mathbb{R}^{n_u\times n_G}$, $W_g \in \mathbb{R}^{n_G\times n_y}$, $W_h \in \mathbb{R}^{n_u\times n_y}$, and $L \in \mathbb{R}^{n_G\times n_G}$. Then, the replacements $P \longrightarrow M_P$, $PA_{CL} \longrightarrow M_A$, $PB_{CL} \longrightarrow M_B$, $C \longrightarrow M_C$, and $D \longrightarrow M_D$ are performed to the terms in (2.5). As a result, the following convex optimization problem is obtained:

$$\begin{array}{cc} \underset{\gamma,P_f,P_g,W_f,W_g,W_h,L}{\text{minimize}} & \gamma \\ \text{subject to} & M_P \succ 0, \\ & \begin{bmatrix} -M_A - M_A^T & M_B & M_C^T \\ M_B^T & \gamma I_{n_d} & -M_D^T \\ M_C & -M_D & \gamma I_{n_e} \end{bmatrix} \succ 0. \end{array} \tag{P_1}$$

Following [40], the obtained value of γ is relaxed and the semidefinite program (P_1) is re-solved as a feasibility problem. Using the obtained matrices P_f, P_g, W_f, W_g, W_h, and L, the $\mathcal{H}_\infty$ controller $K_{\mathcal{H}_\infty}$ of order $n_k = n_G$ is constructed as follows:

$$\begin{bmatrix} D_{K_{\mathcal{H}_\infty}} & C_{K_{\mathcal{H}_\infty}} \\ B_{K_{\mathcal{H}_\infty}} & A_{K_{\mathcal{H}_\infty}} \end{bmatrix} = \begin{bmatrix} I_{n_u} & \mathbf{0} \\ B_2 & -P_g^{-1} \end{bmatrix} \begin{bmatrix} W_h & W_f \\ W_g & L - P_gAP_f \end{bmatrix} \begin{bmatrix} I_{n_y} & -C_2P_fS_f^{-1} \\ \mathbf{0} & S_f^{-1} \end{bmatrix}, \tag{2.7}$$

where

$$S_f = P_f - P_g^{-1} \succ 0.$$

2.3 Proportional Integral (PI) Control

In this section, the synthesis of a Proportional Integral (PI) controller with an $\mathcal{H}_\infty$ performance specification is presented.

Consider the system G given in (2.1). Further assume that $D_{11} = \mathbf{0}$ and $D_{21} = \mathbf{0}$. A PI controller has the form

$$u_c(t) = K_P y(t) + K_I \int_0^t y(t)\mathrm{d}t, \tag{2.8}$$

where K_P and K_I are the proportional and integral gains, respectively.

To find the gains K_P and K_I, an algorithm based on an iterative Linear Matrix Inequality (LMI) technique is presented in [9]. Three different LMI conditions are presented in [9] for designing stabilizing controllers, controllers with $\mathcal{H}_\infty$ performance specification, and controllers with $\mathcal{H}_2$ performance specification. In this thesis, the $\mathcal{H}_\infty$ LMI condition is used. For this purpose, an alternative system G_{SOF} is considered by defining the state vector $\tilde{x}(t) = \begin{bmatrix}\tilde{x}_1(t)^T & \tilde{x}_2(t)^T\end{bmatrix}^T \in \mathbb{R}^{n_G+n_y}$ as

$$\begin{aligned}\tilde{x}_1(t) &= x_{OL}(t),\\ \tilde{x}_2(t) &= \int_0^t y(t)\mathrm{d}t,\end{aligned}$$

and the output vector $\tilde{y}(t) = \begin{bmatrix}\tilde{y}_1(t)^T & \tilde{y}_2(t)^T\end{bmatrix}^T \in \mathbb{R}^{2n_y}$ as

$$\begin{aligned}\tilde{y}_1(t) &= y(t),\\ \tilde{y}_2(t) &= \int_0^t y(t)\mathrm{d}t.\end{aligned}$$

Then, the new system G_{SOF} has the form

$$\begin{bmatrix}\dot{\tilde{x}}(t)\\ e(t)\\ \tilde{y}(t)\end{bmatrix} = \begin{bmatrix}\tilde{A} & \tilde{B}_1 & \tilde{B}_2\\ \tilde{C}_1 & \mathbf{0} & \tilde{D}_{12}\\ \tilde{C}_2 & \mathbf{0} & \mathbf{0}\end{bmatrix}\begin{bmatrix}\tilde{x}(t)\\ u_d(t)\\ u_c(t)\end{bmatrix}, \tag{2.9}$$

where

$$\tilde{A} = \begin{bmatrix}A & \mathbf{0}\\ C_2 & \mathbf{0}\end{bmatrix}, \qquad \tilde{B}_1 = \begin{bmatrix}B_1\\ \mathbf{0}\end{bmatrix}, \qquad \tilde{B}_2 = \begin{bmatrix}B_2\\ \mathbf{0}\end{bmatrix},$$
$$\tilde{C}_1 = \begin{bmatrix}C_1 & \mathbf{0}\end{bmatrix}, \qquad \tilde{D}_{12} = D_{12}, \qquad \tilde{C}_2 = \begin{bmatrix}C_2 & \mathbf{0}\\ \mathbf{0} & I_{n_y}\end{bmatrix}.$$

Thus, the problem of designing a PI controller of the form given in (2.8) for the system G given in (2.1) reduces to finding a static output feedback (SOF) controller of the form $u_c(t) = K_{PI}\tilde{y}(t)$, where $K_{PI} = \begin{bmatrix}K_P & K_I\end{bmatrix}$, for the new system G_{SOF} given in (2.9). Then, the feedback gains are computed using the iterative algorithm proposed in [9]. The resulting closed-loop system has the form

$$\begin{bmatrix}\dot{\tilde{x}}_{CL}(t)\\ e(t)\end{bmatrix} = \begin{bmatrix}\tilde{A}_{CL} & \tilde{B}_{CL}\\ \tilde{C}_{CL} & \tilde{D}_{CL}\end{bmatrix}\begin{bmatrix}\tilde{x}_{CL}(t)\\ u_d(t)\end{bmatrix}, \tag{2.10}$$

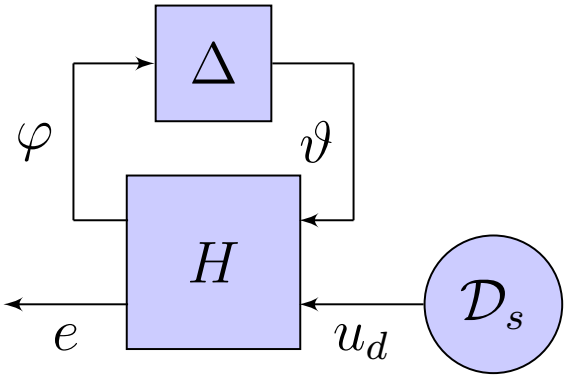

Figure 2.2: Block diagram of the uncertain system $(H, \mathbf{\Delta})$.

with

$$\begin{aligned} \tilde{A}_{CL} &= \tilde{A} + \tilde{B}_2 K_{PI} \tilde{C}_2, & \tilde{B}_{CL} &= \tilde{B}_1, \\ \tilde{C}_{CL} &= \tilde{C}_1 + \tilde{D}_{12} K_{PI} \tilde{C}_2, & \tilde{D}_{CL} &= \tilde{D}_{11}. \end{aligned} \tag{2.11}$$

2.4 Integral Quadratic Constraints

The Integral Quadratic Constraints (IQCs) framework [26] provides a method for representing real-world complex and uncertain dynamical systems in a form that is convenient for stability and performance analysis. Consider the block diagram given in Figure 2.2 depicting an uncertain system. This system comprises a stable nominal linear time-invariant system H connected to a perturbation operator Δ, representing nonlinearities, time-varying coefficients, parametric uncertainties, and unmodeled dynamics [27]. In addition, the uncertain system has an exogenous input signal $u_d \in \mathcal{D}_s \subseteq \mathcal{L}_2$. In general, mathematical descriptions of block Δ and set $\mathcal{D}_s$ are very complicated, which makes the performance analysis problem very difficult. In the IQC framework, block Δ and set $\mathcal{D}_s$ are replaced by an IQC characterization. As a result of the IQC relaxation, the relaxed model contains all of the possible solutions of the uncertain system. With this approximation, the performance analysis problem becomes easier and convex optimization can be used to solve the performance analysis problem. The reader is referred to [26]–[30] for a detailed description of the Integral Quadratic Constraints framework, as well as the IQC characterizations of various types of uncertainties.

The operator Δ is a bounded causal operator on $\mathcal{L}_2$, and Δ lies in a pre-specified set $\mathbf{\Delta}$, i.e, $\Delta \in \mathbf{\Delta}$. The uncertain system $(H, \mathbf{\Delta})$, depicted in Figure 2.2, has the form

$$\begin{bmatrix} \varphi \\ e \end{bmatrix} = H \begin{bmatrix} \vartheta \\ u_d \end{bmatrix}, \ \vartheta = \Delta\varphi, \ H = \begin{bmatrix} H_{11} & H_{12} \\ H_{21} & H_{22} \end{bmatrix}.$$

This system is stable if $(I - H_{11}\Delta)^{-1}$ is a bounded causal operator on $\mathcal{L}_2$ for all $\Delta \in \mathbf{\Delta}$ [26]. The system $(H, \mathbf{\Delta})$ is said to have a robust $\mathcal{D}_s$-to-$\mathcal{L}_2$-gain performance level of γ if it is stable and $\|(H, \Delta)\|_{\mathcal{D}_s \to \mathcal{L}_2} < \gamma$ for all $\Delta \in \mathbf{\Delta}$ and $u_d \in \mathcal{D}_s$, i.e., $||(H, \Delta)u_d||_{\mathcal{L}_2} < \gamma ||u_d||_{\mathcal{D}_s}$.

An uncertainty $\Delta \in \mathbf{\Delta}$ can be characterized by an IQC multiplier, and a set of signals $\mathcal{D}_s \subseteq \mathcal{L}_2$ can be characterized by a signal IQC multiplier [29]. An operator Δ satisfies the IQC defined by the IQC multiplier $\Pi = \Pi^* \in \mathcal{RL}_\infty$ if

$$\int_{-\infty}^{+\infty} \begin{bmatrix} \hat{\varphi}(j\omega) \\ \hat{\vartheta}(j\omega) \end{bmatrix}^* \Pi(j\omega) \begin{bmatrix} \hat{\varphi}(j\omega) \\ \hat{\vartheta}(j\omega) \end{bmatrix} d\omega \geq 0,$$

for all $\varphi \in \mathcal{L}_2$ and $\vartheta = \Delta\varphi$, where $\hat{\varphi}$ and $\hat{\vartheta}$ are the Fourier transforms of φ and ϑ, respectively. A set of signals $\mathcal{D}_s$ satisfies the signal IQC defined by the IQC multiplier $\Phi = \Phi^* \in \mathcal{RL}_\infty$ if

$$\int_{-\infty}^{+\infty} \hat{u}_d(j\omega)^* \Phi(j\omega) \hat{u}_d(j\omega) d\omega \geq 0,$$

for all $u_d \in \mathcal{D}_s$, where $\hat{u}_d$ is the Fourier transform of u_d.

Robust Performance Theorem [26, Theorem 1]: The system $(H, \mathbf{\Delta})$ has a robust $\mathcal{D}_s$-to-$\mathcal{L}_2$-gain performance level of γ if for all $\epsilon \in \begin{bmatrix} 0 & 1 \end{bmatrix}$, $(H, \epsilon\mathbf{\Delta})$ is well-posed, $\epsilon\mathbf{\Delta}$ satisfies the IQC defined by Π, $\mathcal{D}_s$ satisfies the signal IQC defined by Φ, and

$$\begin{bmatrix} H(j\omega) \\ I \end{bmatrix}^* \tilde{\Pi}(j\omega) \begin{bmatrix} H(j\omega) \\ I \end{bmatrix} \preceq -\epsilon I, \tag{2.12}$$

for all $\omega \in \mathbb{R}$, where $\epsilon > 0$, and $\tilde{\Pi}$ is defined as follows:

$$\tilde{\Pi} = \begin{bmatrix} \Pi_{11} & \mathbf{0} & \Pi_{12} & \mathbf{0} \\ \mathbf{0} & I & \mathbf{0} & \mathbf{0} \\ \Pi_{12}^* & \mathbf{0} & \Pi_{22} & \mathbf{0} \\ \mathbf{0} & \mathbf{0} & \mathbf{0} & -\gamma^2 I + \Phi \end{bmatrix}.$$

SDP Formulation: The multiplier $\Pi(s)$ can be factorized as $\Pi(s) = \psi(s)^* \mathcal{S} \psi(s)$, where $\psi(s) \in \mathcal{RH}_\infty$ is a transfer function matrix typically chosen a priori. Similarly, the signal IQC multiplier $\Phi(s)$ can be factorized as $\Phi(s) = \theta(s)^* \mathcal{R} \theta(s)$, where $\theta(s) \in \mathcal{RH}_\infty$. Therefore, a convex optimization problem can be formulated to solve for an upper bound γ on the robust $\mathcal{D}_s$-to-$\mathcal{L}_2$-gain performance level by utilizing the Kalman–Yakubovich–Popov (KYP) Lemma [41] to express (2.12) as a linear matrix inequality. To find γ, the following semidefinite program (SDP) is solved:

$$\begin{aligned} \underset{\tilde{S}, P, \gamma^2}{\text{minimize}} \quad & \gamma^2 \\ \text{subject to} \quad & P = P^T, \\ & \begin{bmatrix} \mathcal{A}^T P + P\mathcal{A} & P\mathcal{B} \\ \mathcal{B}^T P & \mathbf{0} \end{bmatrix} + \begin{bmatrix} \mathcal{C}^T \\ \mathcal{D}^T \end{bmatrix} \tilde{S} \begin{bmatrix} \mathcal{C} & \mathcal{D} \end{bmatrix} \prec 0, \end{aligned} \tag{P_2}$$

where

$$\tilde{S} = \begin{bmatrix} \mathcal{S}_{11} & \mathbf{0} & \mathcal{S}_{12} & \mathbf{0} & \mathbf{0} \\ \mathbf{0} & I_{n_e} & \mathbf{0} & \mathbf{0} & \mathbf{0} \\ \mathcal{S}_{12}^T & \mathbf{0} & \mathcal{S}_{22} & \mathbf{0} & \mathbf{0} \\ \mathbf{0} & \mathbf{0} & \mathbf{0} & \mathcal{R} & \mathbf{0} \\ \mathbf{0} & \mathbf{0} & \mathbf{0} & \mathbf{0} & -\gamma^2 I_{n_s} \end{bmatrix},$$

and n_s is the number of exogenous inputs. The realization $(\mathcal{A}, \mathcal{B}, \mathcal{C}, \mathcal{D})$ is defined as

$$\mathcal{D} + \mathcal{C}(sI - \mathcal{A})^{-1} = \tilde{\Psi}(s) \begin{bmatrix} H(s) \\ I \end{bmatrix}, \tag{2.13}$$

where

$$\tilde{\Psi}(s) = \begin{bmatrix} \psi_{11}(s) & \mathbf{0} & \psi_{12}(s) & \mathbf{0} \\ \mathbf{0} & I & \mathbf{0} & \mathbf{0} \\ \psi_{21}(s) & \mathbf{0} & \psi_{22}(s) & \mathbf{0} \\ \mathbf{0} & \mathbf{0} & \mathbf{0} & \theta(s) \\ \mathbf{0} & \mathbf{0} & \mathbf{0} & I \end{bmatrix}.$$

Parametrization of the IQC Multiplier for Static Linear Time-varying (SLTV) Parameters: In this thesis, the IQC characterization of static linear time-varying parameters is of interest. Let $\vartheta(t) = \Delta\varphi(t)$, where Δ is a block of diagonally repeated bounded time-varying parameters $\delta(t)$. Then, $\Delta \in \mathbf{\Delta}$, where the set $\mathbf{\Delta}$ is defined as

$$\mathbf{\Delta} = \{\Delta : \vartheta(t) = \Delta\varphi(t) \text{ and } |\delta(t)| \leq \alpha\}.$$

This set $\mathbf{\Delta}$ is characterized by a class of IQC multipliers $\Pi(s) = \Pi(s)^* \in \mathcal{RL}_\infty$. A parameterization of $\Pi(s)$ given in [31] is $\Pi(s) = \psi(s)^* \mathcal{S} \psi(s)$, where

$$\psi = \begin{bmatrix} \alpha I_{n_\vartheta} & 0 \\ 0 & I_{n_\vartheta} \end{bmatrix}, \mathcal{S} = \begin{bmatrix} X & Y \\ Y^T & -X \end{bmatrix},$$

with $X \succeq 0$ and $Y = -Y^T \in \mathbb{R}^{n_\vartheta \times n_\vartheta}$.

Parametrization of the Signal IQC Multiplier for White Noise Signals: In this thesis, the IQC characterization of white noise signals is of interest. White signals can be represented as signals in $\mathcal{L}_2$ with a flat power spectral density over a large frequency range [29]. The set of white signals will be denoted by $\mathcal{D}_w$, and a white signal $w_w \in \mathcal{D}_w \subseteq \mathcal{L}_2$ satisfies

$$|\hat{w}_w(j\omega)|^2 = \begin{cases} \frac{\pi}{b}\|w_w\|_2^2, & w_w \in [-b, b], \\ 0, & |w_w| > b. \end{cases}$$

This is depicted in Figure 2.3. The set of white signals $\mathcal{D}_w$ is characterized by a class of signal IQC multipliers $\Phi_w(s) = \Phi_w(s)^* \in \mathcal{RL}_\infty$ that satisfy $\int_{-b}^{b} \mathbf{tr}\big(\Phi_w(j\omega)\big) d\omega \geq 0$ [29]. A parameterization of $\Phi_w(s)$ given in [29] is $\Phi_w(s) = Y(s) + Y(s)^*$, with

$$Y(s) = x_0 + \sum_{i=1}^{N} \frac{x_i}{s + a_i},$$

where x_0, $x_i \in \mathbb{R}$ are the decision variables, and the poles a_i are distinct with positive real parts. This parameterization allows for the following factorization

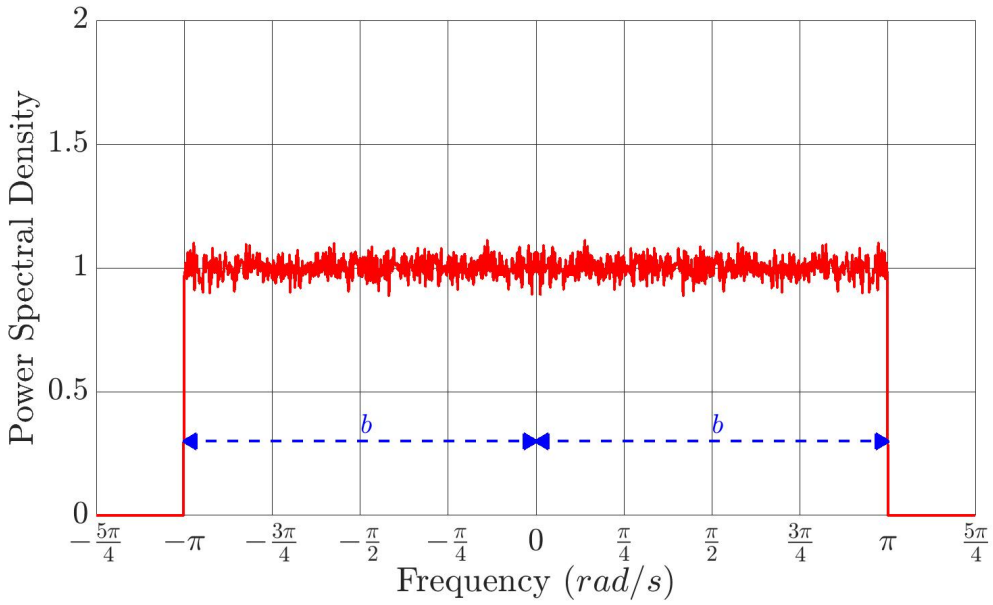

Figure 2.3: Power spectral density of white noise signals.

$\Phi_w(s) = \theta(s)^* \mathcal{R} \theta(s)$, where

$$\begin{aligned} \theta(s) &= \begin{bmatrix} (sI - A_Y)^{-1} B_Y \\ I \end{bmatrix}, \ \mathcal{R} = \begin{bmatrix} \mathbf{0}_{N\times N} & C_Y^T \\ C_Y & 2D_Y \end{bmatrix}, \\ A_Y &= -\mathbf{diag}(a_1, \cdots, a_N), \ B_Y = [1, \cdots, 1]^T, \\ C_Y &= \begin{bmatrix} x_1, \cdots, x_N \end{bmatrix}, \ D_Y = x_0. \end{aligned} \tag{2.14}$$

Moreover, the following characterization of the constraint $\int_{-b}^{b} \mathbf{tr}\big(\Phi_w(j\omega)\big) d\omega \geq 0$ is obtained [29]:

$$b x_0 + \sum_{i=1}^{N} x_i \mathbf{tan}^{-1}\left(\frac{b}{a_i}\right) \geq 0. \tag{2.15}$$

Chapter 3

CONTROL-THEORETIC MODELING OF WIND TURBINES

In this chapter, an overview of the modeling of horizontal-axis, three-bladed, pitch-controlled, variable-speed wind turbines is presented.

3.1 Overview of a Wind Turbine Model and Basic Operations

Wind Turbine Components: A horizontal-axis wind turbine is composed of a rotor connected to the nacelle, which is mounted on the wind turbine tower. The nacelle houses the generator, low- and high-speed shafts, and the gear box. The rotor consists of the wind turbine blades that rotate as a result of the lift generated by the wind. The rotor is connected to the low-speed shaft which rotates and drives the high-speed shaft. The two shafts are connected through a gear box that steps up the rotational speed. The high-speed shaft drives the generator which converts the rotational kinetic energy to electric energy [3]. A schematic diagram showing the various components of the wind turbine is presented in Figure 3.1.

Wind Turbines Actuators and Sensors: Wind Turbines have three different types of actuators. The first type is the yaw motor which turns the nacelle to align the rotor with the incoming wind flow. To avoid dangerous gyroscopic forces, the yaw is limited to a rate of less than 1 deg/s. The second type is the generator, which can command a desired torque used to accelerate or decelerate the rotor. The third type is the blade pitch motor. Each blade of the wind turbine has a pitch actuator, and the three pitch angles can be controlled either collectively or individually [3].

The yaw actuator operates at a much slower time-scale compared to the generator and pitch actuators, and therefore, yaw control is of less interest to control engineers [3], [14], [25]. In this thesis, a yaw controller will not be designed, and the yaw angle will be always held constant such that rotor plane is in the direction of the incoming

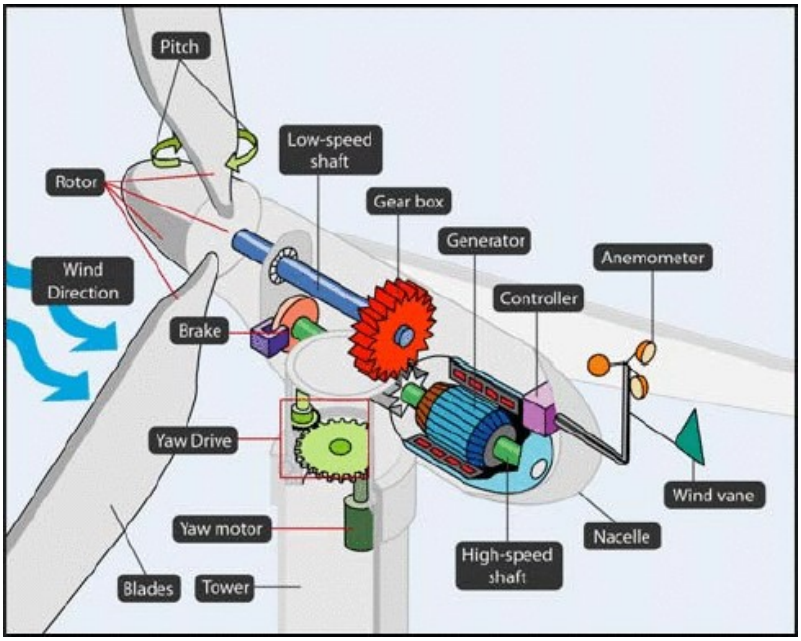

Figure 3.1: Wind turbine components [3].

wind. Therefore, only the generator torque and blade pitch controllers are of interest in this thesis. Moreover, collective pitch control will be considered.

Wind turbines use two types of sensors. First, there are sensors that measure the generator or the rotor speed, and these measurements are used for the feedback control of wind turbines. Second, there is the anemometer, mounted on the top of the nacelle, used to measure the wind speed. However, these measurements are corrupted by the interaction between the blades and the incoming wind, and therefore, they are not used for control purposes [3].

Aerodynamic Efficiency of a Wind Turbine: A wind turbine is not capable of capturing all of the available power in the wind. An incoming wind flow must have some remaining kinetic energy after passing through the turbine's rotor; otherwise, the wind would "stop" and would not leave the region of the turbine. In this sense, the aerodynamic efficiency of a wind turbine is defined as the proportion of the power available in the wind that is captured by the turbine. The maximum theoretical value of the aerodynamic efficiency, known as Betz Limit, is approximately 59% [42]. Specifically, the aerodynamic efficiency of a wind turbine is defined as

$$C_P = \frac{P_r}{P_{wind}},$$

where P_r is the rotor power, i.e., the power captured by the turbine, and P_{wind} is the power available in the wind. P_{wind} is given by

$$P_{wind} = \frac{1}{2}\rho A_r v^3,$$

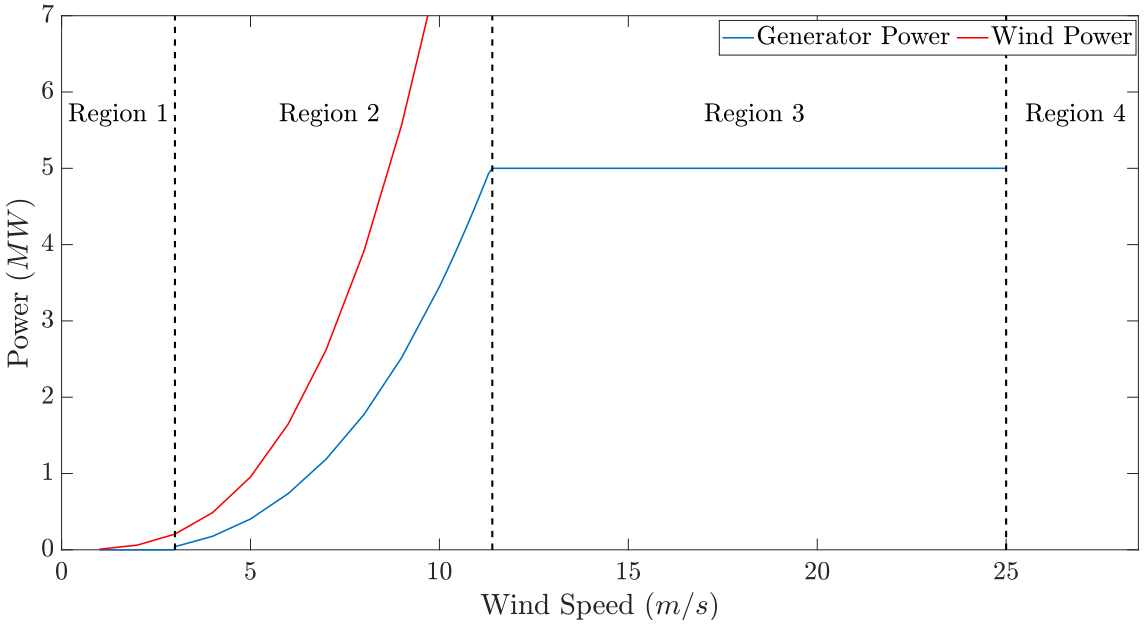

Figure 3.2: Generator power versus wind speed curve for the NREL $5-MW$ wind turbine. The data used to generate this plot is from [43].

where ρ is the density of air, $A_r = \pi R_r^2$ is the rotor area, R_r is the rotor radius, and v is the wind speed. The generator power P_g is then expressed as $P_g = \eta_g P_r$, where η_g is the efficiency of the electrical generator.

The aerodynamic efficiency is a function of the turbine's tip-speed ratio λ and the blade pitch angle β. The tip-speed ratio λ is defined as

$$\lambda = \frac{\omega_r R_r}{v},$$

where ω_r is the rotor rotational speed. The relation between the parameters (C_P, λ, β) is described by a turbine-specific nonlinear function [42]. The maximum aerodynamic efficiency of a wind turbine, denoted by $C_{P_{max}}$, corresponds to operating the turbine at an optimal tip-speed ratio λ_* and optimal pitch angle β_*.

The rotor power of the wind turbine can be expressed as $P_r = \tau_r \omega_r$, where τ_r is the aerodynamic/rotor torque. However, the generator torque τ_g is of interest in the wind turbine control system. It is the torque of the high-speed shaft transmitted through the drive train, i.e., $\tau_g = \eta_g \frac{\tau_r}{N_g}$, where N_g is the gear box ratio. Assuming that the drive train has a mechanical efficiency of 100%, i.e., $\eta_g = 1$, an expression of the generator torque can then be obtained as follows:

$$\begin{aligned}\tau_g &= \frac{\tau_r}{N_g} = \frac{P_r}{N_g \omega_r} = \frac{C_P P_{wind}}{N_g \omega_r} = \frac{C_P \rho \pi R_r^2 v^3}{2 N_g \omega_r} \\ &= \frac{\pi}{2} \frac{\rho R_r^5}{N_g} \frac{C_P}{\lambda^3} \omega_r^2.\end{aligned}$$

Wind Turbine Control Objectives: The objective of the wind turbine controller varies in the different wind speed regions. As shown in the power versus wind speed curve in Figure 3.2, a wind turbine has four operating regions: Region 1 for wind speeds below the cut-in speed, Region 2 for wind speeds between the cut-in and rated speeds, Region 3 for wind speeds between the rated and cut-off speeds, and Region 4 for wind speeds above the cut-off speed [3]. This figure pertains to the NREL $5-MW$ reference wind turbine considered in thesis. Further details on this wind turbine are presented in Section 3.2. In Region 1, the turbine does not rotate as the power available in the wind is insufficient. In Region 2, the power available in the wind is less than the rated power of the wind turbine, and thus, the objective of the controller is to extract the maximum of the available power. This can be accomplished by using a generator torque controller that tracks a rotational speed reference. In this region, the pitch angle is held constant at the value of maximum aerodynamic efficiency [42]. In Region 3, the main objective of the controller is to maintain the generated power to its rated value and minimize the structural loads on the turbine. This can be accomplished by using a blade pitch controller that increases the pitch angle as the wind speed increases to lower the aerodynamic efficiency, and hence, limit the generated power. In this region, the generator torque is held constant at its rated value [44]. A transition region between Regions 2 and 3, referred to as Region 2.5, is usually introduced to ensure a smooth transition between the two regions [3]. In Region 4, the turbine is shut down to prevent structural damages. In this thesis, the emphasis is on Region 3 of the wind turbine operation. Therefore, the generator torque is held constant at its rated value, and a blade pitch controller is designed. Collective blade pitch is used.

3.2 NREL 5-MW Reference Wind Turbine

In this thesis, the specific wind turbine model that will be used for simulations is the NREL $5-MW$ reference wind turbine. It is a representative utility-scale, multi-megawatt wind turbine proposed by the National Renewable Energy Laboratory (NREL) as a standardized, well-documented wind turbine model. It is a conventional horizontal-axis, three-bladed, variable-speed, pitch-controlled turbine that can be configured in an onshore setting [43]. The main properties of this turbine are summarized in Table 3.1.

Table 3.1: Properties of the NREL $5-MW$ Reference Turbine [43]

Cut-In Wind Speed	3 m/s	Rated Wind Speed	11.4 m/s	Cut-Out Wind Speed	25 m/s
Cut-In Rotor Speed	6.9 RPM	Rated Rotor Speed	12.1 RPM	Rated Generator Speed	1173.7 RPM
Rated Power	5 MW	Generator Efficiency	94.4 %	Gearbox Ratio	97
Rotor Diameter	126 m	Hub Diameter	3 m	Hub Height	90 m
Rotor Mass	110,000 kg	Nacelle Mass	240,000 kg	Tower Mass	347,460 kg

3.3 High-Fidelity Simulation Model

In this section, a description of a high-fidelity wind turbine model is presented. This model is based on the OpenFAST modeling package, which is developed by NREL. OpenFAST, formerly known as FAST (Fatigue, Aerodynamics, Structures, and Turbulence), is a simulation package used to model the wind turbine nonlinear dynamics [2]. In this thesis, simulations involving control of wind turbines are executed using OpenFAST and its interface on Simulink/`MATLAB`.

3.3.1 *Overview*

OpenFAST is a high-fidelity simulation tool that models the dynamics of horizontal-axis wind turbines. In OpenFAST, the wind turbine components are modeled as flexible structures. The drive train is modeled as a spring-mass-damper system, and the tower and blades are treated as cantilever beams. Computations of deformations along these flexible structures are based on modal analysis, whereby the tower and blades are discretized into a grid of modes [2].

The dynamics of three-bladed onshore wind turbines are modeled using OpenFAST with up to 18 degrees of freedom. Four DOFs correspond to the tower dynamics. These DOFs are the first and second tower bending modes in fore-aft and side-to-side directions. Three DOFs correspond to the dynamics of each of the three blades. These DOFs are the first and second flap-wise bending modes and the first edge-wise bending mode. The drive train dynamics are modeled using two DOFs: the torsion and the generator speed. In addition, one DOF corresponds to the yaw motion of the nacelle, and two other DOFs correspond to the rotor and tail furl [2].

Therefore, the nonlinear model of the wind turbine may have up to 36 state variables, which correspond to the 18 DOFs in OpenFAST and their first time derivatives. However, it is common practice to model the wind turbine in OpenFAST with a smaller number of DOFs. That is, for control synthesis purposes, a lower order wind turbine nonlinear, and consequently linearized, model is used. There are up to five control inputs: the pitch angle of each of the three blades, generator torque, and yaw angle. The wind turbine model has seven exogenous inputs to describe the wind disturbance: hub-height average wind speed, horizontal wind direction, vertical wind speed, horizontal wind shear, vertical power law wind shear, linear vertical wind shear, and horizontal hub-height wind gust. These seven parameters are inputs to the TurbSim module that generates the hub-height wind profile [2].

The nonlinear model of the wind turbine can be expressed as

$$\dot{x}^{WT}(t) = f_1\big(x^{WT}(t), u_c^{WT}(t), u_d^{WT}(t), t\big),$$
$$y^{WT}(t) = f_2\big(x^{WT}(t), u_c^{WT}(t), u_d^{WT}(t), t\big),$$

where $x^{WT}(t) \in \mathbb{R}^{n_G}$ is the vector of state variables of the wind turbine model, $u_c^{WT}(t) \in \mathbb{R}^{n_c}$ is the vector of control inputs, $u_d^{WT(t)} \in \mathbb{R}^{n_d}$ is the vector of wind disturbance inputs, and $y^{WT}(t)$ is the vector of outputs. The outputs are specified by the user from a list of available outputs in OpenFAST. These outputs include

the generator and rotor speeds, as well as loads and moments on the different wind turbine components [2].

3.3.2 *Linearization*

For the purpose of controller synthesis and performance analysis, the linearization framework in OpenFAST is used to obtain a linear time-invariant wind turbine model at a given operating wind speed. This is done by simulating the nonlinear model at the given steady wind speed $\bar{u}_d^{WT}$ until a steady-state periodic operating point $\bar{x}^{WT}(t)$ is achieved, with the control inputs held constant at their operating values $\bar{u}_c^{WT}$ that stabilize the rotor speed at its operating value. Since the operating point is periodic, the simulation is repeated for multiple azimuth angles. A periodic linear time-varying (PLTV) model is obtained. It has the form

$$\begin{bmatrix} \Delta\dot{x}^{WT}(t) \\ \Delta y^{WT}(t) \end{bmatrix} = \begin{bmatrix} A^{WT}(\bar{x}^{WT}(t)) & B_1^{WT}(\bar{x}^{WT}(t)) & B_2^{WT}(\bar{x}^{WT}(t)) \\ C^{WT}(\bar{x}^{WT}(t)) & D_1^{WT}(\bar{x}^{WT}(t)) & D_2^{WT}(\bar{x}^{WT}(t)) \end{bmatrix} \begin{bmatrix} \Delta x^{WT}(t) \\ \Delta u_d^{WT}(t) \\ \Delta u_c^{WT}(t) \end{bmatrix},$$

where $\Delta x^{WT}(t) = x^{WT}(t) - \bar{x}^{WT}(t)$, $\Delta y^{WT}(t) = y^{WT}(t) - \bar{y}^{WT}(t)$, $\Delta u_d^{WT}(t) = u_d^{WT}(t) - \bar{u}_d^{WT}$, and $\Delta u_c^{WT}(t) = u_c^{WT}(t) - \bar{u}_c^{WT}$.

Multi-Blade Coordinate (MBC) Transformation:
The obtained PLTV model has to be approximated with a linear time-invariant (LTI) model without losing the physical interpretation of the states of the system. Hence, the multi-blade coordinate (MBC) transformation is applied on the obtained state-space matrices to generate a weakly PLTV system. Namely, the wind turbine model is defined in more than one coordinate system, i.e., the DOFs corresponding to the turbine tower, drive train, and generator are defined in a fixed nonrotating frame, while the DOFs corresponding to the turbine blades are defined in a rotating frame. Hence, the MBC transformation is applied on the states, inputs, and outputs of the system to transform them into a nonrotating frame [45].

For a given rotor position ψ, the MBC transformation is defined by a matrix $T_{MBC}(\psi)$ that transforms the quantities that are in the rotating frame, i.e., quantities associated with turbine blades, to the nonrotating frame. The matrix $T_{MBC}(\psi)$ is given by

$$T_{MBC}(\psi) = \begin{bmatrix} \frac{1}{2} & \frac{1}{2} & \frac{1}{2} \\ \mathbf{cos}(\psi) & \mathbf{cos}(\psi + \frac{2\pi}{3}) & \mathbf{cos}(\psi + \frac{4\pi}{3}) \\ \mathbf{sin}(\psi) & \mathbf{sin}(\psi + \frac{2\pi}{3}) & \mathbf{sin}(\psi + \frac{4\pi}{3}) \end{bmatrix}.$$

After this transformation, rotating quantities associated with the three blades of the wind turbine, for instance the blades flap-wise bending moments, are converted into quantities that have an interpretation in terms of the rotor motion instead of the individual blades. The converted quantities consist of one symmetric and two asymmetric components. The symmetric component results from the blades bending in the same direction, and it is the average value of the moment experienced by the

rotor. The asymmetric components correspond to the out-of-phase bending of the blades and result in the yaw and tilt bending of the rotor [46].

An LTI system is obtained by azimuth-averaging the weakly PLTV system (the MBC-transformed state-space matrices). In this approach, the LTI system retains many of the periodic properties of the wind turbine model [45]. To test the obtained linearized time-invariant models, simulations of the open-loop LTI and nonlinear wind turbine models are performed. The turbulence is set to zero, and the pitch angle is set to zero before the instant $20s$ and 1° afterwards. The responses of the rotor speed, flap-wise bending moment of the first blade, and tower fore-aft bending moments of linear and nonlinear models are compared. The results corresponding to the mean wind speed $v_m = 18\ m/s$ are presented in Figure 3.3, and those corresponding to $v_m = \{16, 20, 23\}\ m/s$ are presented in Figures A.1, A.2, and A.3 in Appendix A, respectively. It can be observed in Figure 3.3 that the nonlinear and linear responses of all three outputs match after steady-state is achieved.

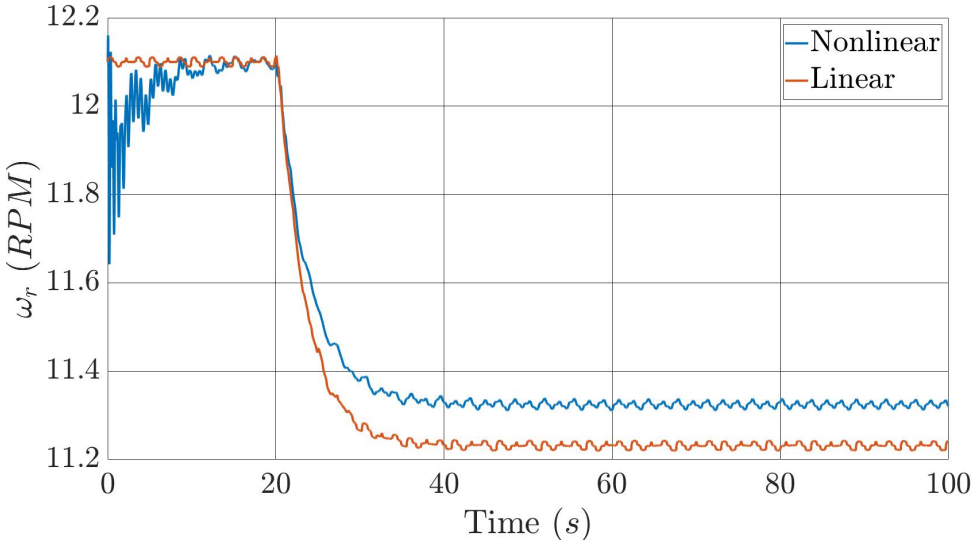

(a) Rotor speed

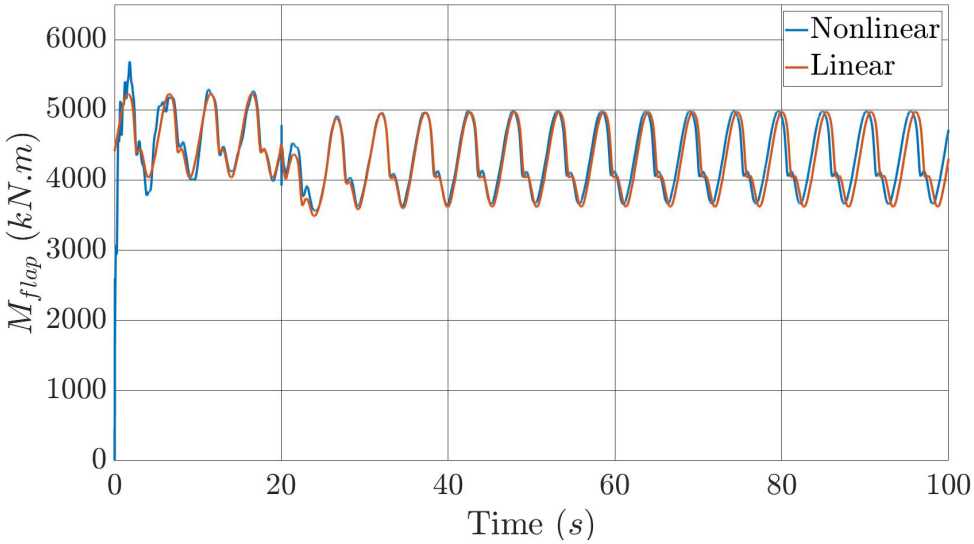

(b) Blade 1 flap-wise bending moment

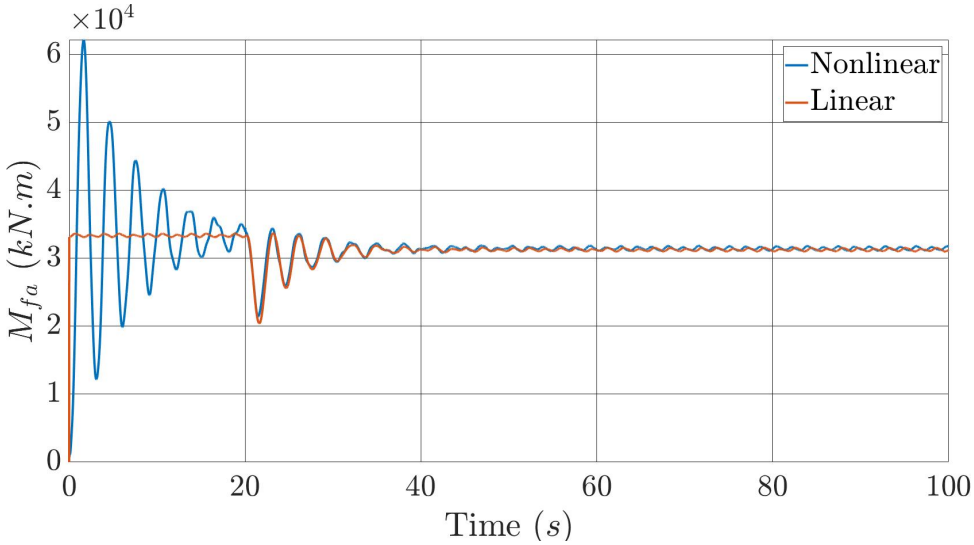

(c) Tower fore-aft bending moment

Figure 3.3: Open-loop simulation results at $v_m = 18\ m/s$.

3.4 Pitch Actuator Dynamics

The wind turbine blades pitch actuator dynamics are not modeled within the OpenFAST simulation package. Therefore, in this thesis, a blade pitch actuator model is connected to the wind turbine open-loop model. The dynamics of the blade pitch actuator are modeled as a second-order system of the form

$$\frac{\beta(s)}{\beta_r(s)} = \frac{\omega_n^2}{s^2 + 2\zeta\omega_n s + \omega_n^2},$$

where β is the actual blade pitch angle and β_r is the pitch reference outputted from the pitch controller, i.e., $\beta_r(t) = u_c(t)$. The parameters ζ and ω_n are set as $\zeta = 0.6$ and $\omega_n = 11.11\ rad/s$ [47]. Defining the state vector $x_p(t) = \begin{bmatrix}\beta(t) & \dot{\beta}(t)\end{bmatrix}^T \in \mathbb{R}^2$, the blade pitch actuator model can be equivalently represented as

$$\begin{bmatrix} \dot{x}_p(t) \\ \beta(t) \end{bmatrix} = \begin{bmatrix} A_p & B_p \\ C_p & D_p \end{bmatrix} \begin{bmatrix} x_p(t) \\ \beta_r(t) \end{bmatrix},$$

where

$$A_p = \begin{bmatrix} 0 & 1 \\ -\omega_n^2 & -2\zeta\omega_n \end{bmatrix},\ B_p = \begin{bmatrix} 0 \\ \omega_n^2 \end{bmatrix},\ C_p = \begin{bmatrix} 1 & 0 \end{bmatrix},\ D_p = 0.$$

Thus, the wind turbine LTI model featuring the actuator dynamics is given by the following open-loop system equations:

$$\begin{bmatrix} \dot{\hat{x}}_{OL}(t) \\ e(t) \\ y(t) \end{bmatrix} = \begin{bmatrix} \hat{A} & \hat{B}_1 & \hat{B}_2 \\ \hat{C}_1 & \hat{D}_{11} & \hat{D}_{12} \\ \hat{C}_2 & \hat{D}_{21} & \mathbf{0} \end{bmatrix} \begin{bmatrix} \hat{x}_{OL}(t) \\ u_d(t) \\ \beta(t) \end{bmatrix},$$

with

$$\hat{A} = \begin{bmatrix} A & B_2 & \mathbf{0} \\ \mathbf{0} & 0 & 1 \\ \mathbf{0} & -\omega_n^2 & -2\zeta\omega_n \end{bmatrix}, \quad \hat{B}_1 = \begin{bmatrix} B_1 \\ 0 \\ 0 \end{bmatrix}, \quad \hat{B}_2 = \begin{bmatrix} \mathbf{0} \\ 0 \\ w_n^2 \end{bmatrix},$$
$$\hat{C}_1 = \begin{bmatrix} C_1 & D_{12} & \mathbf{0} \end{bmatrix}, \quad \hat{D}_{11} = D_{11}, \quad \hat{D}_{12} = \mathbf{0},$$
$$\hat{C}_2 = \begin{bmatrix} C_2 & \mathbf{0} & \mathbf{0} \end{bmatrix}, \quad \hat{D}_{21} = D_{21},$$

where $\hat{x}_{OL}(t) = \begin{bmatrix} x_{OL}(t)^T & x_p(t)^T \end{bmatrix}^T \in \mathbb{R}^{n_G+2}$ is the vector of state variables.

3.5 Wind Model

The wind model considered in this thesis is based on the work of Langreder in [5] and is shown in Figure 3.4a. The reader is referred to [5] for further details on the wind model and the individual filters of the model.

This wind model relies on Kaimal's characterization of turbulence, whereby stationary turbulent winds are generated by filtering white noise signals (w_{w_1},w_{w_2},w_{w_3})

Table 3.2: Transfer function coefficients of the Kaimal and harmonic filters. These numbers are from [5].

κ_1	0.0182	κ_6	4.7869	κ_{11}	0.0307
κ_2	1.3653	κ_7	0.9904	κ_{12}	0.3691
κ_3	0.9846	κ_8	7.6823	κ_{13}	1.7722
κ_4	1.3463	κ_9	7.3518		
κ_5	3.7593	κ_{10}	0.2766		

through a Kaimal Filter ($KF(s)$). This filter is based on a fitting of the turbulent wind power spectra. The obtained fixed-point turbulence outputs (v_{c_1},v_{c_2},v_{c_3}) are then passed through admittance filters ($HF_1(s)$ and $HF_2(s)$) that output rotationally sampled turbulence (in the rotating frame of the rotor). In addition, the aerodynamic loading effect of the entire wind field is lumped into a single equivalent wind speed. Two admittance filters are included in the model, which capture the frequency components of turbulent winds that correspond to the 0^{th} harmonic ($HF_1(s)$) and 3^{rd} harmonic ($HF_2(s)$) of the rotor speed. These two harmonics make a significant contribution to the development of the aerodynamic torque, with other harmonics having small or no contributions [5].

The equations of the wind model shown in Figure 3.4a are given by

$$\begin{aligned} KF(s) &= \frac{\kappa_1 c^2 s^2 + \kappa_2 cs + \kappa_3}{\kappa_4 c^2 s^2 + \kappa_5 cs + 1}, \; c = \frac{L_t}{2\pi v_m}, \\ K_F &= \frac{I}{100}\sqrt{\frac{v_m L_t}{2}}, \\ HF_1(s) &= \frac{\kappa_6 ds + \kappa_7}{\kappa_8 d^2 s^2 + \kappa_9 ds + 1}, \; d = \frac{R_r}{v_m}, \\ HF_2(s) &= \frac{\kappa_{10} ds + \kappa_{11}}{\kappa_{12} d^2 s^2 + \kappa_{13} ds + 1}, \end{aligned}$$

where KF is the Kaimal filter, HF_1 is the 0^{th} harmonic filter, HF_2 is the 3^{rd} harmonic filter, K_F is a normalization gain, I is the turbulence intensity, L_t is the turbulence length scale, v_m is the mean wind speed, and R_r is the turbine rotor radius. The values of $\kappa_1, \ldots, \kappa_{13}$ are given in Table 3.2.

Let $\delta_1(t) = \mathbf{cos}(3\omega_r t)$ and $\delta_2(t) = \mathbf{sin}(3\omega_r t)$. From Figure 3.4a, the output of the wind model is given by

$$v_t = v_{t_1} + v_{t_2} = HF_1 v_{c_1} + \sqrt{2}\delta_1 HF_2 v_{c_2} + \sqrt{2}\delta_2 HF_2 v_{c_3}, \tag{3.1}$$

with

$$v_{c_1} = K_F KF w_{w_1}, \; v_{c_2} = K_F KF w_{w_2}, \; v_{c_3} = K_F KF w_{w_3}.$$

After manipulating the output equation (3.1) of the wind model, the following equation is obtained:

$$v_t = K_F KF\Big(HF_1 w_{w_1} + \sqrt{2} HF_2\big(\delta_1 w_{w_2} + \delta_2 w_{w_3}\big)\Big). \tag{3.2}$$

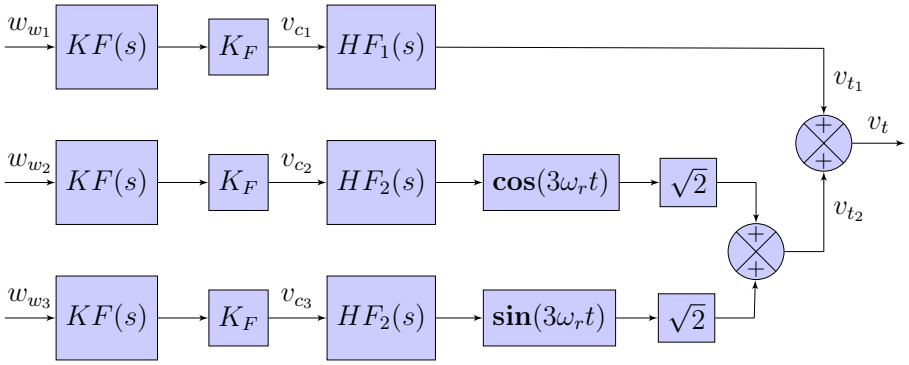

(a) Block diagram representation of the wind model.

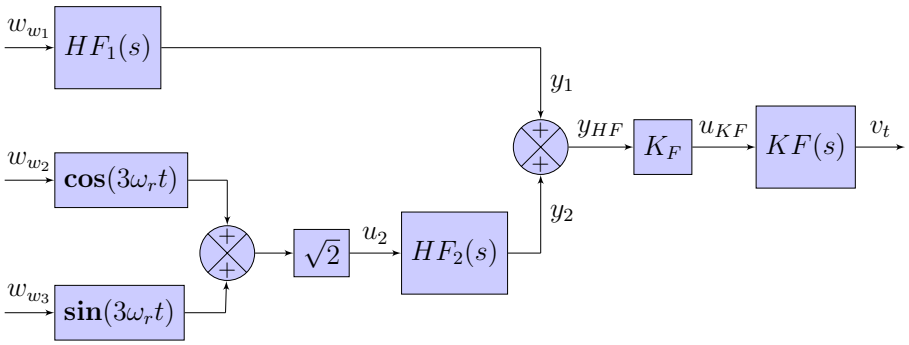

(b) Alternate block diagram representation of the wind model.

Figure 3.4: Wind model based on Kaimal's characterization of turbulence.

The output equation (3.2) of the wind model is shown in Figure 3.4b, and it used to get a minimal representation of the wind model. Namely, from Figure 3.4b, the following equations are obtained:

$$y_1 = HF_1 w_{w_1}, \; y_2 = HF_2 u_2,$$

where $u_2 = \sqrt{2}\delta_1 w_{w_2} + \sqrt{2}\delta_2 w_{w_3}$. In state-space form, the following equations are obtained:

$$\begin{bmatrix} \dot{x}_{HF_1}(t) \\ y_1(t) \end{bmatrix} = \begin{bmatrix} A_{HF_1} & B_{HF_1} \\ C_{HF_1} & D_{HF_1} \end{bmatrix} \begin{bmatrix} x_{HF_1}(t) \\ w_{w_1}(t) \end{bmatrix},$$
$$\begin{bmatrix} \dot{x}_{HF_2}(t) \\ y_2(t) \end{bmatrix} = \begin{bmatrix} A_{HF_2} & B_{HF_2} \\ C_{HF_2} & D_{HF_2} \end{bmatrix} \begin{bmatrix} x_{HF_2}(t) \\ u_2(t) \end{bmatrix},$$

where

$$A_{HF_1} = \begin{bmatrix} 0 & 1 \\ -\frac{1}{\kappa_8 d^2} & -\frac{\kappa_9}{\kappa_8 d} \end{bmatrix}, \qquad B_{HF_1} = \begin{bmatrix} 0 \\ 1 \end{bmatrix},$$
$$C_{HF_1} = \begin{bmatrix} \frac{\kappa_7}{\kappa_8 d^2} & \frac{\kappa_6}{\kappa_8 d} \end{bmatrix}, \qquad D_{HF_1} = 0,$$
$$A_{HF_2} = \begin{bmatrix} 0 & 1 \\ -\frac{1}{\kappa_{12} d^2} & -\frac{\kappa_{13}}{\kappa_{12} d} \end{bmatrix}, \qquad B_{HF_2} = \begin{bmatrix} 0 \\ 1 \end{bmatrix},$$
$$C_{HF_2} = \begin{bmatrix} \frac{\kappa_{11}}{\kappa_{12} d^2} & \frac{\kappa_{10}}{\kappa_{12} d} \end{bmatrix}, \qquad D_{HF_2} = 0.$$

A filter HF is obtained by combining the equations of the filters HF_1 and HF_2, which gives

$$\begin{bmatrix} \dot{x}_{HF}(t) \\ y_{HF}(t) \end{bmatrix} = \begin{bmatrix} A_{HF} & B_{HF}(t) \\ C_{HF} & D_{HF}(t) \end{bmatrix} \begin{bmatrix} x_{HF}(t) \\ w_w(t) \end{bmatrix},$$

where

$$\begin{aligned} A_{HF} &= \begin{bmatrix} A_{HF_1} & \mathbf{0}_{2\times 2} \\ \mathbf{0}_{2\times 2} & A_{HF_2} \end{bmatrix}, & B_{HF}(t) &= \begin{bmatrix} B_{HF_1} & \mathbf{0}_{2\times 1} & \mathbf{0}_{2\times 1} \\ \mathbf{0}_{2\times 1} & \sqrt{2}\delta_1(t)B_{HF_2} & \sqrt{2}\delta_2(t)B_{HF_2} \end{bmatrix}, \\ C_{HF} &= \begin{bmatrix} C_{HF_1} & C_{HF_2} \end{bmatrix}, & D_{HF}(t) &= \begin{bmatrix} D_{HF_1} & \sqrt{2}\delta_1(t)D_{HF_2} & \sqrt{2}\delta_2(t)D_{HF_2} \end{bmatrix}, \\ x_{HF}(t) &= \begin{bmatrix} x_{HF_1}(t)^T & x_{HF_2}(t)^T \end{bmatrix}^T, & w_w(t) &= \begin{bmatrix} w_{w_1}(t)^T & w_{w_2}(t)^T & w_{w_3}(t)^T \end{bmatrix}^T, \\ y_{HF}(t) &= y_1(t) + y_2(t). \end{aligned}$$

Moreover, from Figure 3.4b, $v_t = KFu_{KF}$, where $u_{KF} = K_F y_{HF}$. In state-space form, the following equations are obtained:

$$\begin{bmatrix} \dot{x}_{KF}(t) \\ v_t(t) \end{bmatrix} = \begin{bmatrix} A_{KF} & B_{KF} \\ C_{KF} & D_{KF} \end{bmatrix} \begin{bmatrix} x_{KF}(t) \\ u_{KF}(t) \end{bmatrix},$$

where

$$\begin{aligned} A_{KF} &= \begin{bmatrix} 0 & 1 \\ -\frac{1}{\kappa_4 c^2} & -\frac{-\kappa_5}{\kappa_4 c} \end{bmatrix}, & B_{KF} &= \begin{bmatrix} 0 \\ 1 \end{bmatrix}, \\ C_{KF} &= \begin{bmatrix} \frac{\kappa_3}{\kappa_4 c^2} - \frac{\kappa_1}{\kappa_4^2 c^2} & \frac{\kappa_2}{\kappa_4 c} - \frac{\kappa_1 \kappa_5}{\kappa_4^2 c} \end{bmatrix}, & D_{KF} &= \frac{\kappa_1}{\kappa_4}. \end{aligned}$$

Finally, all of the above equations are combined to obtain the following wind model, denoted by F:

$$\begin{bmatrix} \dot{x}_F(t) \\ v_t(t) \end{bmatrix} = \begin{bmatrix} A_F & B_F(t) \\ C_F & D_F(t) \end{bmatrix} \begin{bmatrix} x_F(t) \\ w_w(t) \end{bmatrix}, \tag{3.3}$$

with

$$\begin{aligned} A_F &= \begin{bmatrix} A_{HF} & \mathbf{0}_{4\times 2} \\ B_{KF}C_{HF} & A_{KF} \end{bmatrix}, & B_F(t) &= \begin{bmatrix} B_{HF}(t) \\ B_{KF}D_{HF}(t) \end{bmatrix}, \\ C_F &= \begin{bmatrix} K_F D_{KF} C_{HF} & K_F C_{KF} \end{bmatrix}, & D_F(t) &= K_F D_{KF} D_{HF}(t), \end{aligned} \tag{3.4}$$

where $x_F(t) = \begin{bmatrix} x_{HF}(t)^T & x_{KF}(t)^T \end{bmatrix}^T \in \mathbb{R}^{n_F}$ is the vector of state variables of the wind model, $w_w(t) \in \mathbb{R}^{n_s}$ the vector of exogenous inputs which in this model are white noise signals, and $v_t(t) \in \mathbb{R}$ is the turbulent wind speed (output of the wind model). Sample wind profiles generated using this wind model are shown in Figure 3.5 at four different mean wind speeds $v_m = \{16, 18, 20, 23\}\ m/s$.

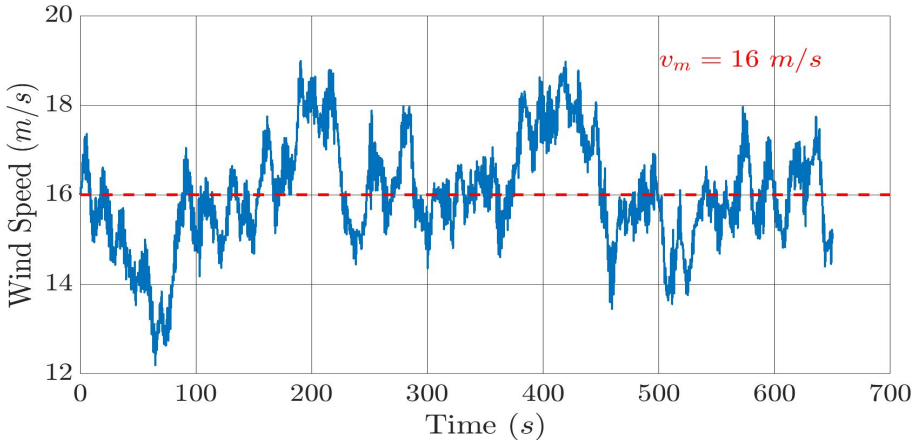

(a) $v_m = 16\ m/s$

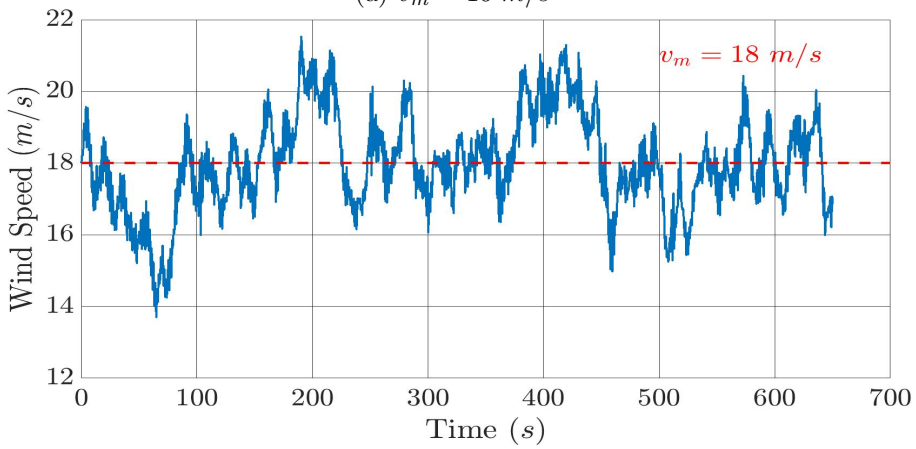

(b) $v_m = 18\ m/s$

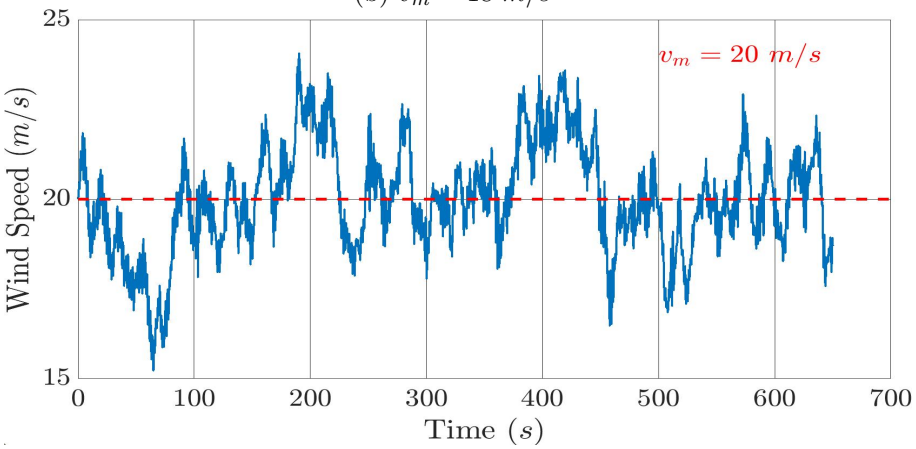

(c) $v_m = 20\ m/s$

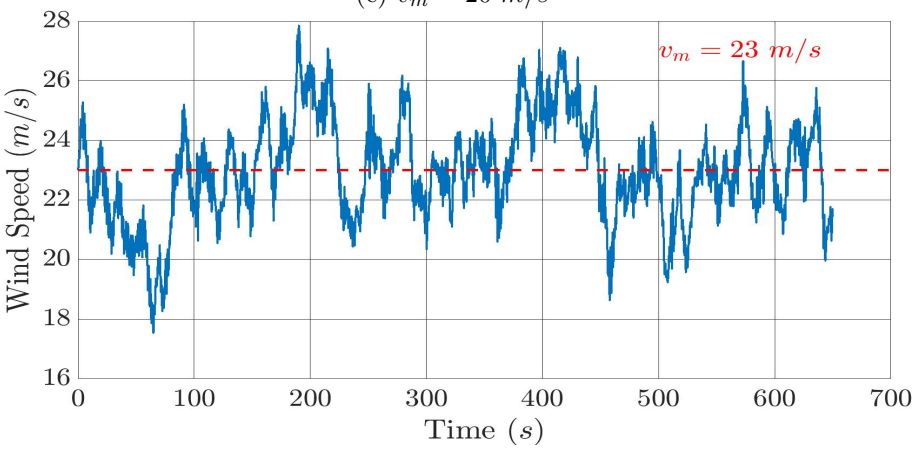

(d) $v_m = 23\ m/s$

Figure 3.5: Sample wind profiles generated at four different mean wind speeds using the wind model given in Figure 3.4.

Chapter 4

PROPOSED FRAMEWORK AND SIMULATION RESULTS

4.1 Wind Turbine Model Linearization and Control Synthesis

Open-loop Wind Turbine Model: In this thesis, 10 DOFs of the wind turbine model provided by OpenFAST are considered. The chosen DOFs cover the different components of the wind turbine, i.e., blades, tower, drive train, and generator, and are the first flap-wise and edge-wise bending modes of the three blades, the first fore-aft and side-to-side tower bending modes, the drive train rotational flexibility, and the generator DOF. Enabling only a subset of the available DOFs is a common practice in the literature [22]–[25] to reduce the computational complexity of the controller synthesis problem. Multiple linearized time-invariant models of the nonlinear wind turbine model are obtained as described in Section 3.3.2. Four different operating mean wind speeds in Region 3 of the wind turbine operation are chosen for the linearization. These wind speeds are $\bar{u}_d^{WT} = 16\ m/s$, $\bar{u}_d^{WT} = 18\ m/s$, $\bar{u}_d^{WT} = 20\ m/s$, and $\bar{u}_d^{WT} = 23\ m/s$.

Each obtained wind turbine linear model comprises 20 state variables. However, it is common practice to remove the generator azimuth state from the wind turbine LTI model, as it is solely an integrator state that has no effect on the dynamics of the LTI model after azimuth-averaging [25]. In the model used in this thesis, the wind disturbance is generated using the input hub-height wind speed $v_h = v_m + v_t$, where $v_m = \bar{u}_d^{WT}$ is the mean wind speed and v_t is the turbulent wind speed. The only measured output of the model is rotor speed, which is used as the feedback input to the controller. Thus, the wind turbine linear model is given by the open-loop system of the form

$$\begin{bmatrix} \dot{x}_{OL}(t) \\ e(t) \\ y(t) \end{bmatrix} = \begin{bmatrix} A & B_1 & B_2 \\ C_1 & D_{11} & D_{12} \\ C_2 & D_{21} & D_{22} \end{bmatrix} \begin{bmatrix} x_{OL}(t) \\ u_d(t) \\ u_c(t) \end{bmatrix},$$

where $x_{OL}(t) = \Delta x^{WT}(t) \in \mathbb{R}^{n_G}$, $u_d(t) = \Delta u_d^{WT}(t) = v_t \in \mathbb{R}^{n_d}$ is the turbulent wind speed, $u_c(t) = \Delta u_c^{WT}(t) \in \mathbb{R}^{n_c}$, $e(t) = \Delta y^{WT}(t) \in \mathbb{R}^{n_e}$, and $y(t) \in \mathbb{R}$ is the rotor

speed. Moreover, $n_G = 19$, $n_d = 1$, and $n_c = 1$.

Control Synthesis: In this thesis, collective blade pitch controllers are designed for Region 3 of the wind turbine operation. Therefore, the generator torque is held constant at its rated value. The control objective in this region is to maintain the generated power of the wind turbine near its rated value. This is achieved through designing controllers that regulate the turbine's rotor/generator speed near its rated value. Therefore, rotor speed error $\Delta\omega_r(t)$, i.e., the deviation of rotor speed from its reference value at the operating point used in the linearization, is the penalized performance output used for control synthesis. The wind turbine model linearized at $v_m = 18\ m/s$ is used for the control synthesis. $\mathcal{H}_\infty$ and PI controllers are synthesized as described in Sections 2.2 and 2.3, respectively. In addition to the rotor speed, the control input signal is also penalized. For the $\mathcal{H}_\infty$ controller, frequency weights on the performance outputs are used, namely,

$$e = \begin{bmatrix} W_e & 0 \\ 0 & W_u \end{bmatrix} \begin{bmatrix} \Delta\omega_r \\ u_c \end{bmatrix},$$

where the weights

$$W_e(s) = \frac{0.25s + 0.4648}{s + 0.4226},\ W_u(s) = \frac{500s + 882.1}{s + 220.5},$$

are inspired from [25] and are tuned to ensure satisfactory performance of the controller. The performance weight $W_e(s)$ for the rotor speed tracking error is chosen to penalize the low frequency tracking error, while the performance weight $W_u(s)$ on the pitch controller input is chosen to penalize the high frequency control effort. The resulting $\mathcal{H}_\infty$ controller has 21 state variables. For the PI controller, the performance outputs chosen are $e(t) = \begin{bmatrix} \Delta\omega_r(t) & u_c(t) \end{bmatrix}^T$. The $\mathcal{H}_\infty$ controller is obtained by solving one semidefinite program, namely, the SDP given in (P_1), one time for optimality and one time for feasibility after relaxing γ. The PI controller is obtained using the iterative procedure, whereby two SDPs are solved at each iteration. The SDPs in this thesis are modeled using YALMIP [48] and solved using MOSEK [49]. The designed controllers are then connected to the wind turbine model featuring pitch actuator dynamics given in Section 3.4. For the $\mathcal{H}_\infty$ controller, the resulting closed-loop system has 42 state variables and has the form given in equation (2.3). For the PI controller, the resulting closed-loop system has 22 state variables and has the form given in equation (2.10). A sample simulation of the designed controllers is shown in Figure 4.1 corresponding to a mean wind speed $v_m = 18\ m/s$. Both controllers have a satisfactory performance in terms of rated rotor speed, i.e., power tracking and load reduction on the wind turbine blades and tower. It can be seen that the $\mathcal{H}_\infty$ controller yields better tracking that the PI controller. However, the loads experienced by the wind turbine are almost the same for both controllers. Moreover, the pitch angle, i.e., the control effort, is very similar for both controllers. The performance of the controllers will be quantified in the analysis and simulations results of this section, and thus, a more clear comparison of the controllers will be observed. Sample simulations performed with turbulent wind profiles, generated using

the wind model described in Section 3.5 for the mean wind speeds $v_m = \{16, 20, 23\}$ m/s, are presented in Figures A.4, A.5, and A.6 in Appendix A, respectively.

4.2 Proposed Framework

The aim of this thesis is to perform robustness analysis of wind turbine control systems by incorporating wind turbulence characteristics into the analysis, which allows for analysis that more accurately reflects the wind turbine's performance and operating conditions. Thus, the system to be analyzed consists of a wind model connected to the wind turbine LTI model. For this purpose, the wind model presented in Section 3.5 is considered. The wind model given in (3.3) is of the form

$$\begin{bmatrix} \dot{x}_F(t) \\ u_d(t) \end{bmatrix} = \begin{bmatrix} A_F & B_F\big(\delta(t)\big) \\ C_F & D_F\big(\delta(t)\big) \end{bmatrix} \begin{bmatrix} x_F(t) \\ w_w(t) \end{bmatrix},$$

where $\delta(t) = \begin{bmatrix}\delta_1(t) & \delta_2(t)\end{bmatrix}^T$ with $\delta_1(t) = \mathbf{cos}(3\omega_r t)$ and $\delta_2(t) = \mathbf{sin}(3\omega_r t)$. Herein, the wind model will be treated as a linear parameter-varying system, where δ_1 and δ_2 are scalar time-varying parameters with $-1 \leq \delta_1, \delta_2 \leq 1$. Figure 4.2a depicts the representation of the wind model as an uncertain system. To represent the wind model in the Linear Fraction Transformation (LFT) framework, the input and feedthrough matrices B_F and D_F given in (3.4) containing the time-varying terms δ_1 and δ_2 can be expressed as

$$\begin{aligned}
B_F(\delta) &= \begin{bmatrix} B_{HF} \\ B_{KF}D_{HF} \end{bmatrix} = \begin{bmatrix} B_{HF_1} & \mathbf{0} & \mathbf{0} \\ \mathbf{0} & \sqrt{2}\delta_1 B_{HF_2} & \sqrt{2}\delta_2 B_{HF_2} \\ B_{KF}D_{HF_1} & \sqrt{2}\delta_1 B_{KF}D_{HF_2} & \sqrt{2}\delta_2 B_{KF}D_{HF_2} \end{bmatrix} \\
&= \begin{bmatrix} B_{HF_1} & \mathbf{0} & \mathbf{0} \\ \mathbf{0} & \mathbf{0} & \mathbf{0} \\ B_{KF}D_{HF_1} & \mathbf{0} & \mathbf{0} \end{bmatrix} \\
&\qquad + \begin{bmatrix} \mathbf{0} & \mathbf{0} \\ \sqrt{2}B_{HF_2} & \sqrt{2}B_{HF_2} \\ \sqrt{2}B_{KF}D_{HF_2} & \sqrt{2}B_{KF}D_{HF_2} \end{bmatrix} \begin{bmatrix} \delta_1 & 0 \\ 0 & \delta_2 \end{bmatrix} \begin{bmatrix} 0 & 1 & 0 \\ 0 & 0 & 1 \end{bmatrix}, \\
D_F(\delta) &= K_F D_{KF} D_{HF} = \begin{bmatrix} K_F D_{KF} D_{HF_1} & \sqrt{2}\delta_1 K_F D_{KF} D_{HF_2} & \sqrt{2}\delta_2 K_F D_{KF} D_{HF_2} \end{bmatrix} \\
&= \begin{bmatrix} K_F D_{KF} D_{HF_1} & 0 & 0 \end{bmatrix} \\
&\qquad + \begin{bmatrix} \sqrt{2}K_F D_{KF} D_{HF_2} & \sqrt{2}K_F D_{KF} D_{HF_2} \end{bmatrix} \begin{bmatrix} \delta_1 & 0 \\ 0 & \delta_2 \end{bmatrix} \begin{bmatrix} 0 & 1 & 0 \\ 0 & 0 & 1 \end{bmatrix}.
\end{aligned}$$

As a result, the wind model can be alternatively represented as

$$\begin{bmatrix} \dot{x}_F(t) \\ u_d(t) \end{bmatrix} = \begin{bmatrix} A^\Delta & B^\Delta \\ C^\Delta & D^\Delta \end{bmatrix} \begin{bmatrix} x_F(t) \\ w_w(t) \end{bmatrix}, \tag{4.1}$$

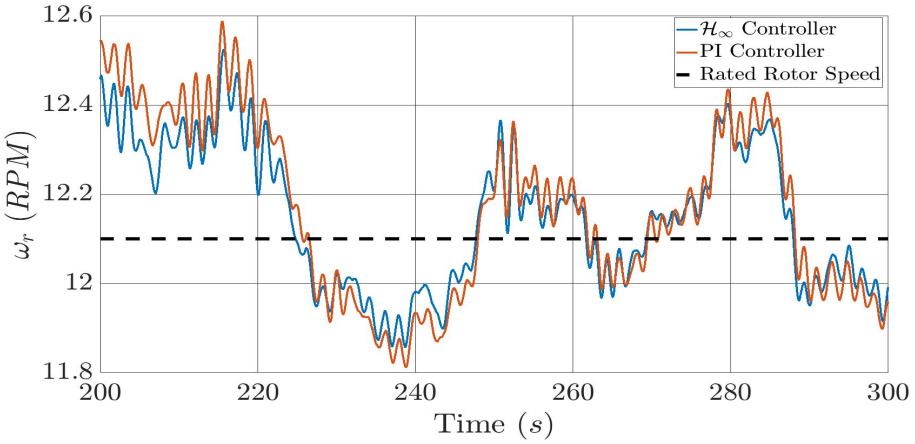

(a) Rotor speed

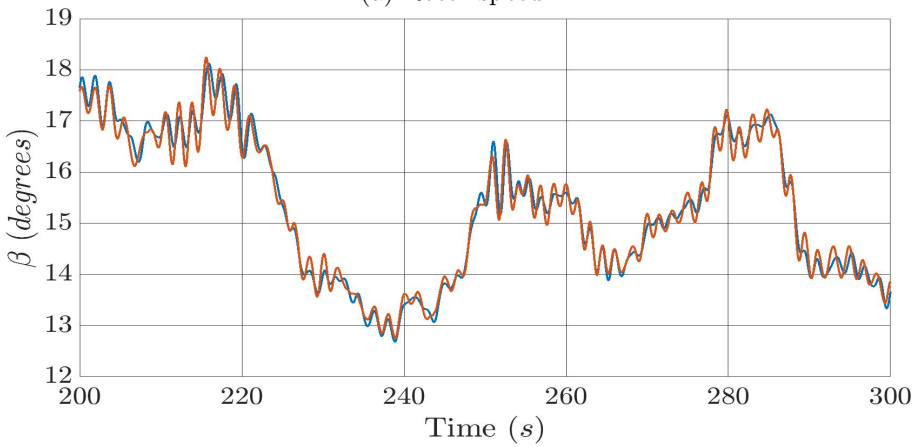

(b) Blade pitch angle

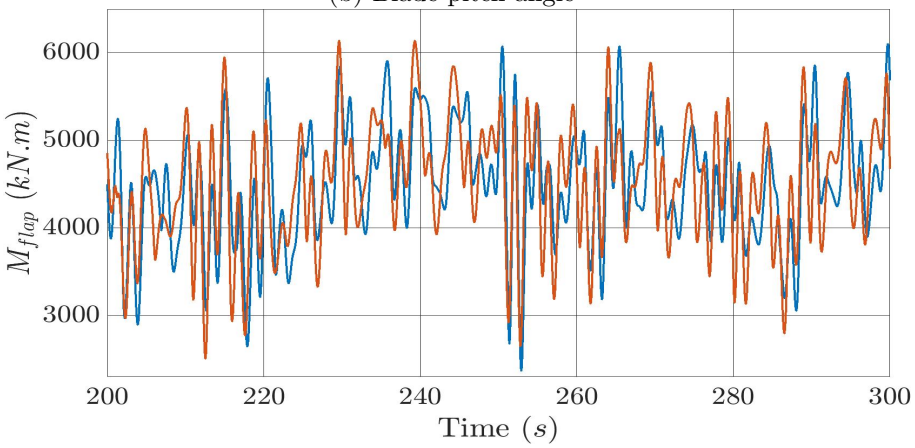

(c) Blade 1 flap-wise bending moment

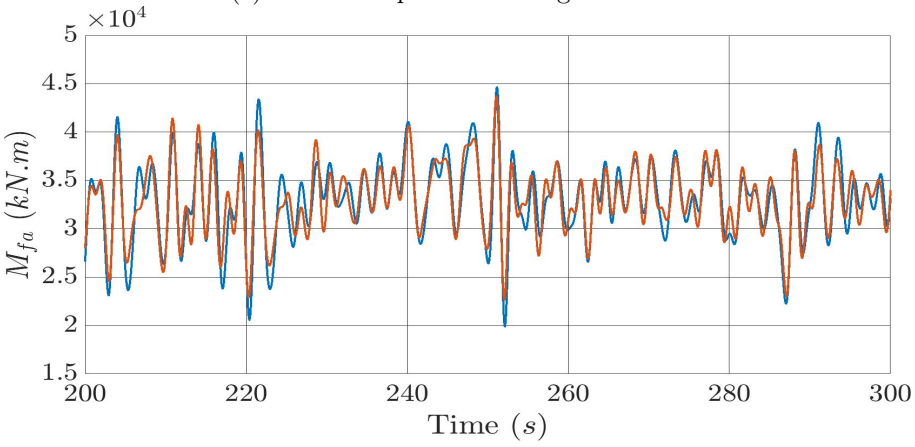

(d) Tower fore-aft bending moment

Figure 4.1: Sample simulation results for the $\mathcal{H}_\infty$ and PI controllers at $v_m = 18\ m/s$.

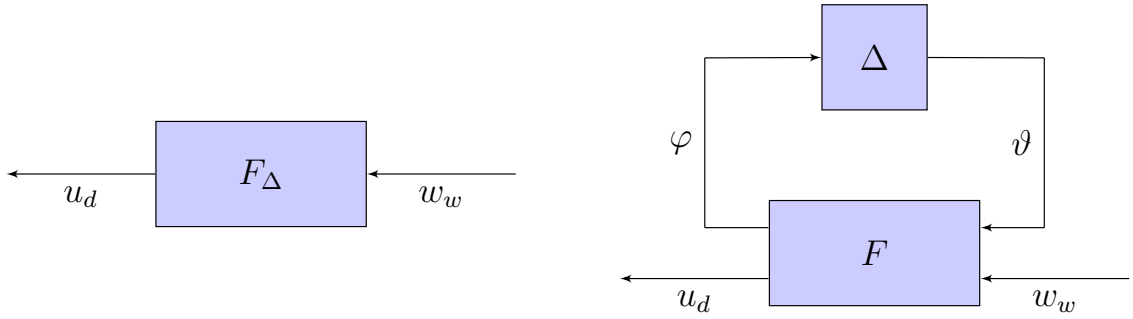

(a) Uncertain wind model.

(b) LFT representation of the uncertain wind model.

Figure 4.2: Uncertain wind model in the LFT framework.

with

$$\begin{bmatrix} A_\Delta & B_\Delta \\ C_\Delta & D_\Delta \end{bmatrix} = \begin{bmatrix} A^F + B_1^F\Delta\big(I - D_{11}^F\Delta\big)^{-1}C_1^F & B_1^F\Delta\big(I - D_{11}^F\Delta\big)^{-1}D_{12}^F + B_2^F \\ C_2^F + D_{21}^F\Delta\big(I - D_{11}^F\Delta\big)^{-1}C_1^F & D_{21}^F\Delta\big(I - D_{11}^F\Delta\big)^{-1}D_{12}^F + D_{22}^F \end{bmatrix}$$
$$= \begin{bmatrix} A^F & B_2^F \\ C_2^F & D_{22}^F \end{bmatrix} + \begin{bmatrix} B_1^F \\ D_{21}^F \end{bmatrix} \Delta(I - D_{11}^F\Delta)^{-1} \begin{bmatrix} C_1^F & D_{12}^F \end{bmatrix},$$

where

$$\Delta = \begin{bmatrix} \delta_1 & 0 \\ 0 & \delta_2 \end{bmatrix}, \tag{4.2}$$

$$A^F{=}A_F \quad B_1^F{=}\begin{bmatrix} \mathbf{0} & \mathbf{0} \\ \sqrt{2}B_{HF_2} & \sqrt{2}B_{HF_2} \\ \sqrt{2}B_{KF}D_{HF_2} & \sqrt{2}B_{KF}D_{HF_2} \end{bmatrix}, \quad B_2^F{=}\begin{bmatrix} B_{HF_1} & \mathbf{0} & \mathbf{0} \\ \mathbf{0} & \mathbf{0} & \mathbf{0} \\ B_{KF}D_{HF_1} & \mathbf{0} & \mathbf{0} \end{bmatrix},$$
$$C_1^F{=}\mathbf{0} \quad D_{11}^F{=}\mathbf{0} \quad D_{12}^F{=}\begin{bmatrix} 0 & 1 & 0 \\ 0 & 0 & 1 \end{bmatrix}, \tag{4.3}$$
$$C_2^F{=}C_F \quad D_{21}^F{=}\begin{bmatrix}\sqrt{2}KD_{KF}D_{HF_2} & \sqrt{2}KD_{KF}D_{HF_2}\end{bmatrix}, \quad D_{22}^F{=}\begin{bmatrix}KD_{KF}D_{HF_1} & 0 & 0\end{bmatrix}.$$

As shown in Figure 4.2b, the wind model can be represented in the LFT framework as a feedback interconnection of the linear time-invariant nominal wind model F and the uncertainty block Δ defined in (4.2). This model is described by

$$\begin{bmatrix} \dot{x}_F(t) \\ \varphi(t) \\ u_d(t) \end{bmatrix} = \begin{bmatrix} A^F & B_1^F & B_2^F \\ C_1^F & D_{11}^F & D_{12}^F \\ C_2^F & D_{21}^F & D_{22}^F \end{bmatrix} \begin{bmatrix} x_F(t) \\ \vartheta(t) \\ w_w(t) \end{bmatrix}, \ \vartheta(t) = \Delta(t)\varphi(t). \tag{4.4}$$

In the proposed framework, the wind model is combined with the wind turbine linearized time-invariant model. The resulting model $\mathcal{H}$ is depicted in Figures 4.3a and 4.3b and is described by the following equations:

$$\begin{bmatrix} \dot{x}_\mathcal{H}(t) \\ \varphi(t) \\ e(t) \end{bmatrix} = \begin{bmatrix} A^\mathcal{H} & B_1^\mathcal{H} & B_2^\mathcal{H} \\ C_1^\mathcal{H} & D_{11}^\mathcal{H} & D_{12}^\mathcal{H} \\ C_2^\mathcal{H} & D_{21}^\mathcal{H} & D_{22}^\mathcal{H} \end{bmatrix} \begin{bmatrix} x_\mathcal{H}(t) \\ \vartheta(t) \\ w_w(t) \end{bmatrix}, \ \vartheta(t) = \Delta(t)\varphi(t),$$

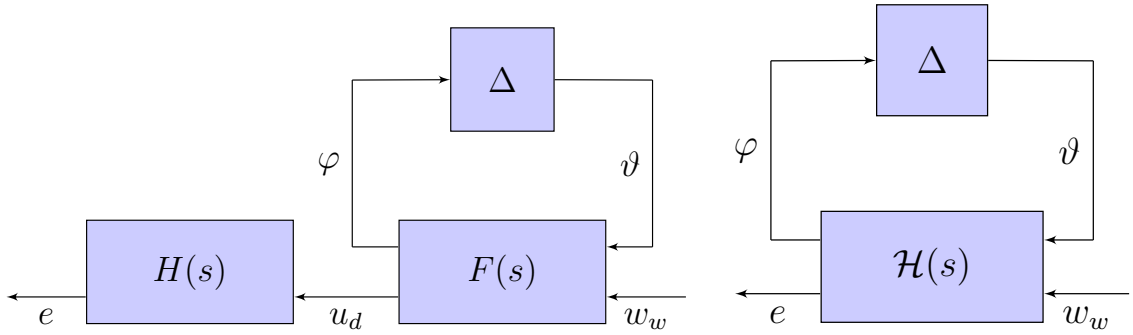

(a) Uncertain wind model connected to the wind turbine model.

(b) Resulting uncertain wind turbine model.

Figure 4.3: Block diagram representation of the wind turbine model.

with

$$A^{\mathcal{H}} = \begin{bmatrix} A_{CL} & B_{CL}C_2^F \\ \mathbf{0} & A^F \end{bmatrix}, \quad B_1^{\mathcal{H}} = \begin{bmatrix} B_{CL}D_{21}^F \\ B_1^F \end{bmatrix}, \quad B_2^{\mathcal{H}} = \begin{bmatrix} B_{CL}D_{22}^F \\ B_2^F \end{bmatrix},$$
$$C_1^{\mathcal{H}} = \begin{bmatrix} \mathbf{0} & C_1^F \end{bmatrix}, \quad D_{11}^{\mathcal{H}} = D_{11}^F, \quad D_{12}^{\mathcal{H}} = D_{12}^F,$$
$$C_2^{\mathcal{H}} = \begin{bmatrix} C_{CL} & D_{CL}C_2^F \end{bmatrix}, \quad D_{21}^{\mathcal{H}} = D_{CL}D_{21}^F, \quad D_{22}^{\mathcal{H}} = D_{CL}D_{22}^F,$$

where $x_{\mathcal{H}}(t) = \begin{bmatrix} x_{CL}(t)^T & x_F(t)^T \end{bmatrix}^T \in \mathbb{R}^{n+n_F}$ is the vector of state variables, $\left(A_{CL}, B_{CL}, C_{CL}, D_{CL}\right)$ are the state-space matrices of the closed-loop system H given in equations (2.4) and (2.11), and $\left(A^F, B_1^F, B_2^F, C_1^F, D_{11}^F, D_{12}^F, C_2^F, D_{21}^F, D_{22}^F\right)$ are the state-space matrices of the wind model given in (4.3).

The uncertainties δ_i with $i = \{1, 2\}$ are modeled as static linear time-varying parameters whose characterization is given in Section 2.4. Defining the sets $\mathbf{\Delta}_i$ and $\mathbf{\Delta}$ as

$$\mathbf{\Delta}_i = \{\Delta_i : \vartheta_i(t) = \big(\Delta_i(\varphi_i(t))\big)(t) = \delta_i(t)\varphi_i(t) \text{ and } |\delta_i(t)| \leq 1\},$$
$$\mathbf{\Delta} = \{\Delta : \Delta = \begin{bmatrix} \Delta_1 & 0 \\ 0 & \Delta_2 \end{bmatrix}, \ \Delta_1 \in \mathbf{\Delta}_1 \text{ and } \Delta_2 \in \mathbf{\Delta}_2\},$$

then, $\mathbf{\Delta}$ is characterized by the IQC multiplier $\Pi = \psi^* \mathcal{S} \psi$, with

$$\psi = \begin{bmatrix} 1 & 0 & 0 & 0 \\ 0 & 0 & 1 & 0 \\ 0 & 1 & 0 & 0 \\ 0 & 0 & 0 & 1 \end{bmatrix}, \ \mathcal{S} = \begin{bmatrix} X_1 & 0 & 0 & 0 \\ 0 & -X_1 & 0 & 0 \\ 0 & 0 & X_2 & 0 \\ 0 & 0 & 0 & -X_2 \end{bmatrix}, \ X_1, X_2 \geq 0 (\in \mathbb{R}).$$

This is equivalent to passing $\varphi(t)$ and $\vartheta(t)$ through a filter ψ and imposing the time-domain constraint $\int_0^{+\infty} r(t)^T \mathcal{S} r(t) dt \geq 0$. The filter ψ is described by the equation

$$r(t) = D_{\psi_1}\varphi(t) + D_{\psi_2}\vartheta(t),$$

with

$$D_{\psi_1} = \begin{bmatrix} 1 & 0 \\ 0 & 0 \\ 0 & 1 \\ 0 & 0 \end{bmatrix}, \; D_{\psi_2} = \begin{bmatrix} 0 & 0 \\ 1 & 0 \\ 0 & 0 \\ 0 & 1 \end{bmatrix},$$

where $\vartheta(t) = \begin{bmatrix} \vartheta_1(t) & \vartheta_2(t) \end{bmatrix}^T$ and $\varphi(t) = \begin{bmatrix} \varphi_1(t) & \varphi_2(t) \end{bmatrix}^T$.

The white noise inputs of the wind turbine model w_{w_1}, w_{w_2}, and w_{w_3} are elements of the set of white signals $\mathcal{D}_w$, which has the signal IQC characterization described in Section 2.4. Therefore, three signal IQCs, with factorizations $\Phi_{w_i}(s) = \theta_i(s)^* \mathcal{R}_i \theta_i(s)$ given in equation (2.14), are needed to characterize the three input white noise signals. This is equivalent to passing w_{w_1}, w_{w_2}, and w_{w_3} through filters $\theta_1(s)$, $\theta_2(s)$, and $\theta_3(s)$, respectively, and imposing the time-domain constraint $\int_0^{+\infty} m_i(t)^T \mathcal{R}_i m_i(t) dt \geq 0$. For $i = \{1, 2, 3\}$, filter θ_i is described by the equations

$$\begin{bmatrix} \dot{x}_{\theta_i}(t) \\ m_i(t) \end{bmatrix} = \begin{bmatrix} A_{\theta_i} & B_{\theta_i} \\ C_{\theta_i} & D_{\theta_i} \end{bmatrix} \begin{bmatrix} x_{\theta_i}(t) \\ w_{w_i}(t) \end{bmatrix},$$

with

$$A_{\theta_i} = A_{Y_i}, \; B_{\theta_i} = B_{Y_i}, \; C_{\theta_i} = \begin{bmatrix} I_{N_i} \\ \mathbf{0}_{1 \times N_i} \end{bmatrix}, \; D_{\theta_i} = \begin{bmatrix} \mathbf{0}_{N_i \times 1} \\ 1 \end{bmatrix},$$

where $x_{\theta_i}(t) \in \mathbb{R}^{N_i}$ and $m_i(t) \in \mathbb{R}^{N_i+1}$ are the vectors of state variables and outputs of the filter θ_i, respectively. A_{Y_i} and B_{Y_i} are given in equation (2.14). Filters $\theta_1(s)$, $\theta_2(s)$, and $\theta_3(s)$ are then combined, and the resulting filter $\theta(s)$ has the form

$$\begin{bmatrix} \dot{x}_{\theta}(t) \\ m(t) \end{bmatrix} = \begin{bmatrix} A_{\theta} & B_{\theta} \\ C_{\theta} & D_{\theta} \end{bmatrix} \begin{bmatrix} x_{\theta}(t) \\ w_{w}(t) \end{bmatrix},$$

with

$$A_\theta = \mathbf{Blkdiag}\big(A_{\theta_1}, A_{\theta_2}, A_{\theta_3}\big), \qquad B_\theta = \mathbf{Blkdiag}\big(B_{\theta_1}, B_{\theta_2}, B_{\theta_3}\big),$$
$$C_\theta = \mathbf{Blkdiag}\big(C_{\theta_1}, C_{\theta_2}, C_{\theta_3}\big), \qquad D_\theta = \mathbf{Blkdiag}\big(D_{\theta_1}, D_{\theta_2}, D_{\theta_3}\big),$$

where $x_\theta(t) = \begin{bmatrix} x_{\theta_1}(t)^T & x_{\theta_2}(t)^T & x_{\theta_3}(t)^T \end{bmatrix}^T \in \mathbb{R}^N$ is the vector of state variables, $N = N_1 + N_2 + N_3$, and $m(t) = \begin{bmatrix} m_1(t)^T & m_2(t)^T & m_3(t)^T \end{bmatrix}^T \in \mathbb{R}^{N+n_s}$ is the vector of outputs of the resulting filter θ.

To obtain the state-space matrices $(\mathcal{A}, \mathcal{B}, \mathcal{C}, \mathcal{D})$ given in (2.13) and used to solve the SDP in (P_2), an augmented system is formed that combines the wind turbine model $\mathcal{H}$ and the IQC filters ψ and θ as shown in Figure 4.4. The equations of this augmented system are given by

$$\begin{bmatrix} \dot{x}(t) \\ r(t) \\ m(t) \\ e(t) \end{bmatrix} = \begin{bmatrix} \mathcal{A} & \mathcal{B}_1 & \mathcal{B}_2 \\ \mathcal{C}_1 & \mathcal{D}_{11} & \mathcal{D}_{12} \\ \mathcal{C}_2 & \mathcal{D}_{21} & \mathcal{D}_{22} \\ \mathcal{C}_3 & \mathcal{D}_{31} & \mathcal{D}_{32} \end{bmatrix} \begin{bmatrix} x_{\mathcal{H}}(t) \\ \vartheta(t) \\ w_w(t) \end{bmatrix},$$

with

$$\mathcal{A} = \begin{bmatrix} A^{\mathcal{H}} & \mathbf{0} \\ \mathbf{0} & A_\theta \end{bmatrix}, \qquad \mathcal{B}_1 = \begin{bmatrix} B_1^{\mathcal{H}} \\ \mathbf{0} \end{bmatrix}, \qquad \mathcal{B}_2 = \begin{bmatrix} B_2^{\mathcal{H}} \\ B_\theta \end{bmatrix},$$
$$\mathcal{C}_1 = \begin{bmatrix} D_{\psi_1} C_1^{\mathcal{H}} & \mathbf{0} \end{bmatrix}, \quad \mathcal{D}_{11} = D_{\psi_1} D_{11}^{\mathcal{H}} + D_{\psi_2}, \quad \mathcal{D}_{12} = D_{\psi_1} D_{12}^{\mathcal{H}},$$
$$\mathcal{C}_2 = \begin{bmatrix} \mathbf{0} & C_\theta \end{bmatrix}, \quad \mathcal{D}_{21} = \mathbf{0}, \quad \mathcal{D}_{22} = D_\theta,$$
$$\mathcal{C}_3 = \begin{bmatrix} C_2^{\mathcal{H}} & \mathbf{0} \end{bmatrix}, \quad \mathcal{D}_{31} = D_{21}^{\mathcal{H}}, \quad \mathcal{D}_{32} = D_{22}^{\mathcal{H}},$$

where $x(t) = \begin{bmatrix} x_{\mathcal{H}}(t)^T & x_\theta(t)^T \end{bmatrix}^T \in \mathbb{R}^{n+n_F+N}$ is the vector of state variables. Using the above notation, the SDP given in (P_2), solved for finding upper bounds on the $\mathcal{D}_w$-to-$\mathcal{L}_2$-induced norm of the system, can be equivalently written as

$$\begin{aligned}
\underset{\gamma^2, P, \mathcal{S}, \mathcal{R}}{\text{minimize}} \quad & \gamma^2 \\
\text{subject to} \quad & P = P^T, \\
& \begin{bmatrix} \mathcal{A}^T P + P\mathcal{A} & P\mathcal{B} \\ \mathcal{B}^T P & \mathbf{0} \end{bmatrix} + \begin{bmatrix} \mathcal{C}_1^T \\ \mathcal{D}_{11}^T \\ \mathcal{D}_{12}^T \end{bmatrix} S \begin{bmatrix} \mathcal{C}_1 & \mathcal{D}_{11} & \mathcal{D}_{12} \end{bmatrix} \\
& + \begin{bmatrix} \mathcal{C}_2^T \\ \mathcal{D}_{21}^T \\ \mathcal{D}_{22}^T \end{bmatrix} \mathcal{R} \begin{bmatrix} \mathcal{C}_2 & \mathcal{D}_{21} & \mathcal{D}_{22} \end{bmatrix} + \begin{bmatrix} \mathcal{C}_3^T \\ \mathcal{D}_{31}^T \\ \mathcal{D}_{32}^T \end{bmatrix} \begin{bmatrix} \mathcal{C}_3 & \mathcal{D}_{31} & \mathcal{D}_{32} \end{bmatrix} \\
& -\mathbf{Blkdiag}\big(\mathbf{0}, \gamma^2 I_{n_s}\big) \prec 0, \\
& X_1 \geq 0, \ X_2 \geq 0, \\
& b x_0^{s_1} + \textstyle\sum_{i=1}^N x_i^{s_1} \mathbf{tan}^{-1}\left(\frac{b}{a_i^{s_1}}\right) \geq 0, \\
& b x_0^{s_2} + \textstyle\sum_{i=1}^N x_i^{s_2} \mathbf{tan}^{-1}\left(\frac{b}{a_i^{s_2}}\right) \geq 0, \\
& b x_0^{s_3} + \textstyle\sum_{i=1}^N x_i^{s_3} \mathbf{tan}^{-1}\left(\frac{b}{a_i^{s_3}}\right) \geq 0,
\end{aligned} \tag{P_3}$$

where $\mathcal{B} = \begin{bmatrix} \mathcal{B}_1 & \mathcal{B}_2 \end{bmatrix}$, and the subscripts s_i for $i = \{1, 2, 3\}$ correspond to the three signal IQCs.

4.3 Analysis

Robustness analysis of wind turbine control systems is performed. The analysis framework is utilized to test the designed controllers in terms of rated power tracking and load reduction on the wind turbine components. Moreover, the analysis framework is employed to compare the designed controllers and test their robustness across varying wind speeds. Three outputs are considered when assessing the controllers: (the errors in) rotor speed, blade flap-wise bending moment, and tower fore-aft bending moment.

In this thesis, two types of analyses are performed. First, traditional KYP analysis is performed, wherein the wind turbine closed-loop LTI model is considered. In this case, the performance metric used is the $\mathcal{L}_2$-induced norm of the mapping from the turbulent wind speed input u_d to the output e. Then, analysis of the augmented system in the proposed framework is done. In this case, the performance metric

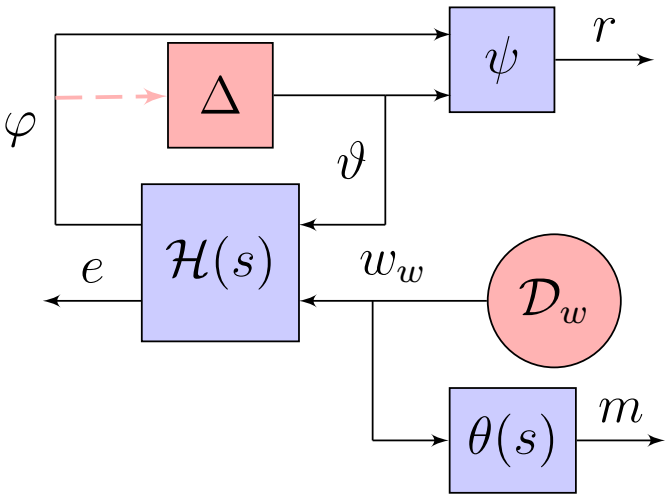

Figure 4.4: Uncertain wind turbine model and IQC filters. The red blocks are eliminated as they are replaced by the IQC characterizations given by the filters ψ and θ and the constraints on their outputs.

used is the $\mathcal{D}_w$-to-$\mathcal{L}_2$-induced norm of the mapping from the white noise inputs w_w to the performance output e. These two mappings can be observed in Figure 4.3a. Hereafter, the two types of analyses will be referred to as traditional analysis and IQC analysis, for simplicity and ease of reference.

Three different values of the induced norm corresponding to three different outputs are considered. These outputs are the rotor speed, the blade flap-wise bending moment, and the tower fore-aft bending moment. The frequency weights used in the control synthesis above are not considered here. However, the blade flap-wise bending moment and the tower fore-aft bending moment outputs are scaled by 10^{-3} and 10^{-5}, respectively, to ensure the convergence of the SDP solvers. The upper bounds on the induced norms of the system are computed at all four mean wind speeds $v_m = \{16, 18, 20, 23\}\ m/s$. This allows for investigating the robustness of the designed controllers across varying wind speeds. The obtained values of the $\mathcal{L}_2$-induced norms for the case of traditional analysis can be validated by using the MATLAB command `hinfnorm`. The analysis of both considered systems is repeated for all three outputs and both controllers by solving the SDP in (P_3). All problems were modeled using YALMIP [48] and solved using MOSEK [49].

The choice of the poles a_i of the signal IQC filters given in (2.14) is observed to have a major effect on the results of the proposed analysis framework as they affect the values of the upper bounds on the $\mathcal{D}_w$-to-$\mathcal{L}_2$-induced norms obtained using (P_3). However, this was not the case for the number of poles a_i for each filter θ_i. In fact, a negligible change in the results is observed when using more than three poles. Thus, a total of three poles were chosen for each filter in the performed analysis. For the purpose of this thesis, to choose the signal IQC filters, i.e., tune the poles a_i, that result in less conservative upper bounds, the following parameterization of the vector of poles a was chosen:

$$a = \big(x, x + 0.1, x + 0.2\big),\ x > 0.$$

This choice of parameterization is based on the observation that widely-spread poles resulted in more conservative upper bounds. Then, an optimal value of x is found, i.e., corresponding to poles that yield the smallest upper bounds for the given parameterization of a. Upon performing extensive tuning of/sweeping over x, the obtained optimal value of x was observed to be almost constant for a given output in both controllers and across different wind speeds. Hence, a constant value of x is considered for each output for the results presented in this thesis. The chosen pole vectors are $a = \begin{bmatrix}0.04 & 0.14 & 0.24\end{bmatrix}^T$, $a = \begin{bmatrix}0.08 & 0.18 & 0.28\end{bmatrix}^T$, and $a = \begin{bmatrix}1.2 & 1.3 & 1.4\end{bmatrix}^T$ corresponding to the outputs: rotor speed, blade flap-wise bending moment, and tower fore-aft bending moment, respectively. The same set of poles was used for all three signal IQC filters. Moreover, b is set to π as depicted in Figure 2.3. This choice is based on the fact that the band-limited white noise signals for continuous systems generated using Simulink have a flat power spectral density over the normalized frequency range of $[-\frac{1}{2}, \frac{1}{2}]$. For the simulations in this thesis, a sampling time of 1 s was chosen, or equivalently, a sampling frequency of 2π rad/s. Hence, the power spectrum is flat over the range $[-\pi, \pi]$, and therefore, $b = \pi$.

4.4 Simulations

Extensive simulations are performed to validate the results of the proposed analysis framework. Wind profiles were generated using the wind model given in Section 3.5 for the following values of mean wind speeds: $v_m = \{16, 18, 20, 23\}$ m/s. For the wind profiles corresponding to each mean wind speed, 3000 simulations were performed on the high-fidelity nonlinear wind turbine model provided by OpenFAST. The simulations were repeated for both $\mathcal{H}_\infty$ and PI control systems using the same wind profiles. Each simulation performed corresponds to 650 seconds of the wind turbine operation. For each simulation, the following approximate, experimental, value of the induced norm of interest is computed:

$$\gamma_{sim}^2 = \frac{\|e\|_{\mathcal{L}_2}^2}{\|u\|_{\mathcal{L}_2}^2} = \frac{\int_0^T e(t)^T e(t) dt}{\int_0^T u(t)^T u(t) dt},$$

where e is the output signal and u is the input signal, which can be the white noise signals w_w or the turbulent wind speed u_d. γ_{sim}^2 is computed for the three different outputs and two different inputs. It is noted that the first 50 seconds of the simulations are not considered when computing the experimental γ values. That is, the transient region of the nonlinear response in OpenFAST is eliminated, and the γ values are computed only in the steady-state region. While wind inputs are generally not finite energy signals, finite approximations are used here since a finite horizon operation of the wind turbine is considered in this thesis.

While obtaining the upper bounds using the SDP in (P_3) takes only a few seconds, computing the experimental γ values requires a lot of time. That is, for each of the two wind turbine control systems at the four different mean wind speed conditions, 3000 simulations were performed to validate the obtained upper bounds. For instance, each simulation is executed in approximately four minutes, and thus,

the 3000 simulations take up to 200 hours to be completed. On the other hand, the upper bounds, computed in a fraction of this time, cover all the values computed from simulations.

Experimental values of the induced norms are computed for each output, both controllers, and both white noise and turbulent wind speed inputs corresponding to IQC analysis and traditional analysis, respectively. Hereafter, all γ values are denoted by $\gamma_{i,j,k}$, where $i = \{rot, flap, fa\}$ corresponding to the rotor speed, the blade flap-wise bending moment, and the tower fore-aft bending moment outputs, respectively, $j = \{sys, wind\}$ corresponding to traditional analysis and IQC analysis, respectively, and $k = \{th, sim\}$ corresponding to the theoretical upper bounds obtained using the SDP in (P_3) and the experimental values from the simulations.

4.5 Results

The analysis and simulations results of this thesis are presented to highlight the importance of the proposed analysis framework. That is, the results are investigated to test the whether the proposed analysis framework is able to compare the performance of the two designed controllers, achieve valid upper bounds on experimental γ values obtained from simulations, and predict the performance of the designed controllers across varying wind speeds.

Controller Comparison: The experimental values of the induced norms obtained from the simulations for the two types of analyses, and both controllers are presented in histograms. In addition, the computed upper bounds are shown in the legend of each figure. In this section, the following histograms are included:

- Figure 4.5 corresponds to the rotor speed output for a mean wind speed of 18 m/s,
- Figure 4.6 corresponds to the blade flap-wise bending moment output for a mean wind speed of 18 m/s,
- Figure 4.7 corresponds to the tower fore-aft bending moment output for a mean wind speed of 18 m/s,
- Figure 4.8 corresponds to the rotor speed output for a mean wind speed of 16 m/s,
- Figure 4.9 corresponds to the blade flap-wise bending moment output for a mean wind speed of 23 m/s,

The rest of the results are included in Figures A.7-A.13 and can be found in Appendix A.

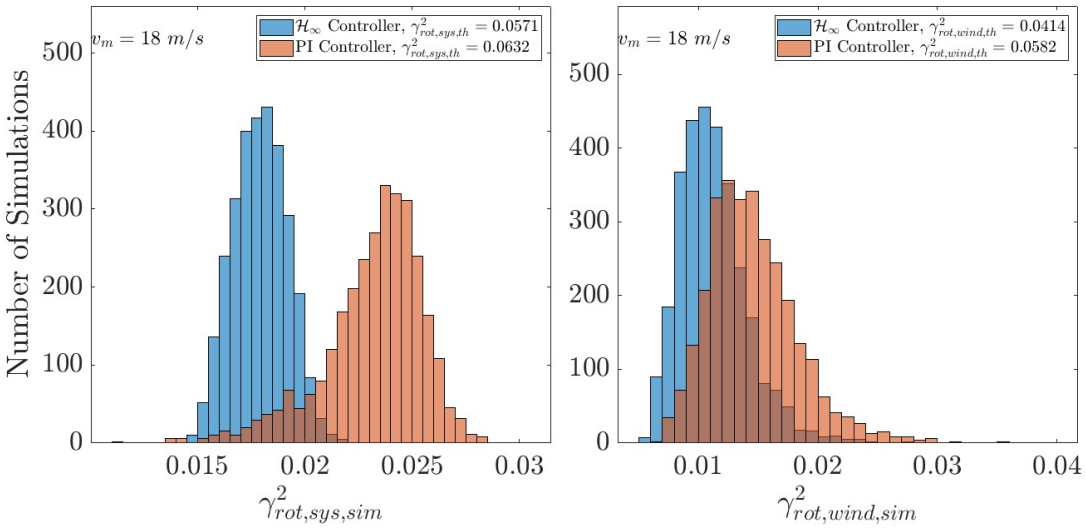

Figure 4.5: Results of the simulations performed at a mean wind speed of 18 m/s. The figure shows the square of the experimental γ values of the wind turbine control systems where the rotor speed is chosen as the performance output. The left figure corresponds to traditional analysis. The right figure corresponds to IQC analysis.

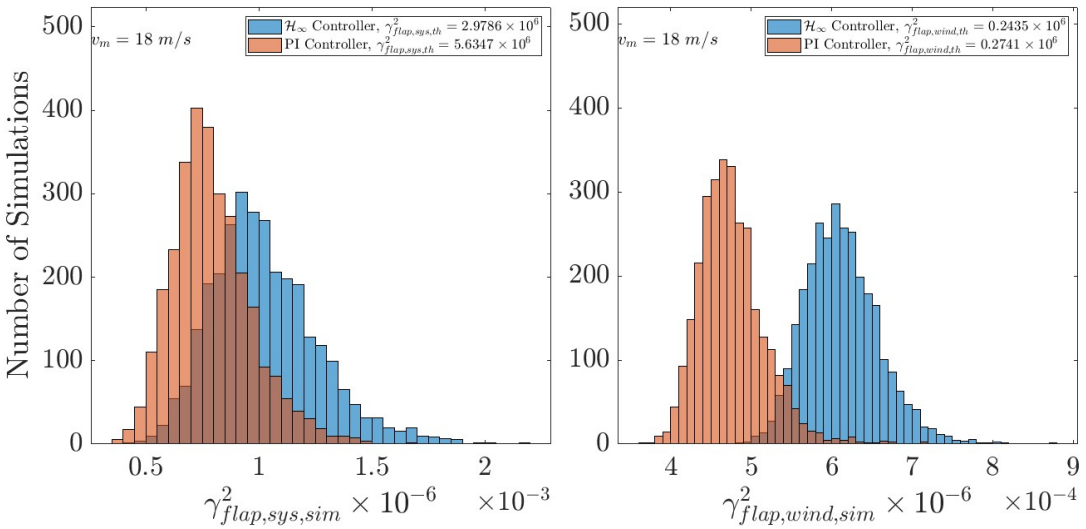

Figure 4.6: Results of the simulations performed at a mean wind speed of 18 m/s. The figure shows the square of the experimental γ values of the wind turbine control systems where the blade flap-wise bending moment is chosen as the performance output. The left figure corresponds to traditional analysis. The right figure corresponds to IQC analysis.

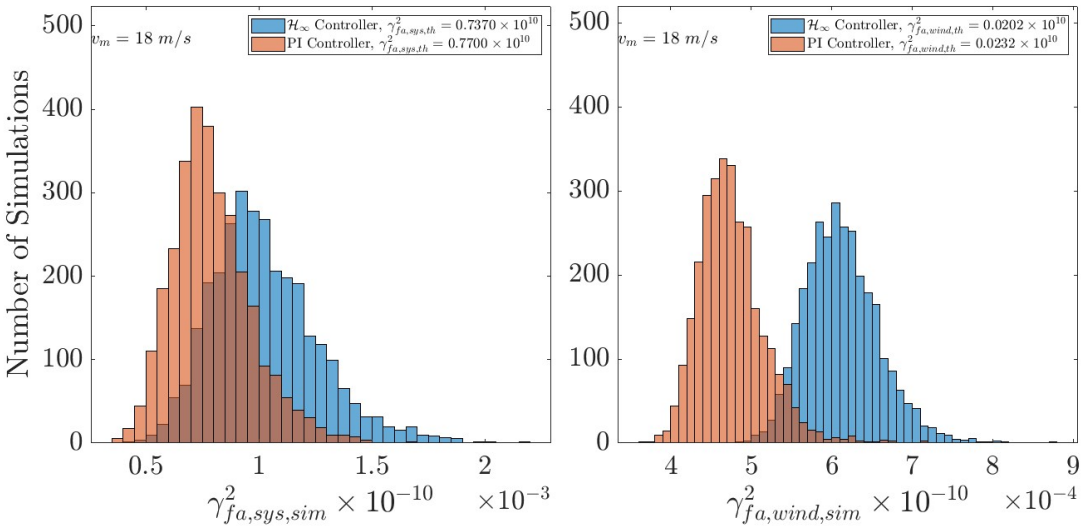

Figure 4.7: Results of the simulations performed at a mean wind speed of 18 m/s. The figure shows the square of the experimental γ values of the wind turbine control systems where the tower fore-aft bending moment is chosen as the performance output. The left figure corresponds to traditional analysis. The right figure corresponds to IQC analysis.

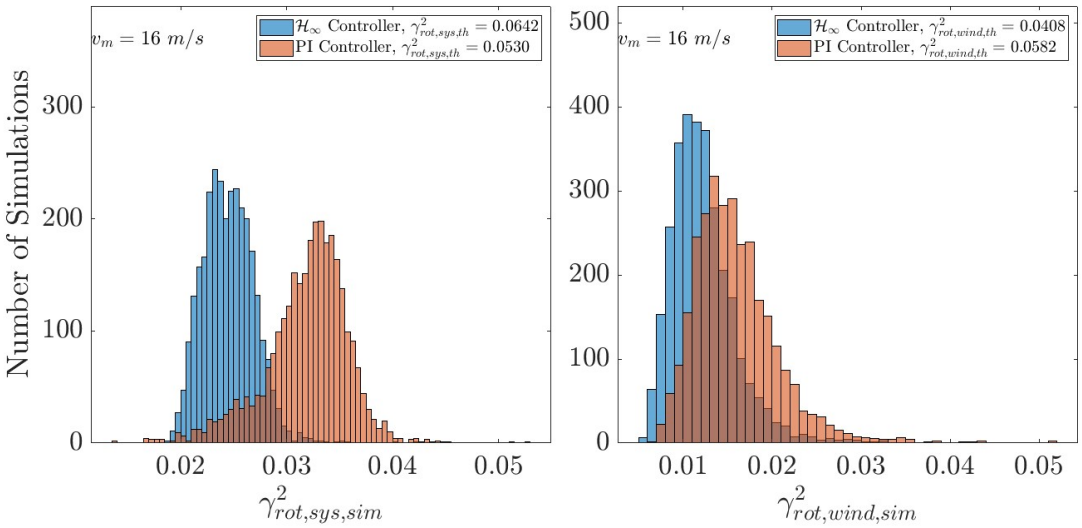

Figure 4.8: Results of the simulations performed at a mean wind speed of 16 m/s. The figure shows the square of the experimental γ values of the wind turbine control systems where the rotor speed is chosen as the performance output. The left figure corresponds to traditional analysis. The right figure corresponds to IQC analysis.

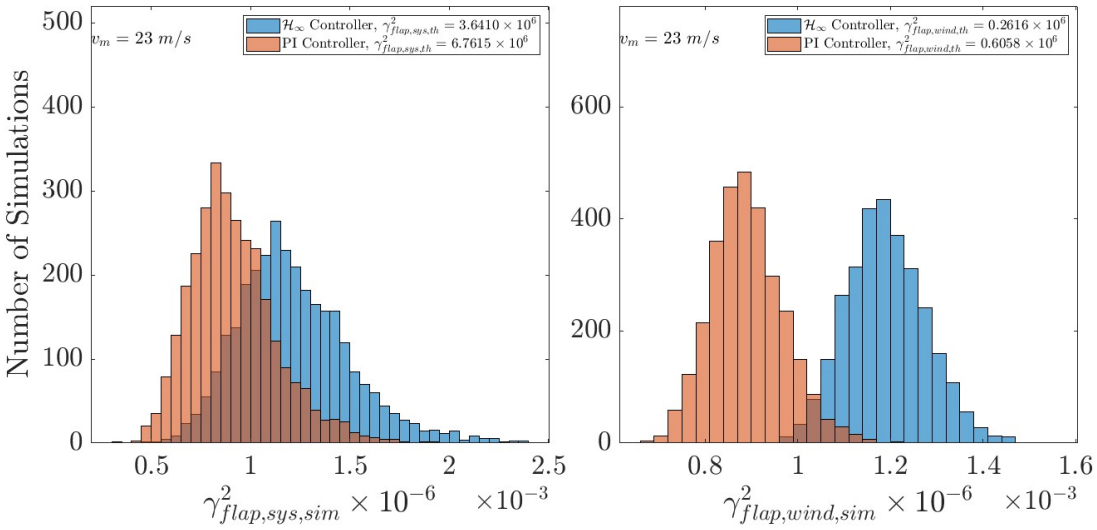

Figure 4.9: Results of the simulations performed at a mean wind speed of 23 m/s. The figure shows the square of the experimental γ values of the wind turbine control systems where the blade flap-wise bending moment is chosen as the performance output. The left figure corresponds to traditional analysis. The right figure corresponds to IQC analysis.

When comparing the two designed controllers for each of the three outputs at a specific wind speed, a controller is said to have a superior performance over the other controller if it has a smaller γ value. That is, from the analysis results, the controller having a smaller $\gamma^2_{i,j,th}$ value is said to be better. From the results of the simulations, the controller having smaller experimental γ values is said to be better. Since 3000 simulations are performed, the controller having γ values skewed to the left in Figures 4.5 - 4.9 is better. For the rotor speed output, it can be observed from Figures 4.5 and 4.8 that the $\mathcal{H}_\infty$ controller has a superior performance over the PI controller. For the blade flap-wise bending moment output, it can be observed from Figures 4.6 and 4.9 that the $\mathcal{H}_\infty$ and PI controllers exhibit very close performance. For the tower fore-aft bending moment output, it can be observed from Figure 4.7 that the PI controller has a superior performance over the $\mathcal{H}_\infty$ controller. One advantage of the proposed framework can be observed in Figure 4.8. The upper bounds on the $\mathcal{L}_2$-induced norms from the traditional analysis indicate a superior performance of the PI controller over the $\mathcal{H}_\infty$ controller for the mean wind speed of 16 m/s and the rotor speed performance output. However, the upper bounds on the $\mathcal{D}_w$-to-$\mathcal{L}_2$-induced norms from IQC analysis indicate the opposite. The results of the simulations are in line with those of IQC analysis. Therefore, a better characterization of the system's performance is achieved when using the proposed framework. Therefore, this framework is able to correctly predict the superior performance of a given controller over another, thus correctly matching the insights captured via extensive simulations. The limitations of the proposed framework in comparing wind turbine control systems are discussed in Section 4.6.

Validity of the Upper Bounds: Tables containing the values of the upper bounds on the induced norms, as well as the average and maximum values of the experimental γ^2 values obtained from simulations are presented next. In this section, the following tables are included:

- Table 4.1 corresponds to the rotor speed output for the case traditional analysis,
- Table 4.2 corresponds to the rotor speed output for the case of IQC analysis,
- Table 4.3 corresponds to the blade flap-wise bending moment output for the case of traditional analysis,
- Table 4.4 corresponds to the blade flap-wise bending moment output for the case of IQC analysis.

The rest of the results are included in Tables A.1-A.2 and can be found in Appendix A.

Table 4.1: $\mathcal{L}_2$-induced norms for the rotor speed output for the case of traditional analysis. $\bar{\gamma}^2_{\mathbf{rot,sys,sim}}$ and $\overset{\max}{\gamma^2}_{\mathbf{rot,sys,sim}}$ denote the squares of the average and maximum γ values obtained from the simulations, respectively.

Controller	$\mathbf{v_m}$	$\gamma^2_{\mathbf{rot,sys,th}}$	$\bar{\gamma}^2_{\mathbf{rot,sys,sim}}$	$\overset{\max}{\gamma^2}_{\mathbf{rot,sys,sim}}$
PI Controller	**16**	0.053	0.0318	0.0526
	18	0.0632	0.0231	0.0302
	20	0.0745	0.0189	0.0228
	23	0.079	0.0153	0.0178
$\mathcal{H}_\infty$ **Controller**	**16**	0.0642	0.0245	0.0421
	18	0.0571	0.0179	0.0231
	20	0.0509	0.0148	0.0174
	23	0.0541	0.0123	0.0143

Table 4.2: $\mathcal{D}_w$-to-$\mathcal{L}_2$-induced norms for the rotor speed output for the case of IQC analysis. $\bar{\gamma}^2_{\mathbf{rot,wind,sim}}$ and $\overset{\max}{\gamma^2}_{\mathbf{rot,wind,sim}}$ denote the squares of the average and maximum γ values obtained from the simulations, respectively.

Controller	$\mathbf{v_m}$	$\gamma^2_{\mathbf{rot,wind,th}}$	$\bar{\gamma}^2_{\mathbf{rot,wind,sim}}$	$\overset{\max}{\gamma^2}_{\mathbf{rot,wind,sim}}$
PI Controller	**16**	0.0582	0.0155	0.0514
	18	0.0582	0.0143	0.0398
	20	0.06	0.0145	0.0361
	23	0.0621	0.0155	0.0345
$\mathcal{H}_\infty$ **Controller**	**16**	0.0408	0.012	0.0421
	18	0.0414	0.0111	0.0317
	20	0.0434	0.0113	0.0286
	23	0.0465	0.0124	0.0276

Table 4.3: $\mathcal{L}_2$-induced norms for the blade flap-wise bending moment output for the case of traditional analysis. $\bar{\gamma}^2_{\mathbf{flap,sys,sim}}$ and $\overset{\max}{\gamma^2}_{\mathbf{flap,sys,sim}}$ denote the squares of the average and maximum γ values obtained from the simulations, respectively.

Controller	$\mathbf{v_m}$	$\gamma^2_{\mathbf{flap,sys,th}} \times \mathbf{10^{-6}}$	$\bar{\gamma}^2_{\mathbf{flap,sys,sim}} \times \mathbf{10^{-6}}$	$\overset{\max}{\gamma^2}_{\mathbf{flap,sys,sim}} \times 10^{-6}$
PI Controller	**16**	4.9772	0.2396	0.3711
	18	5.6347	0.1702	0.2692
	20	6.511	0.1467	0.2441
	23	6.7615	0.1433	0.2465
$\mathcal{H}_\infty$ **Controller**	**16**	3.0479	0.2455	0.375
	18	2.9786	0.1701	0.2704
	20	3.2259	0.1455	0.2433
	23	3.641	0.1448	0.2487

Table 4.4: $\mathcal{D}_w$-to-$\mathcal{L}_2$-induced norms for the blade flap-wise bending moment output for the case of IQC analysis. $\bar{\gamma}^2_{\mathbf{flap,wind,sim}}$ and $\overset{\max}{\gamma^2}_{\mathbf{flap,wind,sim}}$ denote the squares of the average and maximum γ values obtained from the simulations, respectively.

Controller	$\mathbf{v_m}$	$\gamma^2_{\mathbf{flap,wind,th}} \times \mathbf{10^{-6}}$	$\bar{\gamma}^2_{\mathbf{flap,wind,sim}} \times \mathbf{10^{-6}}$	$\overset{\max}{\gamma^2}_{\mathbf{flap,wind,sim}} \times 10^{-6}$
PI Controller	**16**	0.34	0.1163	0.3461
	18	0.2741	0.104	0.2149
	20	0.3649	0.1104	0.1704
	23	0.6058	0.1425	0.1758
$\mathcal{H}_\infty$ **Controller**	**16**	0.3047	0.119	0.3679
	18	0.2435	0.104	0.2114
	20	0.2294	0.1095	0.1688
	23	0.2616	0.144	0.1831

From the extensive simulations performed, it can be observed that the upper bounds computed using the proposed framework are validated and not violated. Specifically, for all the conducted simulations, the following observation can be made:

$$\gamma^2_{sim} < \gamma^2_{th},$$

for all three outputs and both analyzed systems. This can be clearly observed in Tables 4.1 - 4.4, which show the maximum γ value obtained from simulations and the theoretical upper bounds. Some violations of the upper bounds are discussed in Section 4.6.

Performance of a Given Controller across Varying Wind Speeds: Another advantage of the framework is that it allows for comparing a controller's performance across various wind speeds. This results from the fact that γ values in the proposed framework are normalized across wind speeds. Namely, the white noise inputs are identical at the different mean wind speeds, while turbulent wind speed inputs vary

vastly across wind speeds. For this reason, results from the analysis of the wind turbine model solely (traditional analysis) fail in predicting the performance trend of a controller across wind speeds. Plots showing a comparison of the upper bounds on the induced norms and the experimental γ values obtained from simulations at different mean wind speeds for the $\mathcal{H}_\infty$ control system are presented in Figure 4.10 for the rotor speed output, Figure 4.11 for the blade flap-wise bending moment output, and Figure 4.12 for the tower fore-aft bending moment output. Similar plots for the case of the PI controller are presented in Figures A.14 - A.16 in Appendix A.

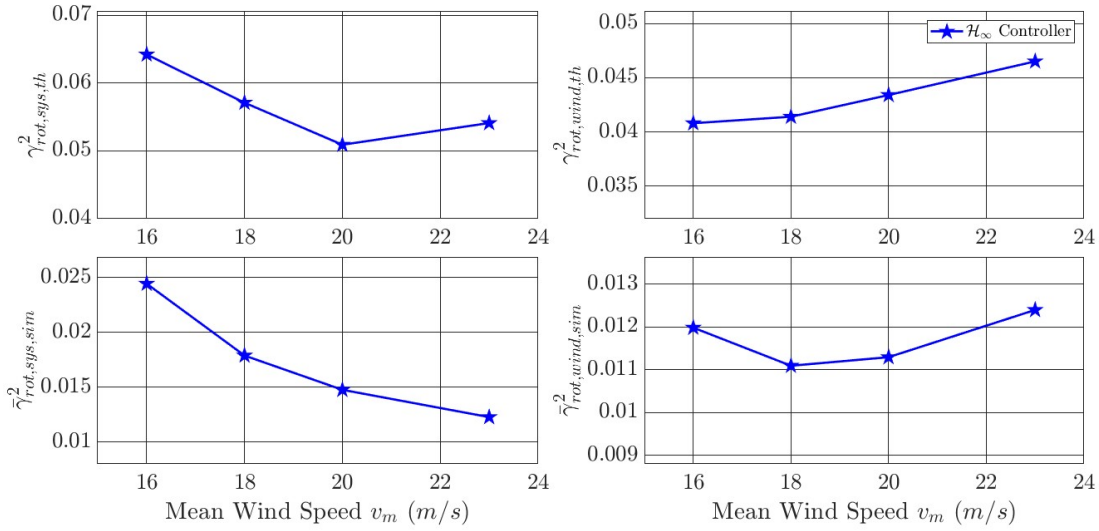

Figure 4.10: Results of the analysis and simulations performed at different mean wind speeds. The figure shows the square of the induced norms of the wind turbine system, for the case of the $\mathcal{H}_\infty$ controller, where the rotor speed is chosen as the performance output. The top left figure shows the upper bounds on the square of the $\mathcal{L}_2$-induced norm obtained from the traditional analysis. The top right figure shows the upper bounds on the square of the $\mathcal{D}_w$-to-$\mathcal{L}_2$-induced norms obtained from IQC analysis. The bottom left figure shows the square of the average of the experimental γ values obtained from the simulations for the case of turbulent wind input. The bottom right figure shows the square of the average of the experimental γ values obtained from the simulations for the case of white noise inputs.

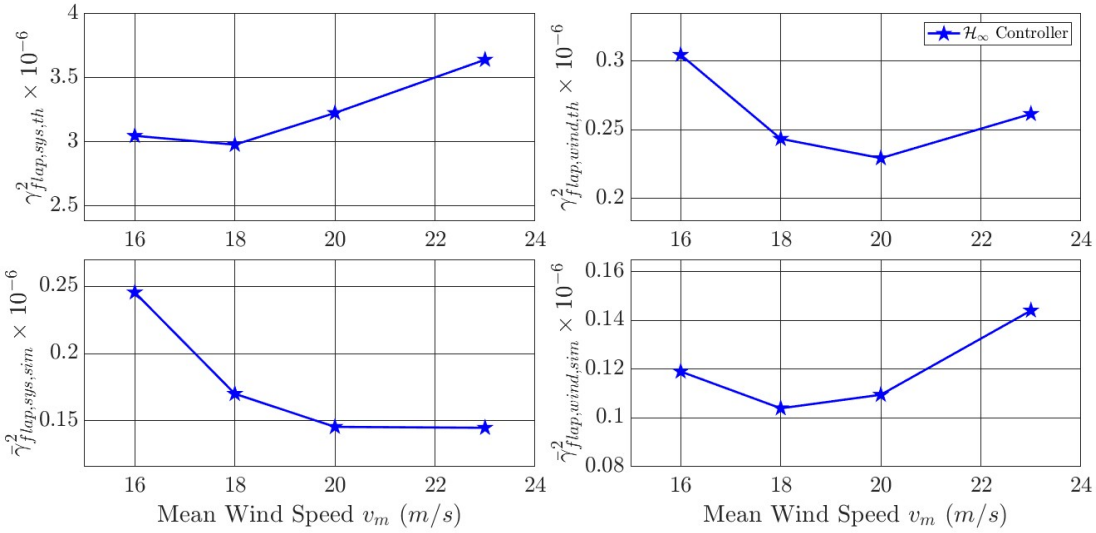

Figure 4.11: Results of the analysis and simulations performed at different mean wind speeds. The figure shows the square of the induced norms of the wind turbine system, for the case of the $\mathcal{H}_\infty$ controller, where the blade flap-wise bending moment is chosen as the performance output. The top left figure shows upper bounds on the square of the $\mathcal{L}_2$-induced norm obtained from traditional analysis. The top right figure shows upper bounds on the square of the $\mathcal{D}_w$-to-$\mathcal{L}_2$-induced norms obtained from IQC analysis. The bottom left figure shows the square of the average of the experimental γ values obtained from the simulations for the case of turbulent wind input. The bottom right figure shows the square of the average of the experimental γ values obtained from the simulations for the case of white noise inputs.

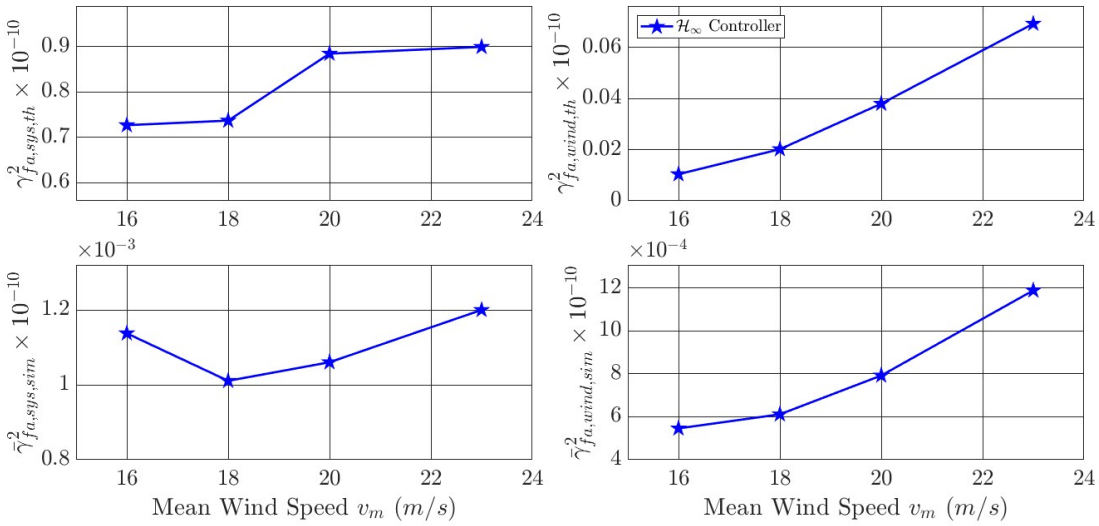

Figure 4.12: Results of the analysis and simulations performed at different mean wind speeds. The figure shows the square of the induced norms of the wind turbine system, for the case of the $\mathcal{H}_\infty$ controller, where the tower fore-aft bending moment is chosen as the performance output. The top left figure shows upper bounds on the square of the $\mathcal{L}_2$-induced norm obtained from traditional analysis. The top right figure shows upper bounds on the square of the $\mathcal{D}_w$-to-$\mathcal{L}_2$-induced norms obtained from IQC analysis. The bottom left figure shows the square of the average of the experimental γ values obtained from the simulations for the case of turbulent wind input. The bottom right figure shows the square of the average of the experimental γ values obtained from the simulations for the case of white noise inputs.

For a given controller across varying wind speeds, it can be observed that the trends are correctly predicted using the proposed framework. For instance, this can be observed for the tower fore-aft bending moment in Figure 4.12. The trend of variation of the experimental γ values obtained from the simulations across wind speeds for the case of white noise input signals, shown in the bottom right plot of Figure 4.12, matches that of the upper bounds on the $\mathcal{D}_w$-to-$\mathcal{L}_2$-induced norm from IQC analysis, shown in the top right plot of Figure 4.12. Thus, this framework is able to capture the trend of the controllers' performance over varying wind speeds while traditional analysis results fail, as shown in the top and bottom left plots of Figure 4.12. For other outputs, it seems that the trends are not exact. However, the difference is very small and can be due to the numerical precision of the solvers.

Upper Bounds on the $\mathcal{L}_2$-norms of the Outputs The computed upper bounds on the induced norms can be interpreted in a second way. That is, the computed γ values can be used to find upper bounds on the $\mathcal{L}_2$-norms of the outputs, i.e., $\|e\| \leq \gamma_{th}\|u\|$, for a given performance output e and corresponding input u. For this purpose, the $\mathcal{L}_2$-norms of the three different outputs obtained from the simulation of the $\mathcal{H}_\infty$ control system on the different mean wind speeds, as well as the upper bounds on the $\mathcal{L}_2$-norm of the outputs computed using the upper bounds

on the induced norms from traditional analysis and IQC analysis are presented in Figures 4.13 - 4.15. Similar plots for the case of the PI controller are presented in Figures A.17 - A.19 in Appendix A.

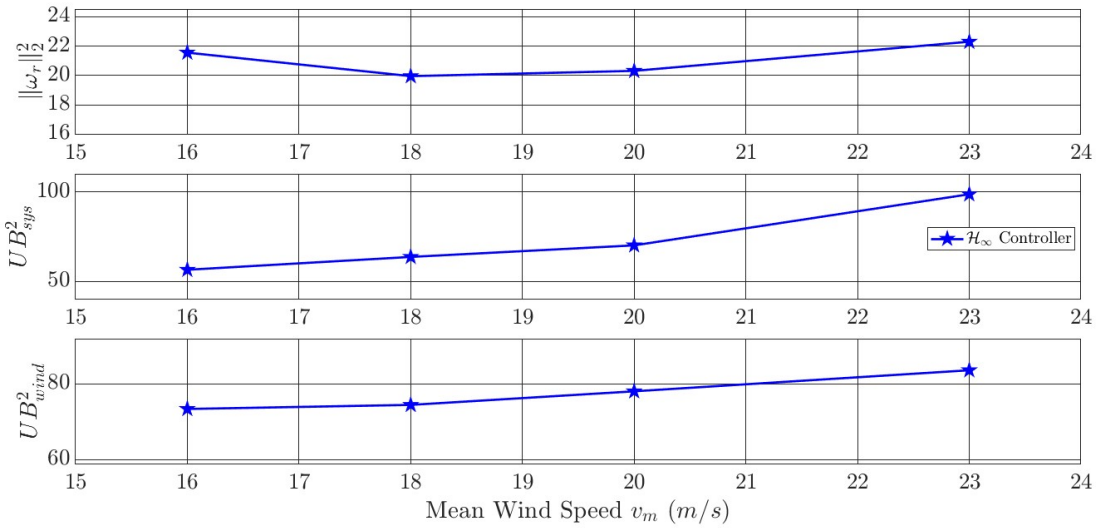

Figure 4.13: Results of the simulations for the rotor speed output performed at different mean wind speeds for the $\mathcal{H}_\infty$ control system. The top figure shows the $\mathcal{L}_2$-norm of the output. The middle and bottom figures show the upper bounds on the $\mathcal{L}_2$-norm of the output computed using the upper bounds on the induced norms from traditional analysis and IQC analysis, respectively.

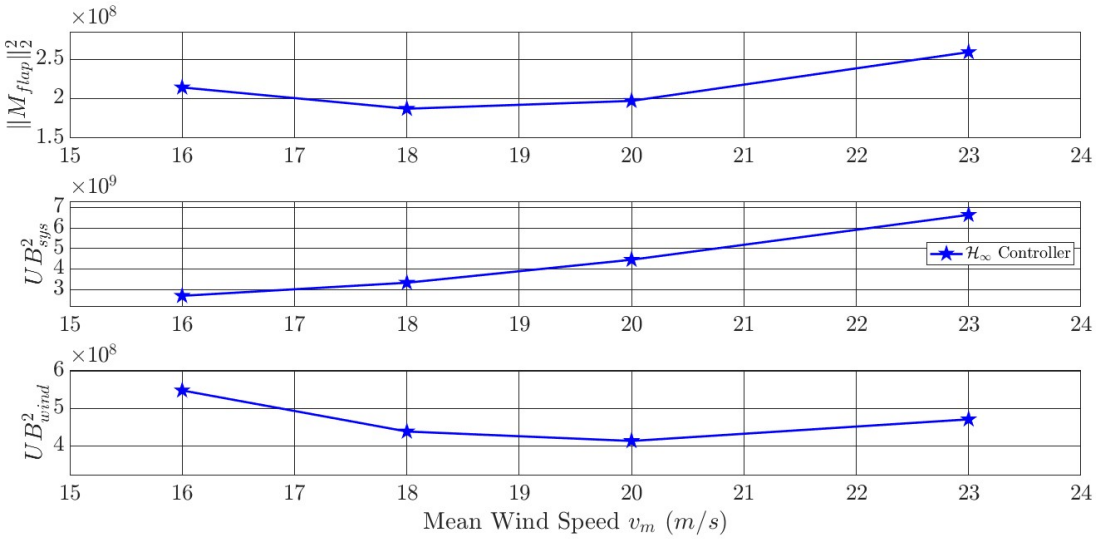

Figure 4.14: Results of the simulations for the blade flap-wise bending moment output performed at different mean wind speeds for the $\mathcal{H}_\infty$ control system. The top figure shows the $\mathcal{L}_2$-norm of the output. The middle and bottom figures show the upper bounds on the $\mathcal{L}_2$-norm of the output computed using the upper bounds on the induced norms from traditional analysis and IQC analysis, respectively.

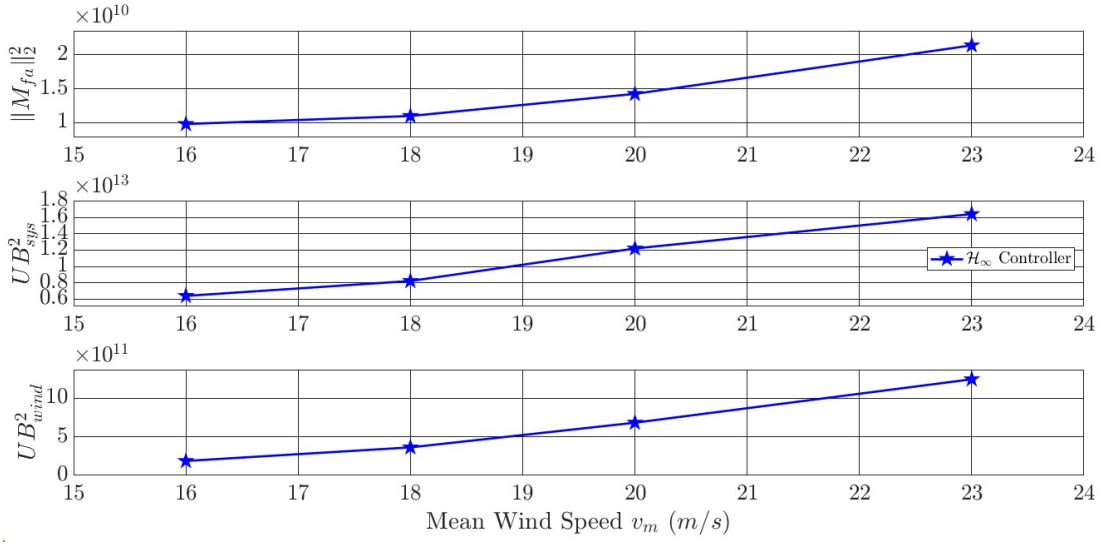

Figure 4.15: Results of the simulations for the tower fore-aft bending moment output performed at different mean wind speeds for the $\mathcal{H}_\infty$ control system. The top figure shows the $\mathcal{L}_2$-norm of the output. The middle and bottom figures show the upper bounds on the $\mathcal{L}_2$-norm of the output computed using the upper bounds on the induced norms from traditional analysis and IQC analysis, respectively.

It can be observed from Figures 4.13 - 4.15 that guaranteed upper bounds on the $\mathcal{L}_2$-norms of the outputs are obtained. For the blade flap-wise and tower fore-aft bending moments, it is observed that the order of magnitude of UB_{wind}^2 is smaller than that of UB_{sys}^2. That is, the upper bounds on the $\mathcal{L}_2$-norms of the outputs computed using the $\mathcal{D}_w$-to-$\mathcal{L}_2$-induced norms obtained from IQC analysis are less conservative than those computed using the $\mathcal{L}_2$-induced norms obtained from traditional analysis. This is also observed to be true at high mean wind speeds for the case of the rotor speed output.

4.6 Limitations

Violations of the Upper Bounds: Out of the 3000 simulations performed on the four different wind speeds, two violations of the obtained theoretical upper bounds were observed at $v_m = 16\ m/s$. Namely, the upper bounds on the $\mathcal{D}_w$-to-$\mathcal{L}_2$-induced norms obtained from IQC analysis for the rotor speed and blade flap-wise bending moment outputs were violated twice in the 3000 simulations performed at a mean wind speed of 16 m/s. The reason behind these violations is highlighted in what follows. For example, the results of a sample simulation of the $\mathcal{H}_\infty$ controller at a mean wind speed of 16 m/s are presented in Figure 4.16. At approximately 220 seconds, the wind speed drops below 10.5 m/s, i.e., it dropped to Region 2 of the wind turbine operation (below 11.4 m/s). This results in a major change in the system dynamics. This can be observed in the responses of the rotor speed and blade flap-wise bending moment at the same instant, wherein large spikes occurred in the nonlinear responses, and the responses of the linear and nonlinear systems

no longer match. To overcome this problem, a different type of controller should be designed. That is, wind turbines have a different mode of operation in Region 2, and therefore, in this region, a generator torque controller should be used, while fixing the blade pitch angle to a constant, optimal, value. Another solution consists in quantifying the linearization error, which might not be an easy task. Then, the linearization error can be added as an uncertainty in the IQC framework. This approach can improve the analysis at mean wind speeds other than $v_m = 16\ m/s$ too.

Controller Comparison: The proposed framework has failed in comparing the performance of the two designed controllers in the case of the tower fore-aft bending moment as shown in Figure 4.7. This problem might be a result of the high dependence of the results on the signal IQCs pole locations. As discussed earlier, choosing the appropriate poles requires extensive tuning and sweeping, and thus, finding another set of poles might solve this problem. This problem requires further investigation in the future.

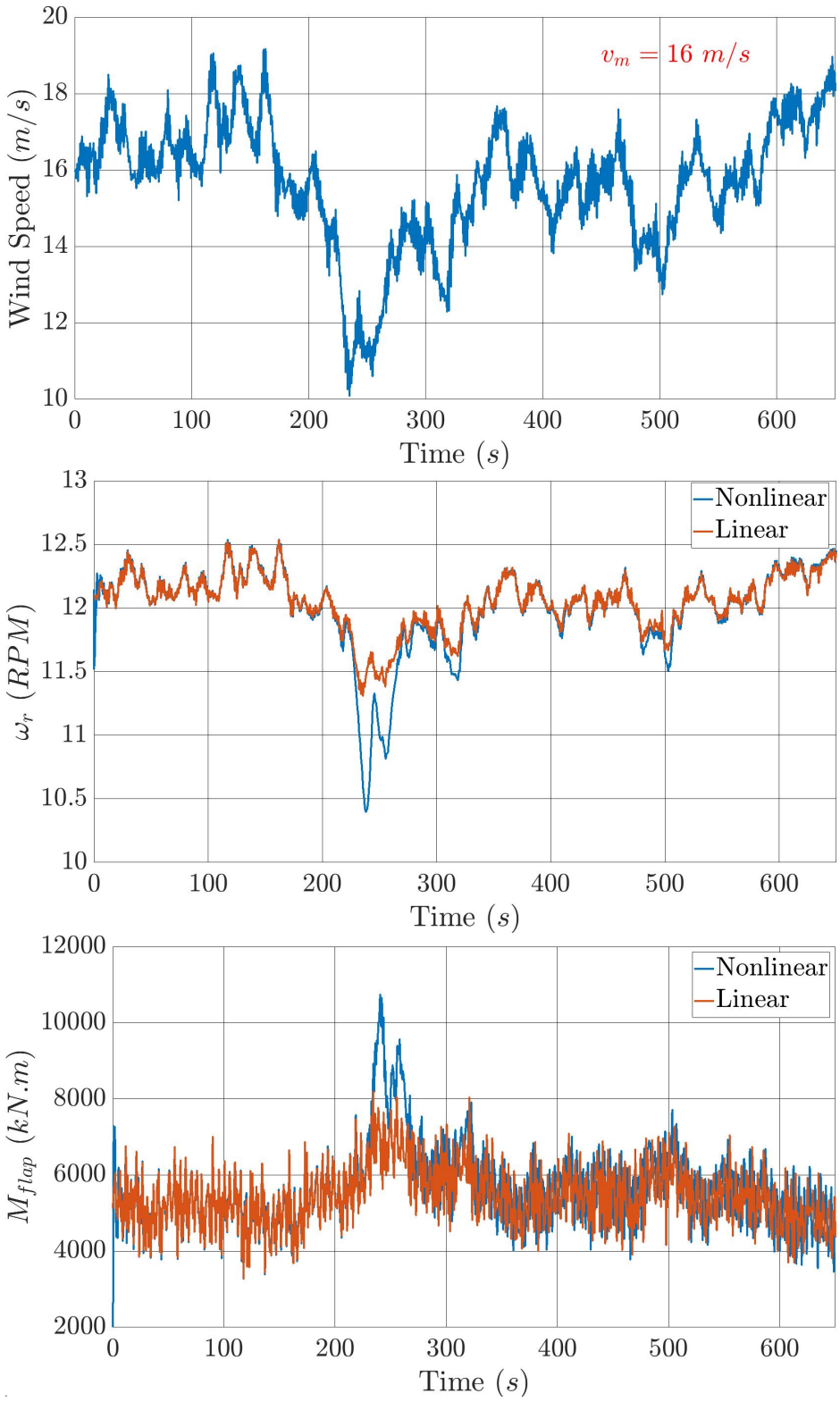

Figure 4.16: Sample simulation results for $\mathcal{H}_\infty$ controller at a mean wind speed of 16 m/s. Top figure shows the used wind profile. Middle and bottoms figures show the responses of the rotor speed and blade flap-wise bending moment, respectively, upon simulating the linear and nonlinear wind turbine models.

Chapter 5

CONCLUSION

This thesis proposes a framework for robustness analysis of wind turbine control systems. In the proposed framework, the characteristics of a turbulent wind profile are incorporated in the analysis of the closed-loop wind turbine system by adding a wind model to the wind turbine model. The resulting combined wind turbine model has white noise inputs and contains time-varying parameters that are treated as uncertainties. This system is modeled in the Linear Fractional Transformation (LFT) framework, and the theory of Integral Quadratic Constraints (IQCs) is used to model the uncertainties as static linear time-varying (SLTV) parameters. In addition, the white noise inputs of the model are characterized via signal IQCs.

Linearizations of the nonlinear wind turbine model are obtained at different operating wind speeds, and $\mathcal{H}_\infty$ and PI blade pitch controllers are synthesized with the objective of maintaining the turbine's generated power at its rated value in Region 3 of the wind turbine operation. The proposed framework is employed to examine and compare the robustness of the two wind turbine control systems. The induced norm of the closed-loop system is used as the performance metric. The analysis results are validated via extensive simulations of a high-fidelity nonlinear wind turbine model. The proposed analysis framework allows for a better characterization of the system's performance. Both types of analyses performed in this thesis, traditional KYP analysis and the proposed IQC-based analysis, guide the control design process. Even though the synthesis and IQC analysis problems are decoupled in this thesis, the results of the IQC analysis allowed for testing the controller, and therefore, motivated the need for tuning the weights of the outputs used in control synthesis. Hence, satisfactory controllers were designed by iteratively repeating the two aforementioned steps.

Potential directions for future work include the following:

1. Other wind models can be incorporated in the proposed analysis framework. In this thesis, a wind model based on the Kaimal spectrum is used. Another wind model that can be used is that based on the von Karmen spectrum.

2. Better wind turbine models can be used in the proposed analysis framework. In this thesis, a linear time-invariant model is used. Other models include periodic linear time-varying and linear parameter-varying models that capture

Regions 2 and 3 of the wind turbine operation.

3. Better controllers can be designed to test the validity of the proposed framework. In this thesis, $\mathcal{H}_\infty$ and PI controllers are synthesized at one operating wind speed. $\mathcal{H}_2$ controllers may also be considered. Also, gain-scheduled controllers and linear parameter-varying controllers that capture Regions 2 and 3 of the wind turbine operation can be designed. In addition, multi-objective controllers can be designed, whereby, more than one performance output are penalized simultaneously.

4. The IQC theory can be incorporated in the controller design problem. In this thesis, controllers were designed for the nominal system, and then the closed-loop uncertain system is analyzed using IQC theory. Alternatively, an IQC-based controller synthesis algorithm can be designed and implemented.

5. The proposed framework can be tested on all regions of the wind turbine operation. In this thesis, it was tested in Region 3 only. Controllers can be also designed for Region 2, and their robustness can be examined using the proposed framework.

6. Additional uncertainties and nonlinearities of the wind turbine model can be added to the proposed framework. Specifically, the linearization error of the wind turbine model should be quantified and incorporated in the IQC analysis.

7. Better and automatic tuning methods of signal IQC poles can be developed.

8. The MCrunch package [50] developed by NREL can be used to analyse and compare the loads on the wind turbine components obtained from the simulation results. That is, MCrunch allows for computing the damage equivalent loads (DELs) metric, which indicates the equivalent fatigue damage. Specifically, the load reduction of the two controllers designed in this thesis can be compared by evaluating the DELs for the blade flap-wise and tower fore-aft bending moments.

9. Other numerical methods can be used to solve the convex optimization problems. In this thesis, off-the-shelf solvers, which are based on interior point methods, were used. Instead, cutting plane methods, which exploit the structure of the SDP and lower its computational cost, can be applied alternatively. For instance, the analytic center cutting plane method, which is applied in [51]–[53] to the discrete-time IQC problem, can be used to solve the SDPs in this thesis.

10. The worst-case input signals that yield the upper bounds on the induced norm of the wind turbine control system obtained in this thesis can be constructed. Two algorithms for constructing such input signals are presented for the case of a stable discrete-time LTV system in [54].

11. The scope of the work in this thesis can be extended from individual wind turbines to wind farms. Wind farms can be modeled as dynamic networked systems of wind turbines. Thus, existing results on $\mathcal{H}_\infty$ network optimization, such as those given in [55], can be implemented for wind farm optimization.

Appendix A

ADDITIONAL SIMULATIONS RESULTS

This appendix contains complementary/additional results, in the form of plots and tables, that were not reported in the main body of the thesis' text.

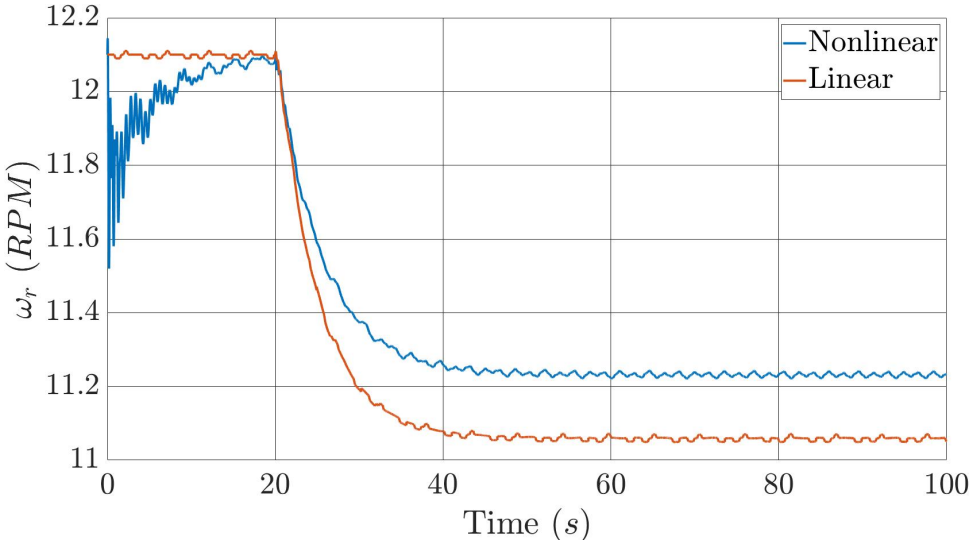

(a) Rotor speed

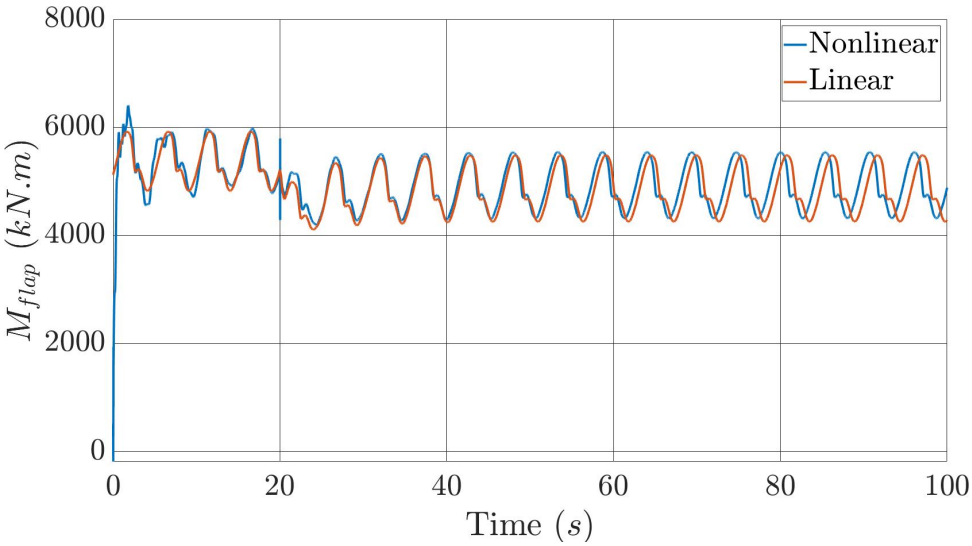

(b) Blade 1 flap-wise bending moment

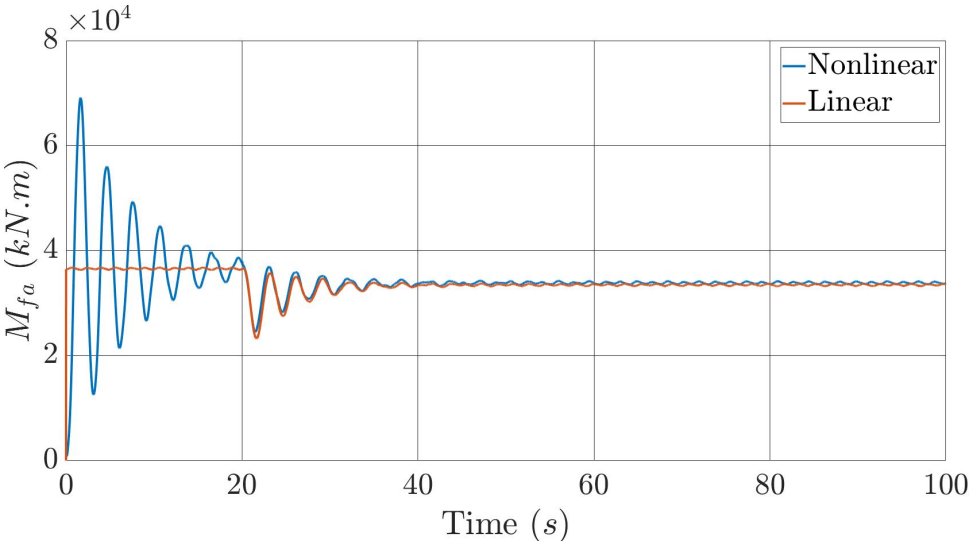

(c) Tower fore-aft bending moment

Figure A.1: Open-loop simulation results at $v_m = 16\ m/s$.

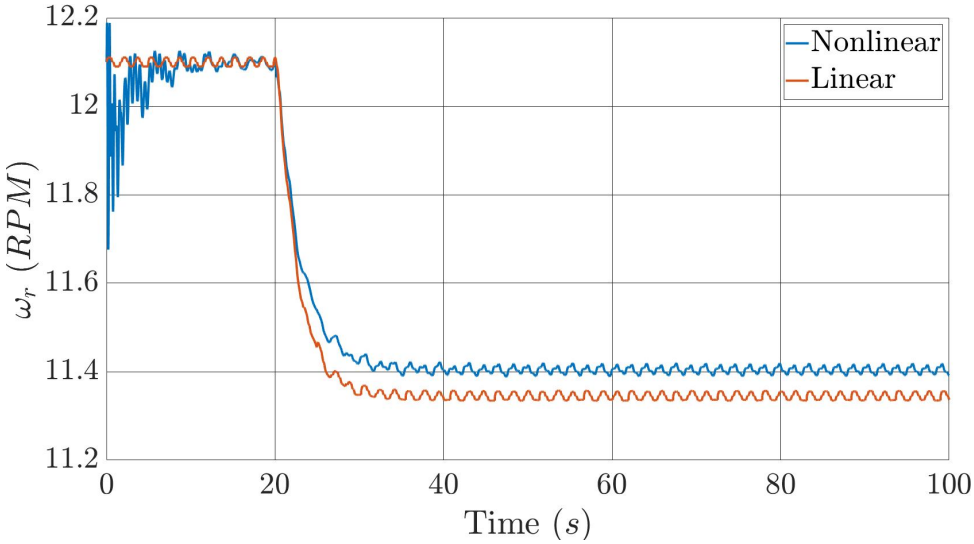

(a) Rotor speed

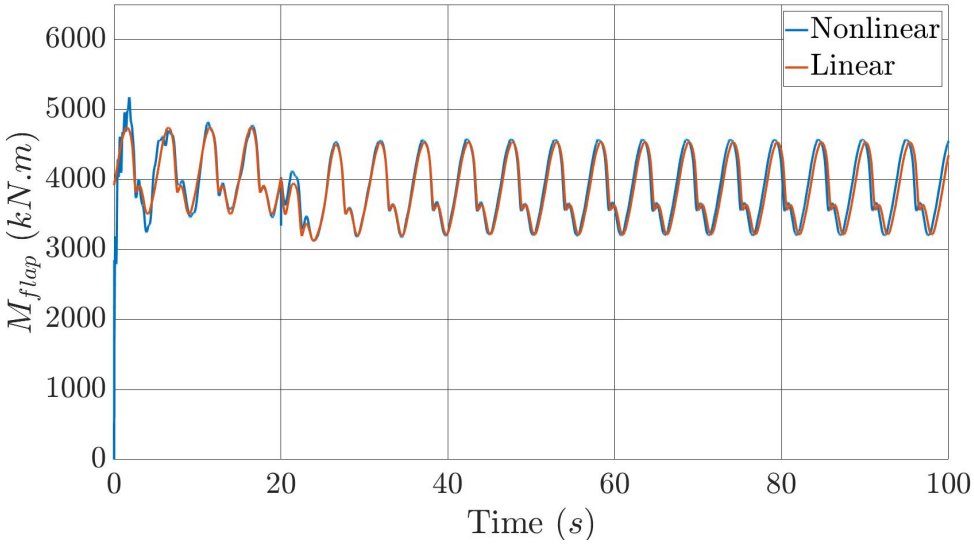

(b) Blade 1 flap-wise bending moment

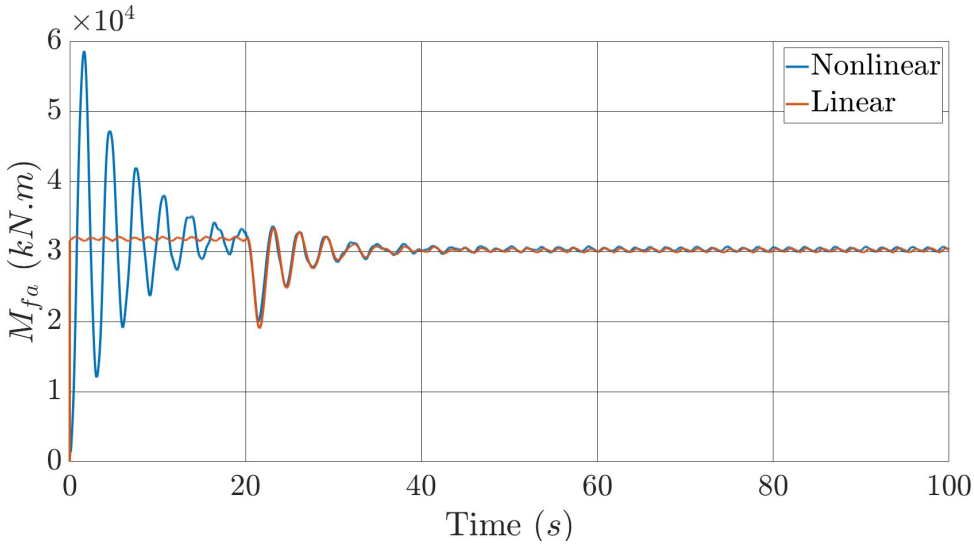

(c) Tower fore-aft bending moment

Figure A.2: Open-loop simulation results at $v_m = 20\ m/s$.

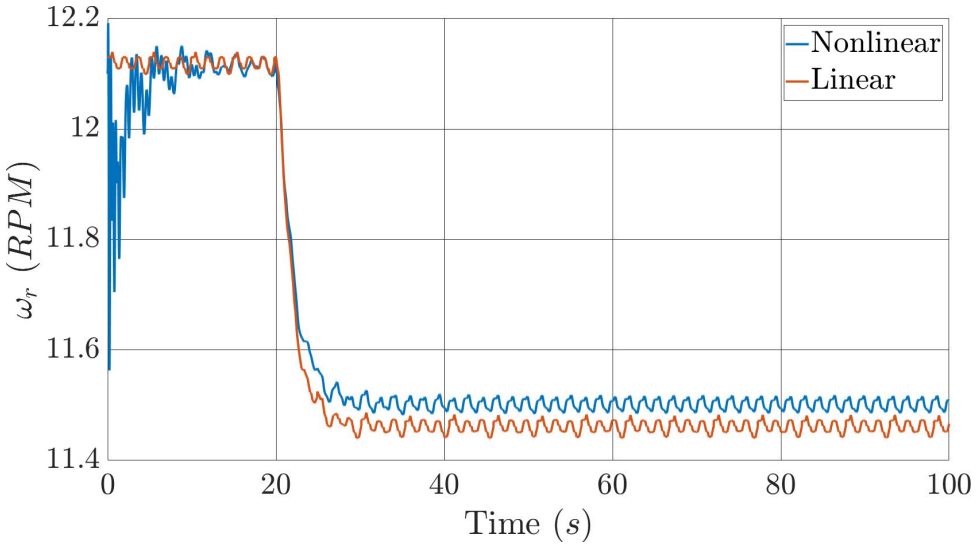

(a) Rotor speed

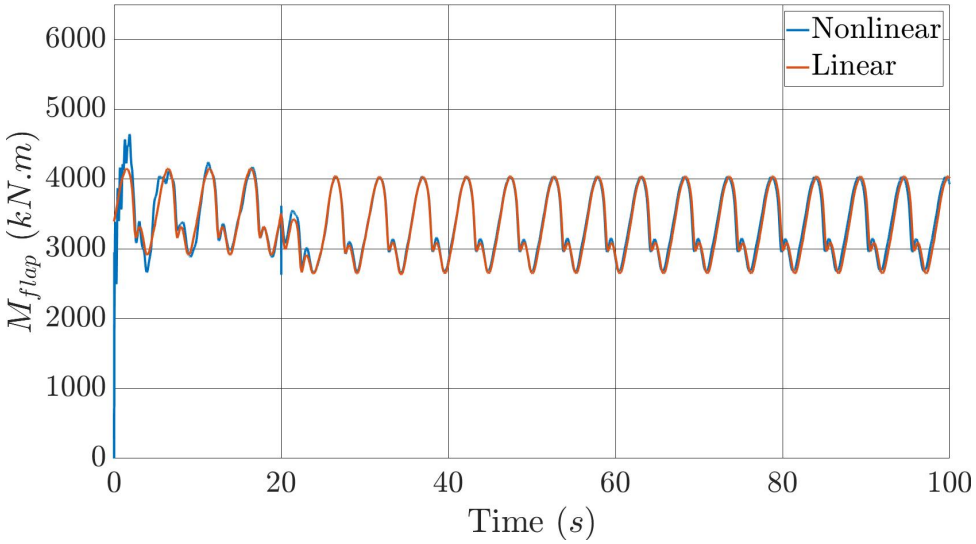

(b) Blade 1 flap-wise bending moment

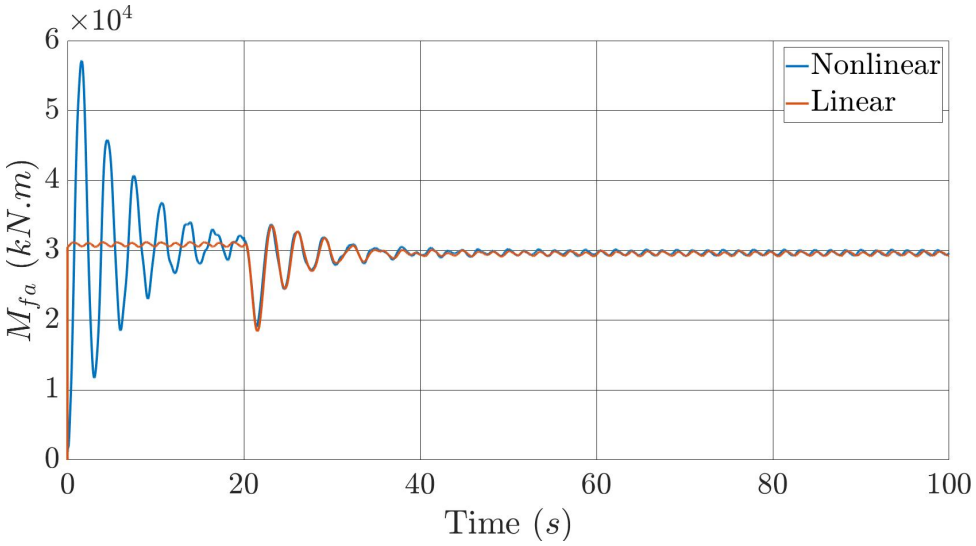

(c) Tower fore-aft bending moment

Figure A.3: Open-loop simulation results at $v_m = 23\ m/s$.

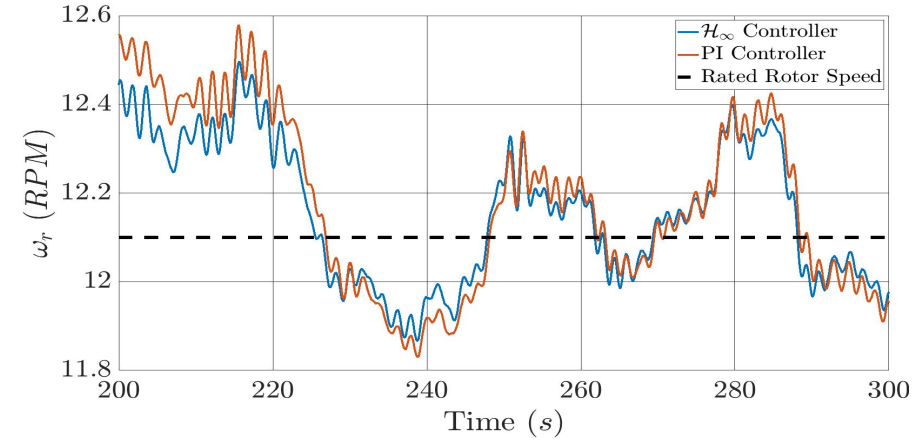

(a) Rotor speed

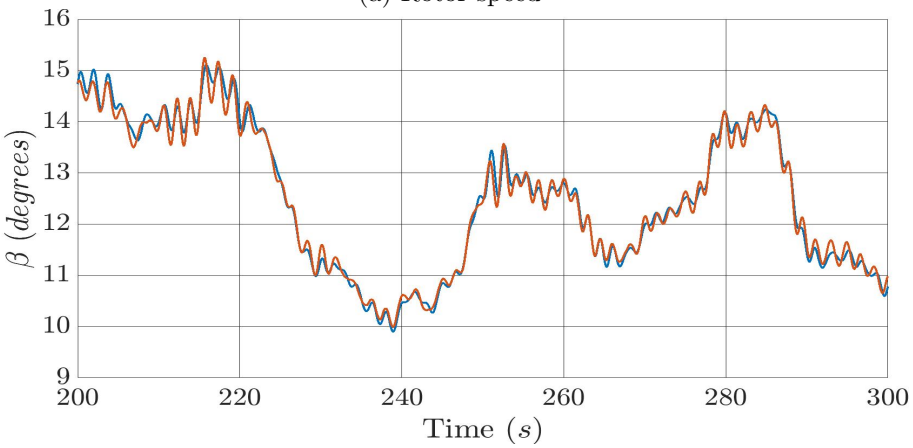

(b) Blade pitch angle

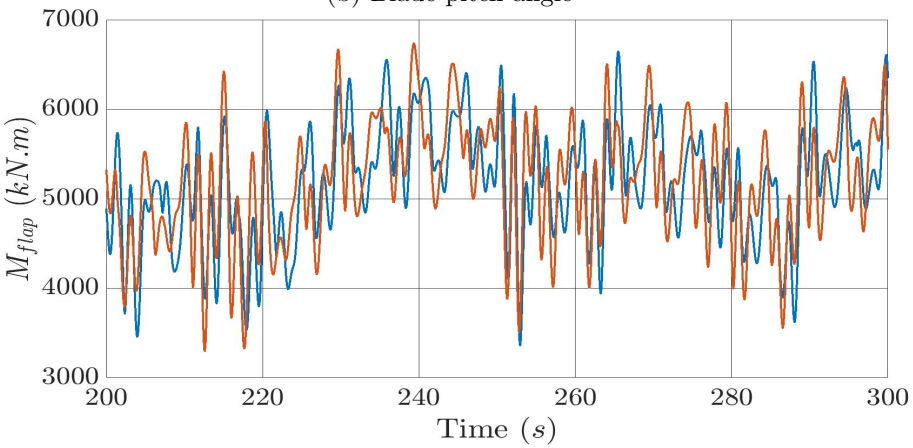

(c) Blade 1 flap-wise bending moment

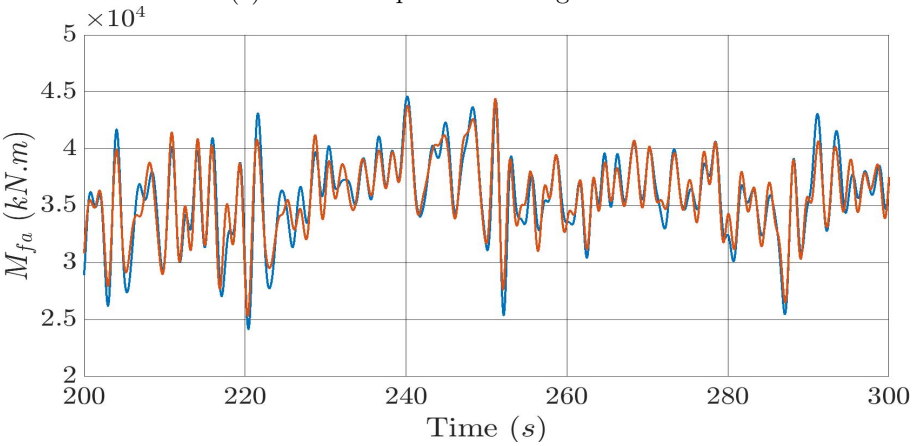

(d) Tower fore-aft bending moment

Figure A.4: Sample simulation results for the $\mathcal{H}_\infty$ and PI controllers at $v_m = 16\ m/s$.

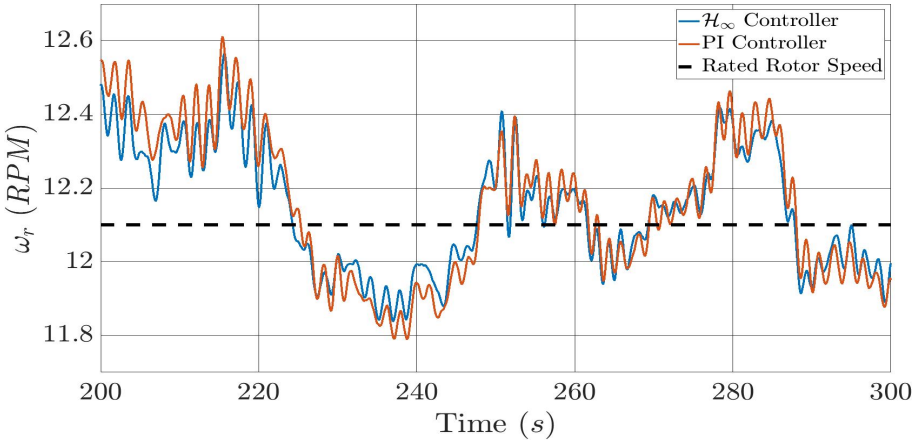

(a) Rotor speed

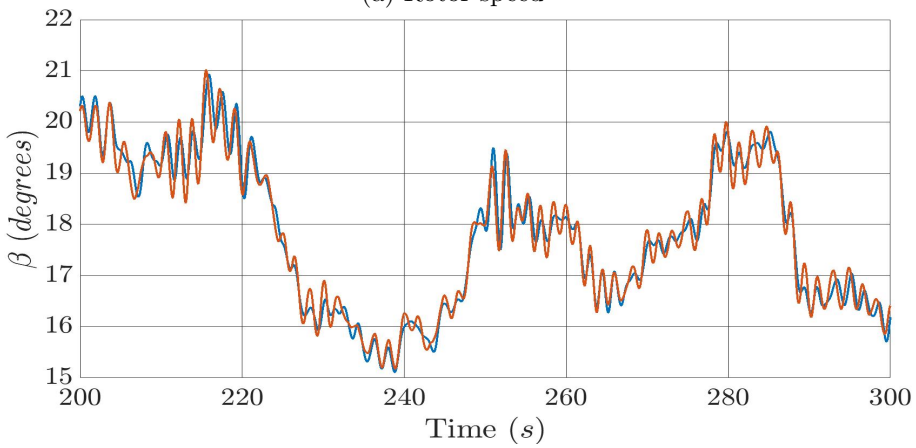

(b) Blade pitch angle

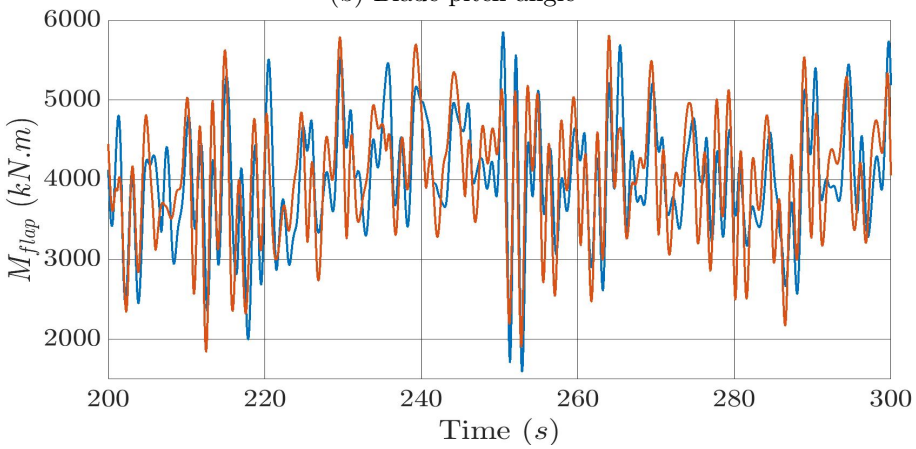

(c) Blade 1 flap-wise bending moment

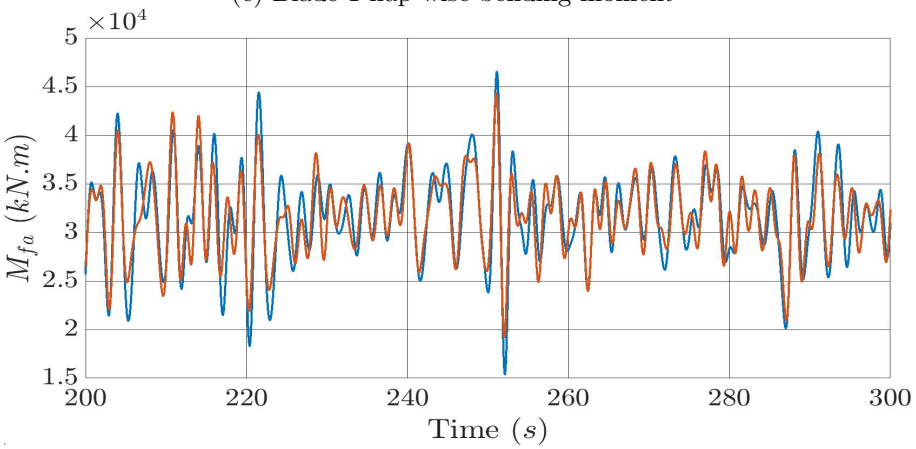

(d) Tower fore-aft bending moment

Figure A.5: Sample simulation results for the $\mathcal{H}_\infty$ and PI controllers at $v_m = 20\ m/s$.

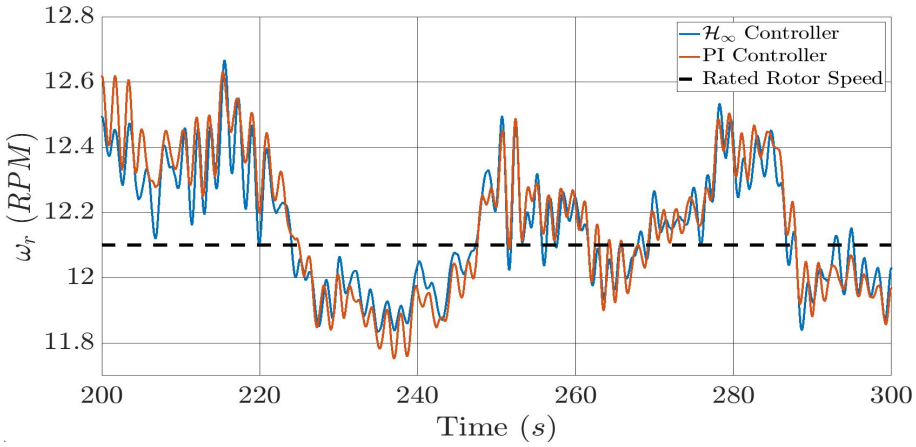

(a) Rotor speed

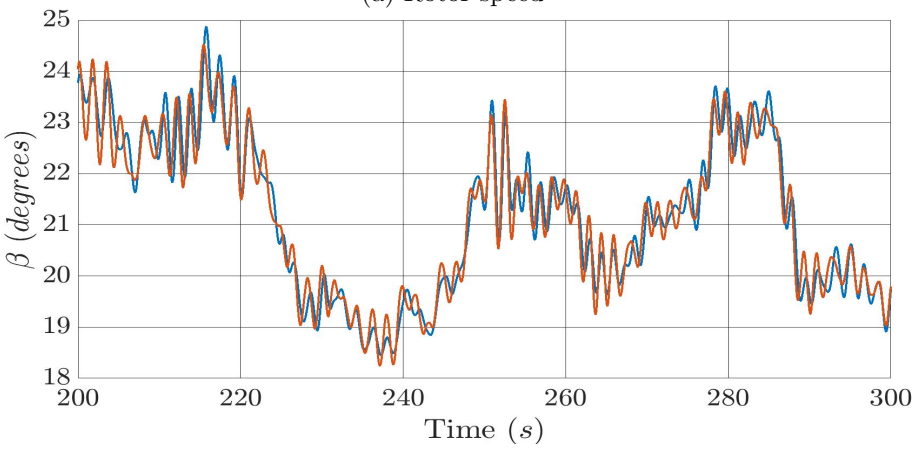

(b) Blade pitch angle

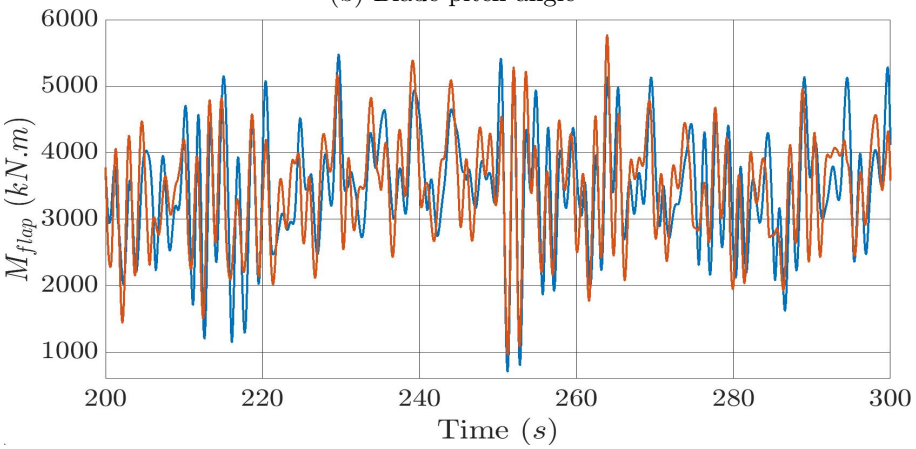

(c) Blade 1 flap-wise bending moment

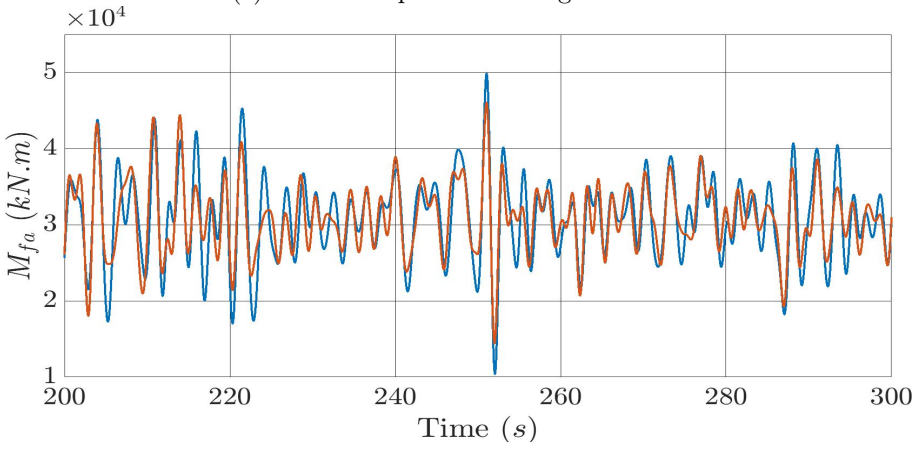

(d) Tower fore-aft bending moment

Figure A.6: Sample simulation results for the $\mathcal{H}_\infty$ and PI controllers at $v_m = 23\ m/s$.

Table A.1: $\mathcal{L}_2$-induced norms for the tower fore-aft bending moment output for the case of traditional analysis. $\bar{\gamma}^{\mathbf{2}}_{\mathbf{fa,sys,sim}}$ and $\overset{\max}{\gamma}{}^{\mathbf{2}}_{\mathbf{fa,sys,sim}}$ denote the squares of the average and maximum γ values obtained from the simulations, respectively.

Controller	$\mathbf{v_m}$	$\gamma^{\mathbf{2}}_{\mathbf{fa,sys,th}} \times \mathbf{10^{-10}}$	$\bar{\gamma}^{\mathbf{2}}_{\mathbf{fa,sys,sim}} \times \mathbf{10^{-10}}$	$\overset{\max}{\gamma}{}^{\mathbf{2}}_{\mathbf{fa,sys,sim}} \times 10^{-10}$
PI Controller	**16**	0.5919	0.0005	0.0018
	18	0.77	0.0008	0.0017
	20	1.0314	0.0008	0.0017
	23	1.2939	0.0009	0.0019
$\mathcal{H}_\infty$ **Controller**	**16**	0.7269	0.0005	0.0022
	18	0.737	0.001	0.0022
	20	0.8848	0.0011	0.0023
	23	0.8997	0.0012	0.0024

Table A.2: $\mathcal{D}_w$-to-$\mathcal{L}_2$-induced norms for the tower fore-aft bending moment output for the case of IQC analysis. $\bar{\gamma}^{\mathbf{2}}_{\mathbf{fa,wind,sim}}$ and $\overset{\max}{\gamma}{}^{\mathbf{2}}_{\mathbf{fa,wind,sim}}$ denote the squares of the average and maximum γ values obtained from the simulations, respectively.

Controller	$\mathbf{v_m}$	$\gamma^{\mathbf{2}}_{\mathbf{fa,wind,th}} \times \mathbf{10^{-10}}$	$\bar{\gamma}^{\mathbf{2}}_{\mathbf{fa,wind,sim}} \times \mathbf{10^{-10}}$	$\overset{\max}{\gamma}{}^{\mathbf{2}}_{\mathbf{fa,wind,sim}} \times 10^{-10}$
PI Controller	**16**	0.011	0.0005	0.0012
	18	0.0232	0.0005	0.0007
	20	0.0479	0.0006	0.0008
	23	0.1053	0.0009	0.0012
$\mathcal{H}_\infty$ **Controller**	**16**	0.0104	0.0005	0.0014
	18	0.0202	0.0006	0.0009
	20	0.038	0.0008	0.001
	23	0.0693	0.0012	0.0015

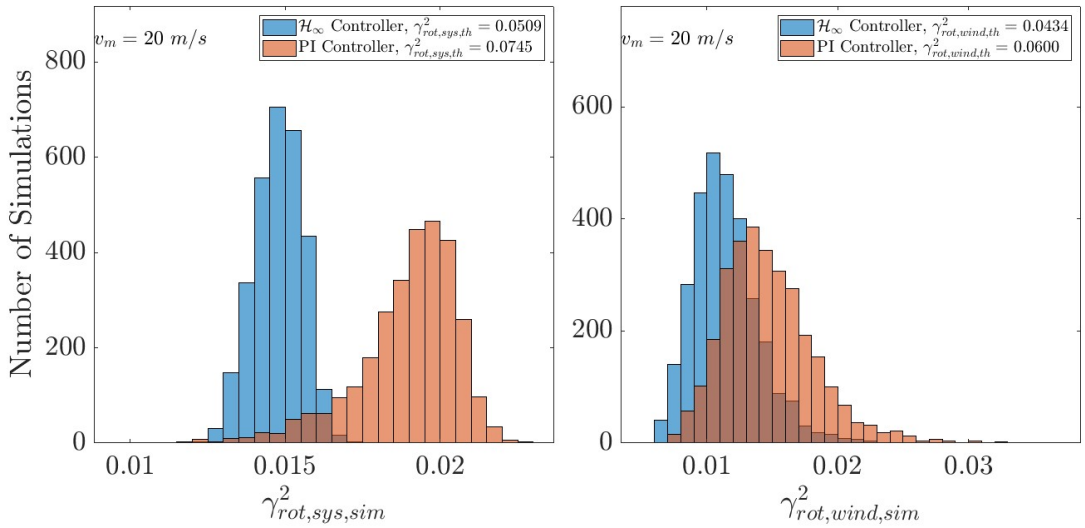

Figure A.7: Results of the simulations performed at a mean wind speed of 20 m/s. The figure shows the square of the experimental γ values of the wind turbine control systems where the rotor speed is chosen as the performance output. The left figure corresponds to traditional analysis. The right figure corresponds to IQC analysis.

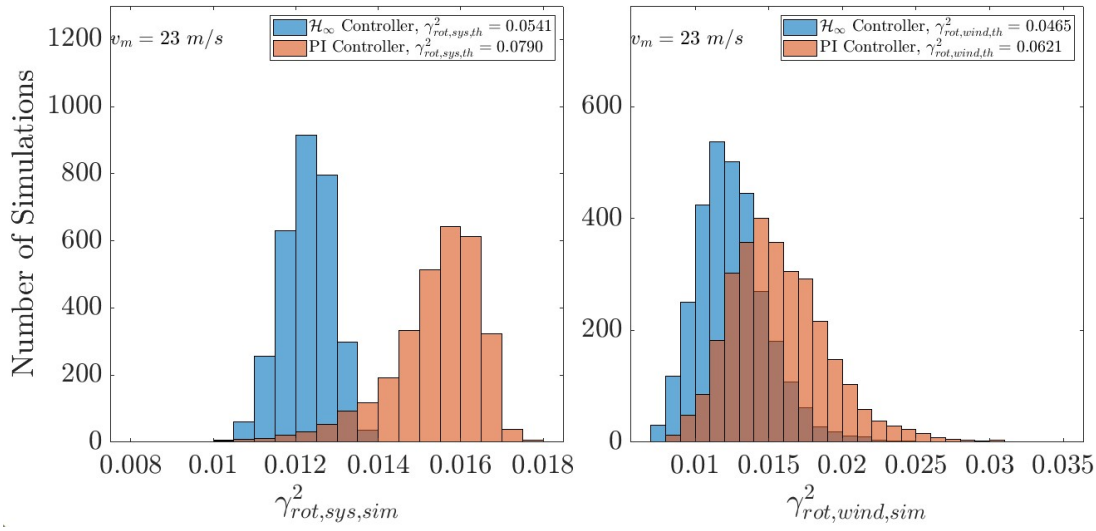

Figure A.8: Results of the simulations performed at a mean wind speed of 23 m/s. The figure shows the square of the experimental γ values of the wind turbine control systems where the rotor speed is chosen as the performance output. The left figure corresponds to traditional analysis. The right figure corresponds to IQC analysis.

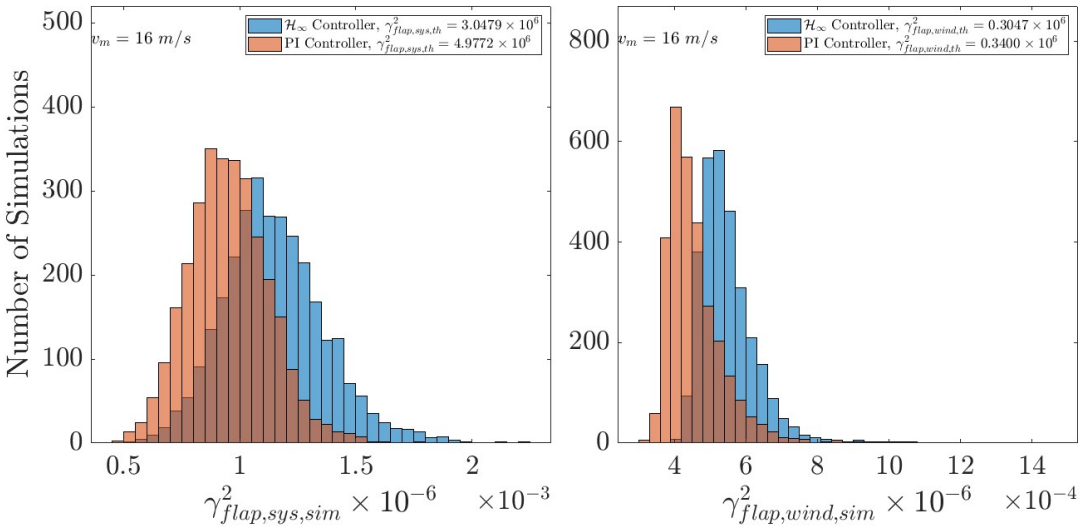

Figure A.9: Results of the simulations performed at a mean wind speed of 16 m/s. The figure shows the square of the experimental γ values of the wind turbine control systems where the blade flap-wise bending moment is chosen as the performance output. The left figure corresponds to traditional analysis. The right figure corresponds to IQC analysis.

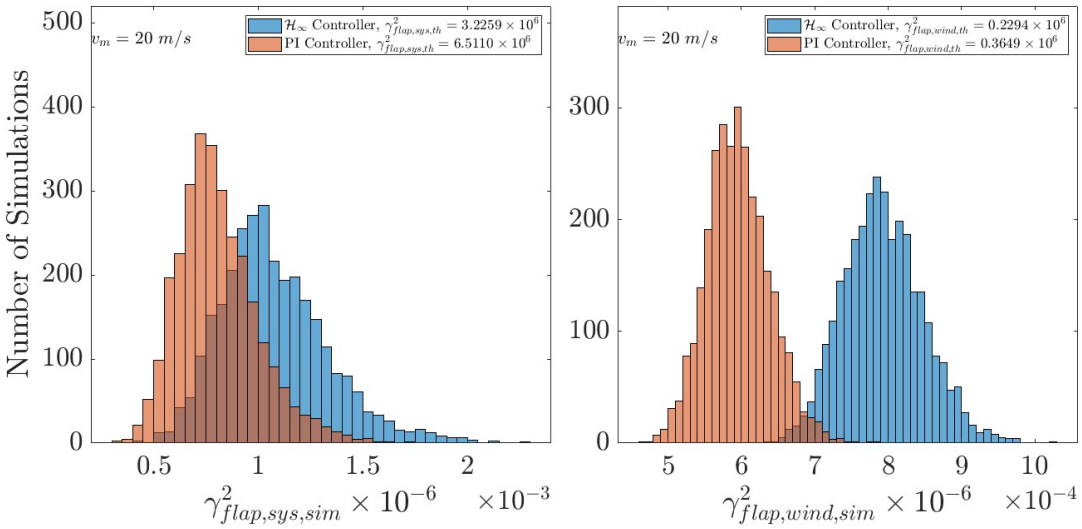

Figure A.10: Results of the simulations performed at a mean wind speed of 20 m/s. The figure shows the square of the experimental γ values of the wind turbine control systems where the blade flap-wise bending moment is chosen as the performance output. The left figure corresponds to traditional analysis. The right figure corresponds to IQC analysis.

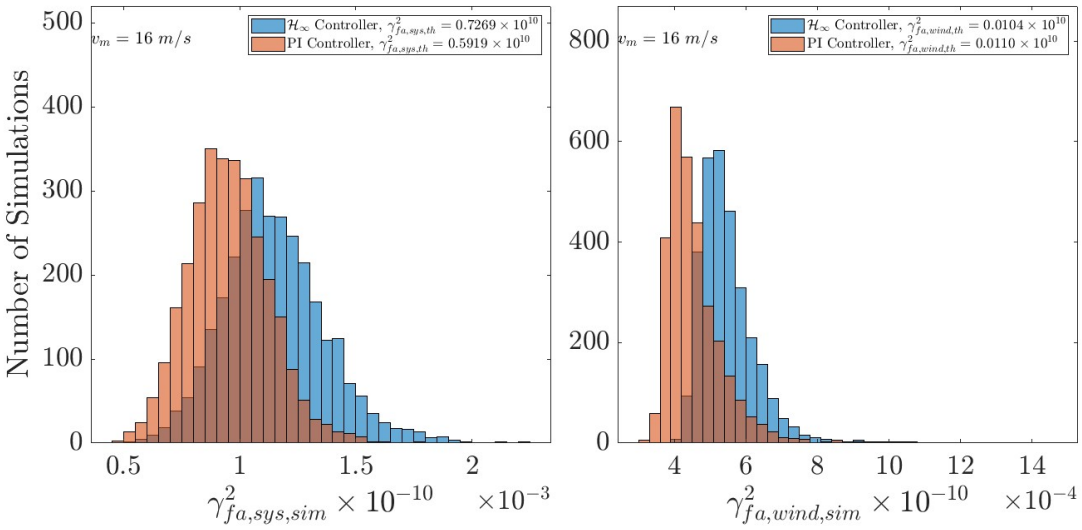

Figure A.11: Results of the simulations performed at a mean wind speed of 16 m/s. The figure shows the square of the experimental γ values of the wind turbine control systems where the tower fore-aft bending moment is chosen as the performance output. The left figure corresponds to traditional analysis. The right figure corresponds to IQC analysis.

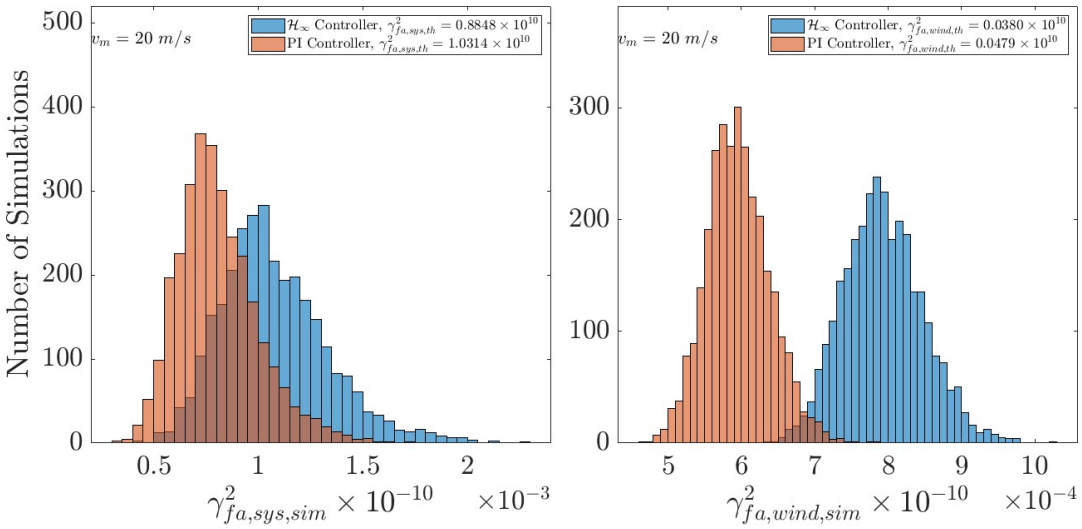

Figure A.12: Results of the simulations performed at a mean wind speed of 20 m/s. The figure shows the square of the experimental γ values of the wind turbine control systems where the tower fore-aft bending moment is chosen as the performance output. The left figure corresponds to traditional analysis. The right figure corresponds to IQC analysis.

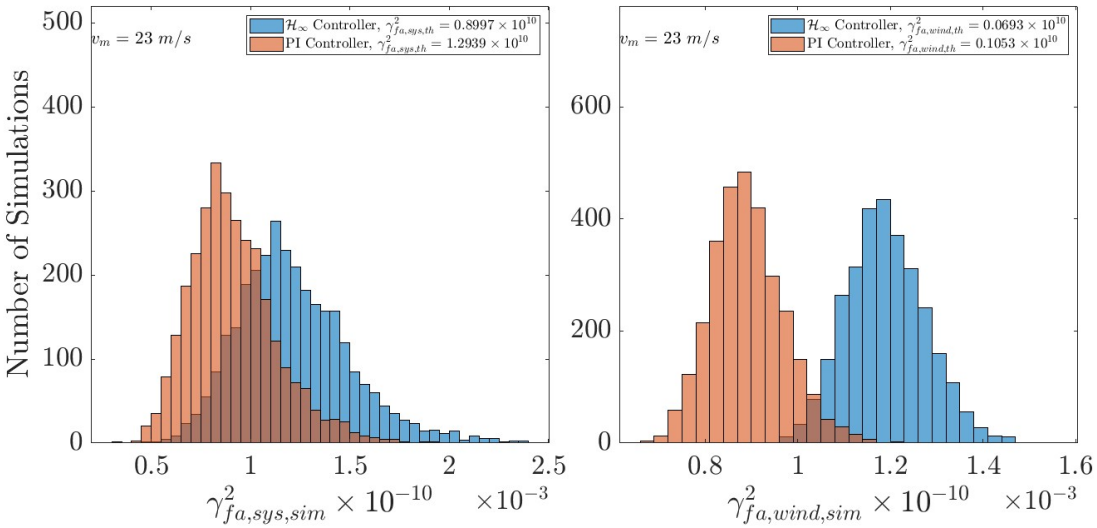

Figure A.13: Results of the simulations performed at a mean wind speed of 23 m/s. The figure shows the square of the experimental γ values of the wind turbine control systems where the tower fore-aft bending moment is chosen as the performance output. The left figure corresponds to traditional analysis. The right figure corresponds to IQC analysis.

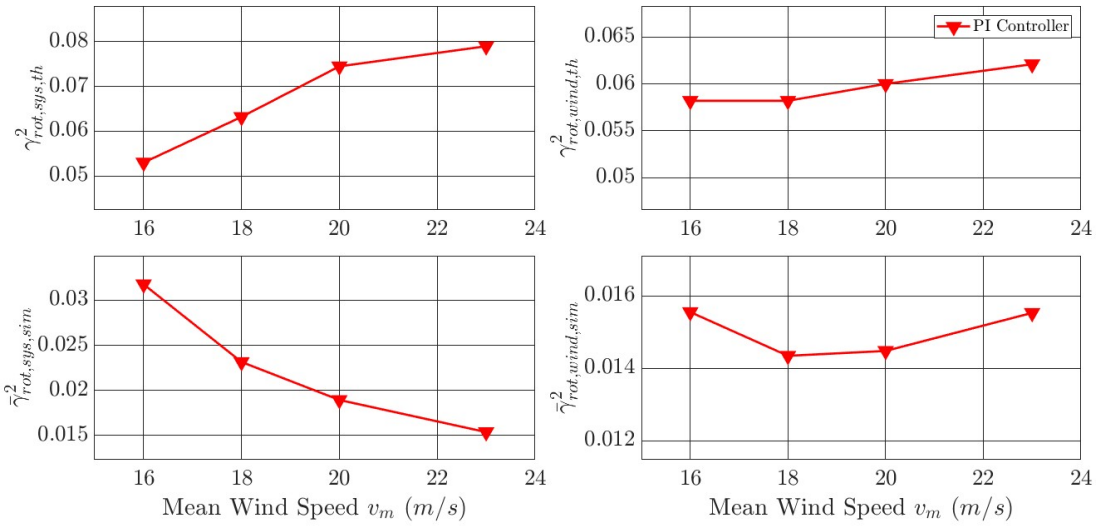

Figure A.14: Results of the analysis and simulations performed at different mean wind speeds. The figure shows the square of the induced norms of the wind turbine system, for the case of the PI controller, where the rotor speed is chosen as the performance output. The top left figure shows the upper bounds on the square of the $\mathcal{L}_2$-induced norm obtained from the traditional analysis. The top right figure shows the upper bounds on the square of the $\mathcal{D}_w$-to-$\mathcal{L}_2$-induced norms obtained from IQC analysis. The bottom left figure shows the square of the average of the experimental γ values obtained from the simulations for the case of turbulent wind input. The bottom right figure shows the square of the average of the experimental γ values obtained from the simulations for the case of white noise inputs.

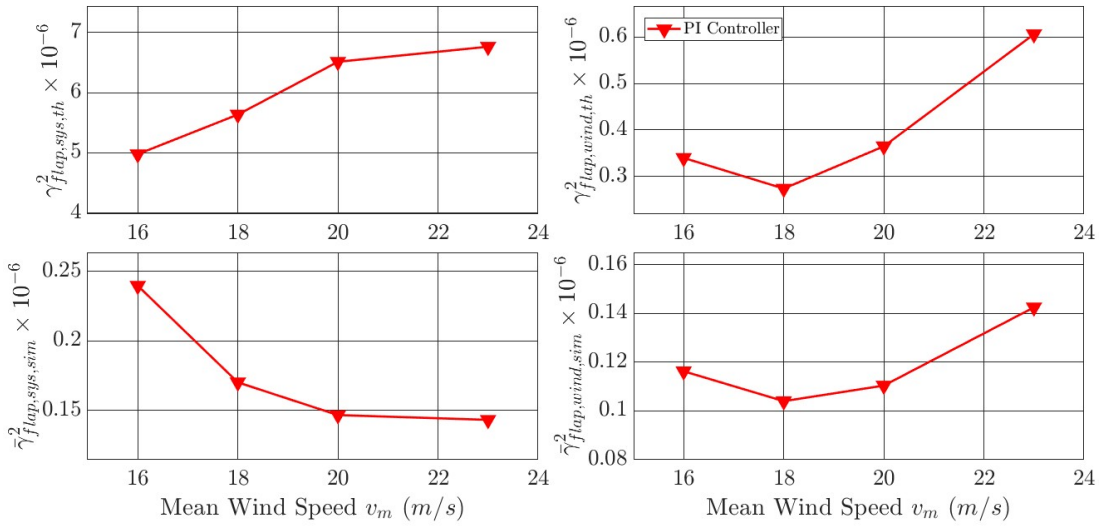

Figure A.15: Results of the analysis and simulations performed at different mean wind speeds. The figure shows the square of the induced norms of the wind turbine system, for the case of the PI controller, where the blade flap-wise bending moment is chosen as the performance output. The top left figure shows upper bounds on the square of the $\mathcal{L}_2$-induced norm obtained from traditional analysis. The top right figure shows upper bounds on the square of the $\mathcal{D}_w$-to-$\mathcal{L}_2$-induced norms obtained from IQC analysis. The bottom left figure shows the square of the average of the experimental γ values obtained from the simulations for the case of turbulent wind input. The bottom right figure shows the square of the average of the experimental γ values obtained from the simulations for the case of white noise inputs.

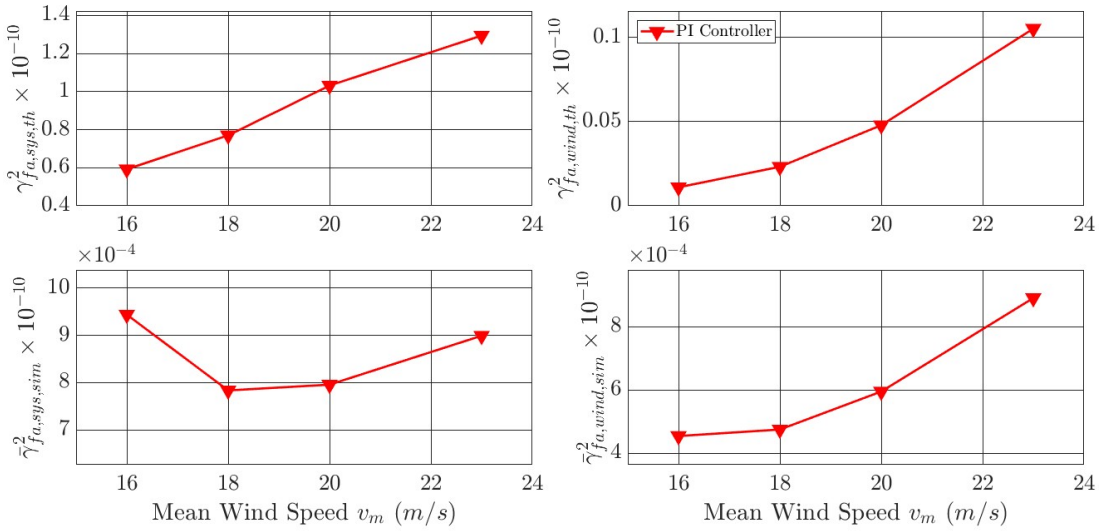

Figure A.16: Results of the analysis and simulations performed at different mean wind speeds. The figure shows the square of the induced norms of the wind turbine system, for the case of the PI controller, where the tower fore-aft bending moment is chosen as the performance output. The top left figure shows upper bounds on the square of the $\mathcal{L}_2$-induced norm obtained from traditional analysis. The top right figure shows upper bounds on the square of the $\mathcal{D}_w$-to-$\mathcal{L}_2$-induced norms obtained from IQC analysis. The bottom left figure shows the square of the average of the experimental γ values obtained from the simulations for the case of turbulent wind input. The bottom right figure shows the square of the average of the experimental γ values obtained from the simulations for the case of white noise inputs.

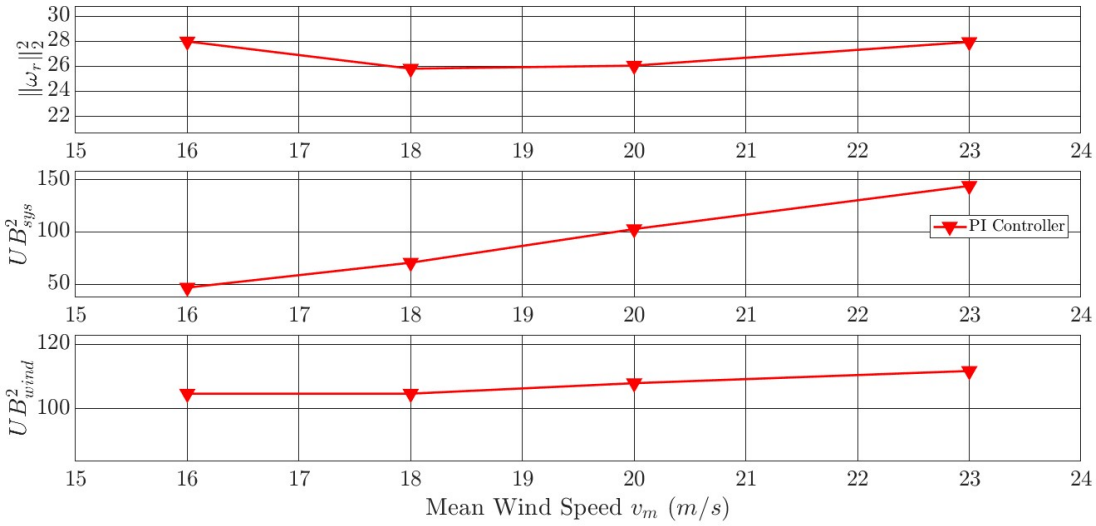

Figure A.17: Results of the simulations for the rotor speed output performed at different mean wind speeds for the PI control system. The top figure shows the $\mathcal{L}_2$-norm of the output. The middle and bottom figures show the upper bounds on the $\mathcal{L}_2$-norm of the output computed using the upper bounds on the induced norms from traditional analysis and IQC analysis, respectively.

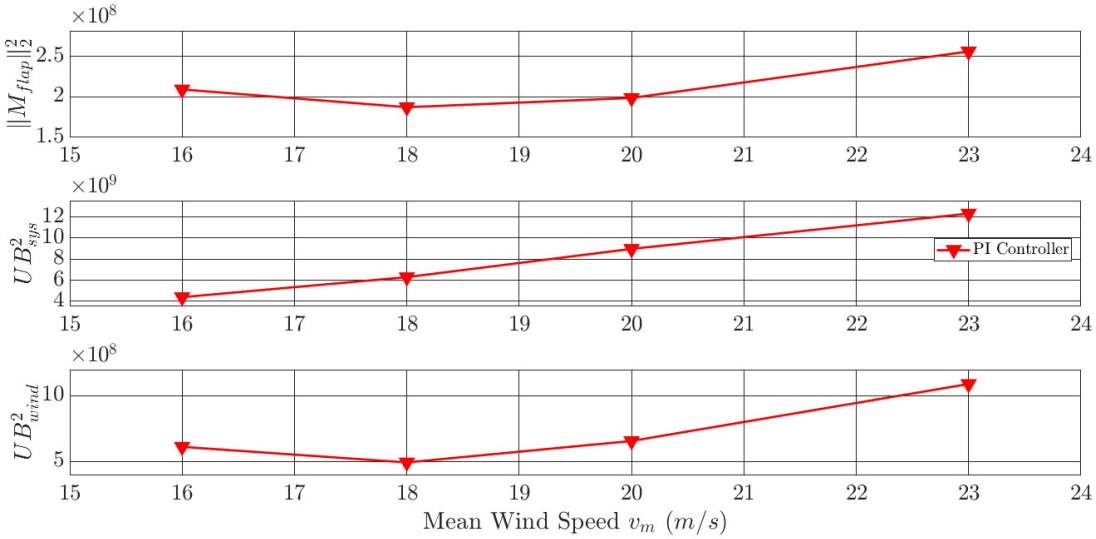

Figure A.18: Results of the simulations for the blade flap-wise bending moment output performed at different mean wind speeds for the PI control system. The top figure shows the $\mathcal{L}_2$-norm of the output. The middle and bottom figures show the upper bounds on the $\mathcal{L}_2$-norm of the output computed using the upper bounds on the induced norms from traditional analysis and IQC analysis, respectively.

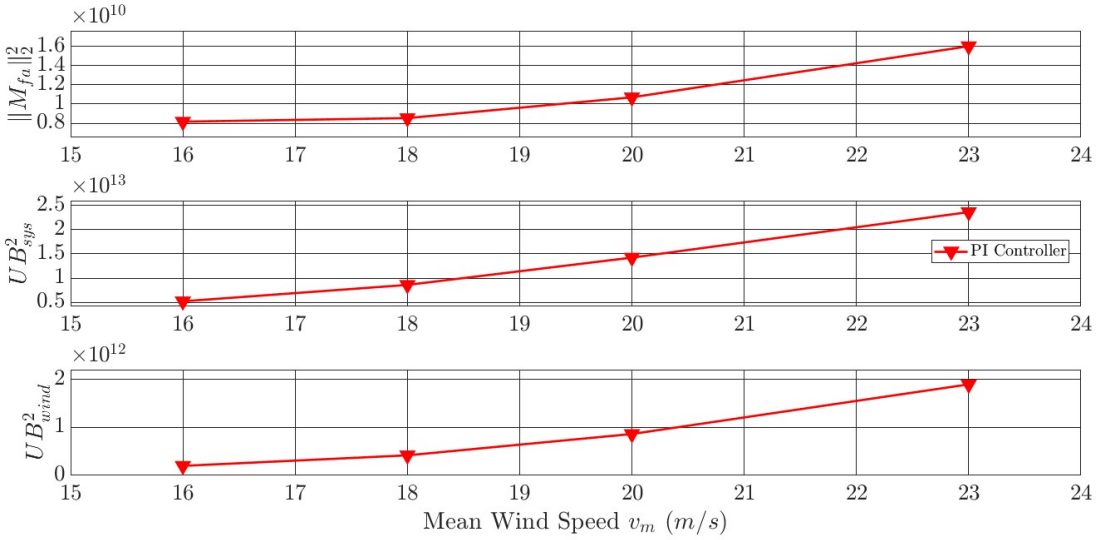

Figure A.19: Results of the simulations for the tower fore-aft bending moment output performed at different mean wind speeds for the PI control system. The top figure shows the $\mathcal{L}_2$-norm of the output. The middle and bottom figures show the upper bounds on the $\mathcal{L}_2$-norm of the output computed using the upper bounds on the induced norms from traditional analysis and IQC analysis, respectively.

Bibliography

[1] Global Wind Energy Council (GWEC), "Global wind report," 2021.

[2] J. M. Jonkman and M. Buhl Jr, "FAST user's guide," *National Renewable Energy Laboratory (NREL)*, 2005.

[3] L. Y. Pao and K. E. Johnson, "A tutorial on the dynamics and control of wind turbines and wind farms," in *Proceedings of the American Control Conference*, 2009, pp. 2076–2089.

[4] P. F. Odgaard, J. Stoustrup, and M. Kinnaert, "Fault-tolerant control of wind turbines: A benchmark model," *IEEE Transactions on Control Systems Technology*, vol. 21, no. 4, pp. 1168–1182, 2013.

[5] W. Langreder, "Models for variable speed wind turbines," M.S. thesis, Loughborough University, 1996.

[6] C. Jauch, "A simple wind model for fast wind farm simulations," *Wind Engineering*, vol. 38, no. 5, pp. 523–534, 2014.

[7] C. Nichita, D. Luca, B. Dakyo, and E. Ceanga, "Large band simulation of the wind speed for real time wind turbine simulators," *IEEE Transactions on Energy Conversion*, vol. 17, no. 4, pp. 523–529, 2002.

[8] T. Petru and T. Thiringer, "Modeling of wind turbines for power system studies," *IEEE Transactions on Power Systems*, vol. 17, no. 4, pp. 1132–1139, 2002.

[9] F. Zheng, Q.-G. Wang, and T. H. Lee, "On the design of multivariable PID controllers via LMI approach," *Automatica*, vol. 38, no. 3, pp. 517–526, 2002.

[10] C. Lin, Q.-G. Wang, and T. H. Lee, "An improvement on multivariable PID controller design via iterative LMI approach," *Automatica*, vol. 40, no. 3, pp. 519–525, 2004.

[11] Y.-Y. CAO, J. LAM, and Y.-X. SUN, "Static output feedback stabilization: An ILMI approach," *Automatica*, vol. 34, no. 12, pp. 1641–1645, 1998.

[12] K. Stol and M. Balas, "Full-state feedback control of a variable-speed wind turbine: A comparison of periodic and constant gains," *Journal of Solar Energy Engineering*, vol. 123, no. 4, pp. 319–326, 2001.

[13] K. A. Stol and M. J. Balas, "Periodic disturbance accommodating control for blade load mitigation in wind turbines," *Journal of Solar Energy Engineering*, vol. 125, no. 4, pp. 379–385, 2003.

[14] K. E. Johnson, L. Y. Pao, M. J. Balas, and L. J. Fingersh, "Control of variable-speed wind turbines: Standard and adaptive techniques for maximizing energy capture," *IEEE Control Systems Magazine*, vol. 26, no. 3, pp. 70–81, 2006.

[15] G. E. Dullerud and F. Paganini, *A Course in Robust Control Theory: A Convex Approach*. New York, NY: Springer Science & Business Media, 2000, vol. 36.

[16] P. Gahinet and P. Apkarian, "A linear matrix inequality approach to $\mathcal{H}_\infty$ control," *International Journal of Robust and Nonlinear Control*, vol. 4, no. 4, pp. 421–448, 1994.

[17] C. Scherer, P. Gahinet, and M. Chilali, "Multiobjective output-feedback control via LMI optimization," *IEEE Transactions on Automatic Control*, vol. 42, no. 7, pp. 896–911, 1997.

[18] I. Masubuchi, A. Ohara, and N. Suda, "LMI-based controller synthesis: A unified formulation and solution," *International Journal of Robust and Nonlinear Control: IFAC-Affiliated Journal*, vol. 8, no. 8, pp. 669–686, 1998.

[19] D. Abou Jaoude and M. Farhood, "Distributed control of nonstationary LPV systems over arbitrary graphs," *Systems & Control Letters*, vol. 108, pp. 23–32, 2017.

[20] M. Farhood and G. Dullerud, "Control of nonstationary LPV systems," *Automatica*, vol. 44, no. 8, pp. 2108–2119, 2008.

[21] M. Farhood, "LPV control of nonstationary systems: A parameter-dependent Lyapunov approach," *IEEE Transactions on Automatic Control*, vol. 57, no. 1, pp. 209–215, 2012.

[22] D. Ossmann, J. Theis, and P. Seiler, "Robust control design for load reduction on a liberty wind turbine," ser. Dynamic Systems and Control Conference, American Society of Mechanical Engineers, vol. Volume 1: Advances in Control Design Methods, Nonlinear and Optimal Control, Robotics, and Wind Energy Systems, 2016.

[23] S. Wang and P. Seiler, "Gain scheduled active power control for wind turbines," in *32nd ASME Wind Energy Symposium*. 2014, pp. 1–14.

[24] D. Ossmann, J. Theis, and P. Seiler, "Load reduction on a clipper liberty wind turbine with linear parameter-varying individual blade pitch control," *Wind Energy*, vol. 20, no. 10, pp. 1771–1786, 2017.

[25] S. Wang and P. Seiler, "Gridded-based LPV control of a clipper liberty wind turbine," *Wind Energy*, vol. 21, no. 11, pp. 1106–1120, 2018.

[26] A. Megretski and A. Rantzer, "System analysis via integral quadratic constraints," *IEEE Transactions on Automatic Control*, vol. 42, no. 6, pp. 819–830, 1997.

[27] C.-Y. Kao, A. Megretski, U. Jonsson, and A. Rantzer, "A MATLAB toolbox for robustness analysis," in *Proceedings of the IEEE International Conference on Robotics and Automation*, 2004, pp. 297–302.

[28] U. Jönsson, "Lecture notes on integral quadratic constraints," 2001.

[29] U. Jönsson and A. Megretski, "IQC characterizations of signal classes," in *Proceedings of the European Control Conference*, 1999, pp. 1481–1486.

[30] A. Megretski, "Power distribution approach in robust control," *IFAC Proceedings Volumes*, vol. 26, no. 2, pp. 27–30, 1993.

[31] J. Veenman, C. W. Scherer, and H. Köroğlu, "Robust stability and performance analysis based on integral quadratic constraints," *European Journal of Control*, vol. 31, pp. 1–32, 2016.

[32] D. Abou Jaoude, D. Muniraj, and M. Farhood, "Robustness analysis of uncertain time-varying interconnected systems using integral quadratic constraints," in *Proceedings of the American Control Conference*, 2019, pp. 3087–3092.

[33] J. M. Fry, D. Abou Jaoude, and M. Farhood, "Robustness analysis of uncertain time-varying systems using integral quadratic constraints with time-varying multipliers," *International Journal of Robust and Nonlinear Control*, vol. 31, no. 3, pp. 733–758, 2021.

[34] D. Abou Jaoude and M. Farhood, "Guaranteed output bounds using performance integral quadratic constraints," in *Proceedings of the American Control Conference*, 2020, pp. 1557–1562.

[35] D. Abou Jaoude, P.-L. Garoche, and M. Farhood, "Computing state invariants using point-wise integral quadratic constraints and the S-procedure," in *Proceedings of the American Control Conference*, 2021, pp. 2394–2399.

[36] S. Wang, H. Pfifer, and P. Seiler, "Robust synthesis for linear parameter varying systems using integral quadratic constraints," *Automatica*, vol. 68, pp. 111–118, 2016.

[37] M. C. Palframan, J. M. Fry, and M. Farhood, "Robustness analysis of flight controllers for fixed-wing unmanned aircraft systems using integral quadratic constraints," *IEEE Transactions on Control Systems Technology*, vol. 27, no. 1, pp. 86–102, 2019.

[38] J. M. Fry and M. Farhood, "A comprehensive analytical tool for control validation of fixed-wing unmanned aircraft," *IEEE Transactions on Control Systems Technology*, vol. 28, no. 5, pp. 1785–1801, 2020.

[39] K. Zhou, J. C. Doyle, and K. Glover, *Robust and Optimal Control*. Upper Saddle River, NJ: Prentice Hall, 1996.

[40] K. Zhou, J. Doyle, K. Glover, and B. Bodenheimer, "Mixed $\mathcal{H}_2$ and $\mathcal{H}_\infty$ control," in *Proceedings of the American Control Conference*, 1990, pp. 2502–2507.

[41] A. Rantzer, "On the Kalman—Yakubovich—Popov lemma," *Systems & Control Letters*, vol. 28, no. 1, pp. 7–10, 1996.

[42] F. D. Bianchi, H. De Battista, and R. J. Mantz, *Wind Turbine Control Systems: Principles, Modelling and Gain Scheduling Design*. Springer, 2007, vol. 19.

[43] J. Jonkman, S. Butterfield, W. Musial, and G. Scott, "Definition of a $5-MW$ reference wind turbine for offshore system development," National Renewable Energy Lab (NREL), Golden, CO (United States), Tech. Rep., 2009.

[44] F. D. Adegas, C. Sloth, and J. Stoustrup, "Structured linear parameter varying control of wind turbines," in *Control of Linear Parameter Varying Systems with Applications*, Springer, 2012, pp. 303–337.

[45] G. S. Bir, "User's guide to MBC3: Multi-blade coordinate transformation code for 3-bladed wind turbine," 2010.

[46] G. Bir, A. Wright, C. Butterfield, G. Bir, A. Wright, and C. Butterfield, "Stability analysis of a variable-speed wind turbine," in *35th Aerospace Sciences Meeting and Exhibit*, 1997, p. 965.

[47] D. Zhang, L. Qian, B. Mao, C. Huang, B. Huang, and Y. Si, "A data-driven design for fault detection of wind turbines using random forests and XGBoost," *IEEE Access*, vol. 6, pp. 21 020–21 031, 2018.

[48] J. Lofberg, "YALMIP: A toolbox for modeling and optimization in MATLAB," *IEEE International Conference on Robotics and Automation*, pp. 284–289, 2004.

[49] M. ApS, *The MOSEK optimization toolbox for MATLAB manual. version 9.3.6*, 2021. [Online]. Available: https://docs.mosek.com/9.3/toolbox/index.html.

[50] M. Buhl Jr, "MCrunch user's guide for version 1.00," *National Renewable Energy Laboratory (NREL)*, 2008.

[51] D. Abou Jaoude, M. C. Palframan, and M. Farhood, "An oracle for the discrete-time integral quadratic constraint problem," *Automatica*, vol. 107, pp. 112–118, 2019.

[52] ——, "On the analytic center cutting plane method for the discrete-time integral quadratic constraint problem," in *Proceedings of the Conference on Decision and Control*, 2019, pp. 7988–7993.

[53] D. Abou Jaoude and M. Farhood, "Customized analytic center cutting plane methods for the discrete-time integral quadratic constraint problem," *IFAC-PapersOnLine*, vol. 55, no. 25, pp. 115–120, 2022.

[54] E. Khalife, D. Abou Jaoude, and M. Farhood, "Construction of worst-case input signals for discrete-time linear time-varying systems," in *Proceedings of the Conference on Decision and Control*, 2022, pp. 6855–6861.

[55] O. Farhat, D. Abou Jaoude, and M. Hudoba de Badyn, "$\mathcal{H}_\infty$ network optimization for edge consensus," *European Journal of Control*, vol. 62, pp. 2–13, 2021.